

## REVIEW ARTICLE

# Nano-optical imaging and spectroscopy of order, phases, and domains in complex solids

Joanna M. Atkin, Samuel Berweger, Andrew C. Jones and Markus B. Raschke\*

*Department of Physics, Department of Chemistry, and JILA, University of Colorado, Boulder, CO 80309, USA*

*(Received 13 February 2012; final version received 02 September 2012)*

The structure of our material world is characterized by a large hierarchy of length scales that determines material properties and functions. Increasing spatial resolution in optical imaging and spectroscopy has been a long standing desire, to provide access, in particular, to mesoscopic phenomena associated with phase separation, order, and intrinsic and extrinsic structural inhomogeneities. A general concept for the combination of optical spectroscopy with scanning probe microscopy emerged recently, extending the spatial resolution of optical imaging far beyond the diffraction limit. The optical antenna properties of a scanning probe tip and the local near-field coupling between its apex and a sample provide few-nanometer optical spatial resolution. With imaging mechanisms largely independent of wavelength, this concept is compatible with essentially any form of optical spectroscopy, including nonlinear and ultrafast techniques, over a wide frequency range from the terahertz to the extreme ultraviolet. The past 10 years have seen a rapid development of this nano-optical imaging technique, known as tip-enhanced or scattering-scanning near-field optical microscopy (*s*-SNOM). Its applicability has been demonstrated for the nano-scale investigation of a wide range of materials including biomolecular, polymer, plasmonic, semiconductor, and dielectric systems.

We provide a general review of the development, fundamental imaging mechanisms, and different implementations of *s*-SNOM, and discuss its potential for providing nanoscale spectroscopic including femtosecond spatio-temporal information. We discuss possible near-field spectroscopic implementations, with contrast based on the metallic infrared Drude response, nano-scale impedance, infrared and Raman vibrational spectroscopy, phonon Raman nanocrystallography, and nonlinear optics to identify nanoscale phase separation (PS), strain, and ferroic order. With regard to applications, we focus on correlated and low-dimensional materials as examples that benefit, in particular, from the unique applicability of *s*-SNOM under variable and cryogenic temperatures, nearly arbitrary atmospheric conditions, controlled sample strain, and large electric and magnetic fields and currents. For example, in transition metal oxides, topological insulators, and graphene, unusual electronic, optical, magnetic, or mechanical properties emerge, such as colossal magneto-resistance (CMR), metal–insulator transitions (MITs), high- $T_C$  superconductivity, multiferroicity, and plasmon and phonon polaritons, with associated rich phase diagrams that are typically very sensitive to the above conditions. The interaction of charge, spin, orbital, and lattice degrees of freedom in correlated electron materials leads to frustration and degenerate ground states, with spatial PS over many orders of length scale. We discuss how the optical near-field response in *s*-SNOM allows for the systematic real space probing of multiple order parameters simultaneously under a wide range of internal and external stimuli (strain, magnetic field, photo-doping, etc.) by coupling directly to electronic, spin, phonon, optical, and polariton resonances in materials. In conclusion, we provide a perspective on the future extension of *s*-SNOM for multi-modal imaging with simultaneous nanometer spatial and femtosecond temporal resolution.

**PACS:** 07.79.-Fv Near-field scanning optical microscopes, 68.37.Uv Near-field scanning microscopy and spectroscopy, 78. Optical properties, condensed-matter spectroscopy

---

\*Corresponding author. Email: markus.raschke@colorado.edu

**Keywords:** correlated electron systems; near-field; tip-enhanced Raman spectroscopy; nonlinear-spectroscopy; nanospectroscopy

<b>Contents</b>	<b>PAGE</b>
1 Introduction to optical nano-scale imaging	747
2 Phase behavior of strongly correlated and topological materials	749
2.1. Historic developments of correlated electron physics	750
2.2. Transition metal compounds	751
2.3. Graphene and topological materials	752
2.3.1. Graphene	752
2.3.2. Topological insulators	752
2.4. Competing degenerate phases and phase separation	753
2.5. Traditional microscopic techniques for the characterization of phase separation	754
3 Light–matter interaction and spectroscopy	757
3.1. Optical resonances and polarization	758
3.1.1. The macroscopic optical polarization	758
3.1.2. The resonant response	759
3.1.3. Drude description for the free carrier response	760
3.1.4. Vibrational polarization	760
3.2. Optical selection rules	761
3.2.1. Linear optics	761
3.2.2. Raman scattering	761
3.2.3. Nonlinear optics	763
3.2.4. Second-harmonic generation	763
3.2.5. Other nonlinear optical techniques	764
4 Optical microscopy: Far-field imaging	765
4.1. Optical microscopy techniques	766
4.1.1. Birefringence and dichroism microscopy	766
4.1.2. Raman microscopy	766
4.1.3. Second-harmonic generation microscopy	767
4.2. Far-field diffraction limit	770
5 Optical microscopy: near-field imaging	771
5.1. Fundamental principles of near-field microscopy	772
5.1.1. Scattering-scanning near-field optical microscopy	773
5.1.2. The coupled dipole model	775
5.1.3. Field enhancement and local field factor	776
5.1.4. Plasmonic field enhancement	777
5.2. Experimental considerations and implementations of <i>s</i> -SNOM	779
5.2.1. Scanning probe tips for <i>s</i> -SNOM	779
5.2.2. Tip-sample distance control	781
5.2.3. Focusing optics	781
5.2.4. Linear elastic light scattering in <i>s</i> -SNOM	782
5.2.5. Near-field spectral behavior	786
5.2.6. Microwave near-field impedance microscopy	786
5.2.7. Tip-enhanced Raman scattering	788
5.2.8. Nonlinear <i>s</i> -SNOM	792
5.2.9. Low-temperature and magnetic field <i>s</i> -SNOM	794
6 Applications of <i>s</i> -SNOM for the study of nano-scale phenomena in complex matter	795
6.1. Phase competition in metal–insulator transitions	795

6.1.1. Metal–insulator transition in vanadium oxide	796
6.1.2. Near-field microwave impedance microscopy of the MIT in CMR manganites	801
6.2. Low-dimensional electronic materials	802
6.2.1. IR <i>s</i> -SNOM imaging of graphene	802
6.2.2. Topological insulators	805
6.3. Domain imaging in ferroelectrics	805
6.3.1. Ferroelectric domains and domain walls	806
6.3.2. Raman Phonon Nanocrystallography	807
6.3.3. Other techniques for near-field imaging of ferroelectric domains	810
6.4. Magnetic domain imaging	812
6.4.1. Magnetic domains	812
6.4.2. Magneto-optic domain imaging	813
6.4.3. Magnetic SHG domain imaging	814
6.5. Multiferroics: Coupled ferroic order and domains	815
6.5.1. Hexagonal manganites	816
6.5.2. Domain coupling in hexagonal manganites	816
6.5.3. SHG <i>s</i> -SNOM imaging	817
7. Perspective for <i>s</i> -SNOM for nanoscale materials science	820
7.1. Ultrafast <i>s</i> -SNOM	820
7.2. Tip-sample coupling and spectroscopic <i>s</i> -SNOM signal interpretation	822
7.3. Increased sensitivity and contrast	823
7.4. Instrument development	825
7.4.1. Optical antenna engineered tips for <i>s</i> -SNOM	825
7.4.2. Integrated design and parallelization	826
7.4.3. Environmental conditions	826
7.5. Outlook	827
Notes	827
Acknowledgements	827
References	828

## 1. Introduction to optical nano-scale imaging

The power of optical spectroscopy is its ability to directly interact with the electronic, spin, and lattice excitations in matter. Owing to the vectorial nature of light both in terms of polarization and (momentum) wavevector, it can provide symmetry selectivity in both linear and nonlinear implementations. With ultrafast laser techniques, insight into the real-time dynamics of elementary interactions can be gained.

However, combining spectroscopy with optical microscopy techniques for simultaneous spatially resolved imaging has remained challenging with far-field diffraction limiting the spatial resolution to hundreds of nm in the visible and up to several micrometers in the infrared. This resolution is too coarse for many of the desired studies of mesoscopic phenomena in condensed matter physics, which are often determined by nanometer scale electronic, phonon, or spin scattering lengths. Optical microscopy has therefore not become a primary research tool in solid-state physics to the same extent as in biology, medicine, or petrology applications.

The development of optical imaging techniques with spatial resolution beyond the diffraction limit was a slow one. Near-field scanning optical microscopy (NSOM) only emerged in the late 1980s [1–3], providing sub-diffraction-limited spatial resolution through the use of tapered fibers or hollow waveguide tips. However, waveguide cut-off and aperture-limited fiber throughput typically constrain sensitivity and practical resolution to  $\sim 100$  nm, with a narrow wavelength range due to

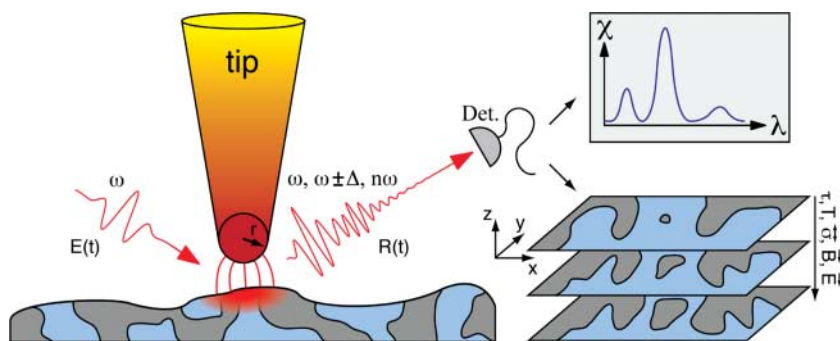


Figure 1. The conceptual representation of tip-enhanced or tip-scattering *s*-SNOM for optical spectroscopic imaging with sub-diffraction limited spatial resolution. With excitation provided by a continuous or pulsed field  $E(t)$  (frequency  $\omega$ ), the locally enhanced optical tip-sample coupling produces a response function  $R(t)$  with nanometer spatial resolution in combination with essentially any linear ( $\omega$ ), nonlinear ( $n\omega$ ), and ultrafast ( $\tau$ ) optical technique. Compatible with variable and low-temperature  $T$ , magnetic field  $B$ , electric field  $E$ , sample strain  $\overleftrightarrow{\sigma}$ , etc., *s*-SNOM enables mapping of the nanoscale structural inhomogeneities of materials and their evolution under these stimuli.

fiber compatibility. This limits the suitability of NSOM as a solid-state imaging technique, which would call for even higher spatial resolution while probing at a wide wavelength range and at low signal levels. The more recent development of far-field localization techniques [4–6] can achieve resolution of discrete molecular or quantum dot emitters by point-spread function reconstruction with precision as high as 20 nm, but these rely largely on fluorescence and/or dilute samples.

This situation changed with the development of tip-enhanced, apertureless, or tip-scattering (*s*-SNOM<sup>1</sup>). This is based on a compellingly simple idea that emerged from the desire to combine the high spatial resolving power of tip-based scanning probe microscopies such as atomic force microscopy (AFM) and scanning tunneling microscopy (STM) with the spectroscopic abilities of optical techniques. As shown conceptually in Figure 1, illumination of the apex of a sharp (metallic or semiconducting) scanning probe tip of an AFM or STM, typically by a focused laser beam, leads to some degree of spatial localization of the light-matter interaction with the sample in the near-field region of the tip apex, defined by the apex radius. After suitable discrimination of the tip-apex scattered light from far-field background, few nanometer spatial resolution can be obtained, determined to first order by the nanoscopic apex radius.

Following the conception of near-field microscopy [1–3, 7–12], and subsequent implementation of different spectroscopies [13–19], the basic physics underlying the imaging process seem to be understood. Most initial *s*-SNOM applications, with implementations in particular of dielectric and vibrational infrared and Raman spectroscopy, have focused on molecular, plasmonic, or dielectric systems, and a number of excellent reviews have summarized the rapid and successful progress in the field [20–29].

In this review, we will provide a summary and perspective based on new fundamental insights and technical developments in recent years that have shown the way for a generalization of the concepts of *s*-SNOM. We discuss the fundamental imaging mechanisms and different spectroscopic implementations, including advanced linear, nonlinear, and ultrafast techniques. Although several technical challenges still persist, we provide a perspective showing the level of microscopic insight that can be gained by taking advantage of the optical symmetry selectivity, resonant specificity, and nano-scale sensitivity provided by *s*-SNOM in different optical imaging modalities.

Concurrently with the emergence of *s*-SNOM as a viable tool for optical nano-imaging, a range of powerful new electron and X-ray microscopies and spectroscopies have been developed for the

study of both static as well as dynamic nanoscale material phenomena. Their detailed discussion is beyond the scope of our review and we will only cover them briefly where they complement or are complemented by *s*-SNOM.

In spite of the sensitivity of *s*-SNOM to a wide range of electronic or lattice structural phenomena depending on the choice of optical process, relatively little work has focused on the investigation of correlated materials. These materials, in part as a result of the strong electron correlations, exhibit a prevailing tendency to form structural inhomogeneities, phases, domains, and order over a wide range of length scales ranging from atomic to macroscopic dimensions. We discuss how the application of *s*-SNOM in combination with different optical techniques could provide the much needed nanoscale characterization of correlated matter and other complex solid matter. Despite this topical focus on these classes of materials, much of the review is kept general for the reader of other disciplines, and the applications discussed can readily be extended to other classes of materials.

The strong electron correlation in, e.g., transition metal oxides and related materials leads to unusually rich phase diagrams with distinct crystallographic, electronic, and magnetic phases, and frustration and degenerate ground states. One resulting phenomenon is that in many cases phase competition and a coexistence of multiple phases occurs near phase boundaries. It has become increasingly evident that this behavior gives rise to structural and electronic inhomogeneities and nanoscale spatial phase separation with complex spatial architecture [30,31]. This phase coexistence, over a wide range of length scales from the nano- to microscale, is determined by both intrinsic and extrinsic factors. It can be static or dynamic, and is very sensitive to external stimuli, as shown conceptually in Figure 2. A generally applicable technique that can provide the necessary microscopic insight could hold the key to the mechanisms underlying these complex material systems. With its compatibility with essentially any sample temperature, strong magnetic and electric fields, sample strain, and environmental pressure, *s*-SNOM can complement and may exceed many alternative imaging and spectroscopy techniques.

Section 2 of this paper gives a brief introduction to correlated and topological materials and their spatial inhomogeneities. In Section 3, we provide background for the relevant light–matter interactions and the material properties they can probe. Section 4 contains examples of the use of several spectroscopic techniques for far-field microscopy. Section 5 contains a theoretical discussion of the spatial localization and imaging mechanisms in *s*-SNOM, and experimental considerations for implementing the various spectroscopic techniques. The results of several near-field optical experiments are summarized in Section 6. In this review, we emphasize in particular results on correlated or topological materials and graphene, as well as a discussion of domain structure within ferroelectric (FE) and ferromagnetic (FM) materials, as an illustration of the various approaches to probing complex material properties. Finally, in Section 7 we discuss some remaining challenges and future improvements for *s*-SNOM to increase its sensitivity and specificity, and we provide a perspective on extending to the time domain for ultrafast nano-imaging.

## 2. Phase behavior of strongly correlated and topological materials

The term “correlated electron systems” is often used to designate materials for which the non-interacting band-structure model fails to correctly predict their electronic properties [32–34]. Strong electron–electron Coulomb and spin interactions, associated unusual electron–lattice coupling and distortions, and a range of new quasi-particle excitations give rise to unique material properties including superconductivity, colossal magneto-resistance (CMR), metal–insulator transitions (MIT), and multiferroicity. Another range of exotic electronic phases and collective behavior can arise from constraining the physical dimensions of a system, as in graphene and topological materials in two dimensions. While the wide range of new and often coupled magnetic,

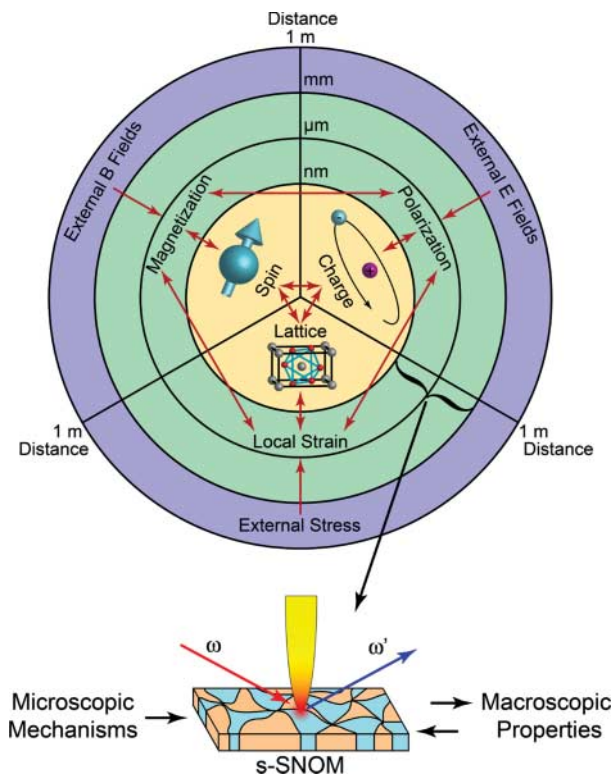


Figure 2. The role of coupled charge, spin, and lattice degrees of freedom in the formation of inhomogeneous mesoscopic domains ranging from the atomic scale, to macroscopic dimensions. The interplay of these interactions (red arrows) can result in intrinsic phase coexistence on mesoscopic length scales (1 nm to 1 mm). *s*-SNOM via the local near-field tip-sample interaction provides spectroscopic access with few nanometer spatial resolution. It can probe nanoscale domain order, which is a reflection of the underlying microscopic mechanisms of many emergent material properties. Similarly, nano-scale phase separation controls the macroscopic materials properties and can in turn be influenced by external stimuli.

electronic, optical, or mechanical properties holds significant promise for technological device applications (e.g., for sensing, control, solar, storage, catalysis, etc.), the complex underlying physics is poorly understood. The nanoscale optical investigation of the domain and phase behavior in correlated and topological matter can thus contribute to the microscopic understanding of the origin of their properties.

In the following sections, we briefly summarize the basic properties of correlated electron and topological materials, their phase behavior, phase competition and domain formation, and the range and limitations of conventional techniques employed for their investigations.

### 2.1. Historic developments of correlated electron physics

The development of quantum mechanics in the early 1900s identified both the particle-like and wave-like properties of matter, with electrons defined by radial  $n$ , orbital-angular momentum  $l$ , magnetic orbital  $m_l$ , and spin  $m_s$  quantum numbers. The significance of these concepts for the description of the electronic behavior of solids was realized soon after the development of the band theory description of metals and insulators in the first half of the twentieth century [35–39].

Band theory describes the electronic states in a crystal in terms of Bloch waves. These states are the energy eigenfunctions for a periodic (crystalline) lattice, which may be written as the product of a plane wave envelope function and a periodic function. The energy–momentum dispersion relation corresponding to the solutions for these states takes the form of bands relating allowable momentum for electronic states to a given energy. One of the primary assumptions of this band structure description is that the valence electrons are described as non-interacting within a static and periodic atomic lattice.

Within the band model, insulators and semiconductors exhibit a band gap separating a highest occupied valence from a lowest unoccupied conduction band with a mid-gap Fermi level. With a full valence band, electronic conduction is prohibited as there are no low-energy unoccupied electron energy states available under small-energy perturbations of the valence electrons. In contrast, conductors have partially filled energy bands, and the highest energy electrons at the Fermi level can easily be perturbed to unoccupied states.

Even during the development of the band model, it was recognized that the assumption of negligible electron–electron Coulomb interaction and other interactions may fail to predict the electronic structure of certain materials [40]. The first example was NiO, for which conventional band theory predicts metallic behavior, but which is found to be a transparent insulator [41,42]. It was proposed that the insulating character of this material system was due to electron–electron interactions, and it was later shown that the insulating properties arise from the presence of an anti-ferromagnetic (a-FM) sub-lattice [43–46]. Subsequently, a wide range of other materials have been identified for which a simple band structure description fails to correctly predict their electronic properties and other physical phenomena. NiO set the stage for the broad definition of complex and correlated electron systems as those systems whose electronic structure deviates from the band-theory model via the presence of strong electron–electron, –phonon, –spin, or –quasi-particle interactions.

## 2.2. Transition metal compounds

One class of materials in which correlated electron effects and associated phase behavior is particularly prevalent are transition metal compounds. In these materials, the mutual interaction of the electronic degrees of freedom is a fundamental component in the wide variety of exotic and complex physical phenomena observed.

The transition metals are elements whose stable ions have partially filled *d* shells (the “*d*-block” of the periodic table) that are characterized by multiple possible orbital and spin states. Many transition metals exhibit multiple oxidation states, in particular vanadium, chromium, and manganese. Similar ion sizes allow for a wide range of doping and substitutions with each other and also with lanthanide and actinide ions. That, together with small differences in oxidation/reduction potential, gives rise to a wide variety of transition metal compounds, in particular oxides, with different crystal structure and electronic behavior as a result of the multitude of possible *d*-band electronic interactions.

In certain cases, the interaction of the intrinsic orbital and spin states of the valence electrons in transition metal oxides with external parameters such as electric, magnetic, and strain fields can lead to the development of a rich phase behavior. Examples that exhibit such correlated electron effects include cuprates, manganites, ruthenates, Fe-pnictides, and heavy-fermion alloys. These substances are often characterized by competing nearly degenerate states with coupled charge, orbital, spin, and lattice degrees of freedom.

Much of the most interesting, complex, and poorly understood condensed phase physics today is associated with these materials, including CMR [47–49], MIT [50], multiferroicity [51], and high-temperature superconductivity [52,53]. In spite of the large potential of these phenomena for

future technological applications, the current understanding of these systems is incomplete due to the complex fundamental physics involved in the formation of the electronic properties of these materials. Currently, a lack of systematic knowledge of the relevant driving forces and parameters behind many of these exotic phases make material design and device applications difficult.

### 2.3. Graphene and topological materials

The confinement of electrons to two dimensions can result in fundamental changes in the electronic dispersion relation as well as differences in electron–electron and electron–spin interactions in a material. These changes give rise to novel electronic behaviors, some of which hold great potential for the development of future nano-electronics, opto-electronics, and photonic devices.

#### 2.3.1. Graphene

The two-dimensional (2D) carbon allotrope of  $sp^2$  hybridized and bonded C-atoms in a honeycomb lattice constituting a single graphene sheet provides an ideal basis for the study of a prototypical 2D electron system. Its band structure is characterized at low energies by a linear energy–momentum relationship. The linear dispersion relationship yields effective electron and hole masses of zero, corresponding to relativistic particles described by the Dirac equation and leading to the terminology of Dirac fermions for the electrons and holes [54,55]. With one electron per carbon atom in the  $\pi$ -levels, the  $\pi$  and  $\pi^*$  bands are degenerate at the  $K$  points of the hexagonal Brillouin zone for symmetry reasons, with the Fermi level between the two symmetrical bands. This makes graphene technically a zero-gap semiconductor.

The linear dispersion relation results in a pronounced ambipolar electric field effect, with charge carriers tuned continuously between electrons and holes. Furthermore, the high mobility of charge carriers in graphene has garnered significant interest for its application in future electronic devices.

Interestingly, despite its role as a prototypical featureless 2D electronic system, STM studies of graphene have revealed spatial inhomogeneities in the electronic structure [56]. These variations result from microscopic perturbations such as topographic corrugations and impurities in an otherwise homogeneous graphene sheet. Ultimately, the scattering associated with these electronic inhomogeneities imposes a limit on the mobility of electrons in graphene systems [56].

Graphene also exhibits several interesting optical properties [57]. In particular, surface waves in the form of density waves of Dirac fermions have been predicted with high oscillator strength at mid-infrared frequencies [58,59]. While the understanding of the generation and properties of surface plasmon polaritons (SPPs) in noble metals is well developed, metallic SPPs are hampered by large ohmic losses due to poor conductivity at optical frequencies. In contrast, graphene represents a promising alternative system with the possibility of new forms of plasmonic engineering with large propagation length, tuning by physical geometry, external field gating, and doping.

#### 2.3.2. Topological insulators

Topological surface states with exotic 2D correlated electron effects have recently been discovered at the surfaces and interfaces of certain insulators. While many similarities exist between the electronic structure of graphene and topological insulators [60], spin–momentum coupling with spin orientation at right angles with respect to the electron momentum distinguishes topological surface states from ordinary surface states of bulk materials or the electronic structure of graphene. These new states are unique in that they are topologically protected against scattering from surface impurities and perturbations by time-reversal symmetry. Both topological insulator surface states and graphene have a linear energy–momentum dispersion relationship. Yet while graphene has two Dirac points and is spin degenerate, topological insulators have only one Dirac point and no

spin degeneracy [60]. Also, while the carbon composition of graphene results in the Fermi level naturally occurring at the Dirac point, this is not necessarily the case for topological insulators [60]. Much of the interest in topological insulators stems from a new quantum spin Hall effect, which was predicted and discovered in 2D structures such as HgTe quantum wells [61,62] as well as three-dimensional (3D) crystals of  $\text{Bi}_{1-x}\text{Sb}_x$ ,  $\text{Bi}_2\text{Se}_3$ , and  $\text{Bi}_2\text{Te}_3$  [63–65] at low temperatures. The topological protection of the surface states in principle allows for dissipationless transport which should be associated with interesting plasmonic properties. The development of understanding of the novel properties of the surface states in topological insulators may hold promise for the development of solid-state quantum computing, magneto-electric, and spintronic devices.

#### 2.4. Competing degenerate phases and phase separation

The strong electron correlations in transition metal oxides and related materials often result in complex phase diagrams with distinct crystallographic, electronic, and magnetic phases. In addition, electronic phases can often be degenerate and can exhibit a high degree of geometrical frustration imposed by the crystal lattice symmetry. Frustration occurs when competing terms of electronic or spin ordering are incommensurate (for example, in a triangular spin lattice). Frustrated and nearly degenerate phases can lead to phase competition and coexistence over a wide range of parameters, such as temperature, doping, or strain, possibly even in an ideal nominally homogeneous pure single crystal [31]. The trade-off between the free energies of the competing phases, the domain wall energies, and the elastic strain energies can give rise to stable nanoscale spatial PS, sometimes with a complex spatial architecture [30,31,66–69]. It has become increasingly evident that phase co-existence is controlled by both intrinsic and extrinsic factors and results in domain formation over a wide range of length scales from the atomic scale to macroscopic mm dimensions depending on material system and conditions.

The PS in correlated electron systems may involve several mechanisms that are poorly understood. While the intrinsic phase transition could be of first order, “incomplete transitions” may occur [31,70,71] where the inhomogeneous mixture of phases exists as a metastable state. The phase co-existence and separation may involve the mutual coupling of several degrees of freedom, making their description generally complex. One proposed reasoning for the presence of PS is the role of disorder or structural interactions which energetically favor a phase-separated state [67,72]. Long-range elastic strain, both extrinsic and intrinsic, may also be a driving component of PS [67].

Initial model descriptions of phase-separation have led to the phenomenological picture of electronic and structural PS, where, for example in CMR compounds, FM metallic, charge-ordered (CO)/orbital ordered (OO)/a-FM insulating, and paramagnetic (PM) insulating states may compete. Instead of a critical temperature  $T_C$  which would describe the transition of the unconstrained system, the intermediate regime characterized by the phase coexistence can be defined by a new temperature  $T^*$ , the temperature at which the onset of local mixed phase behavior and/or local order occurs, as shown in Figure 3.

While qualitatively new and interesting physical properties in the regime of phase competition emerge, it complicates the investigation and microscopic understanding of the origin of the phase behavior [30]. The details and microscopic origins of that spatial separation of electronic, magnetic, and lattice structural inhomogeneities in correlated electron materials is therefore the subject of much current research interest and debate. Even the role of domains in defining macroscopic material properties is often unclear. The description of the physics of PS is complicated by many competing interactions at similar energy scales. As a result, the theoretical description of the microscopic mechanisms and length-scales which arise in these systems remains incomplete. While it has emerged that spatial phase separation and co-existence can often exist and spans length scales of more than five orders of magnitude ranging from the atomic to the hundreds

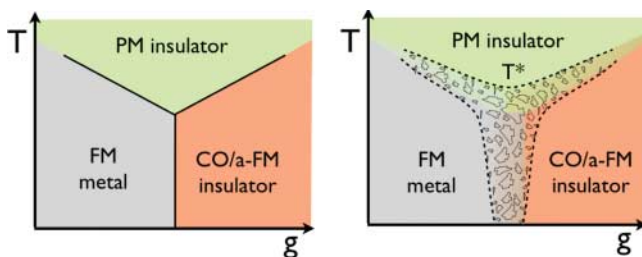


Figure 3. Schematic phase diagram indicating the ideal macroscopic first-order phase boundaries (left) and multi-phase coexistence and spatial separation scenario (right) with domain formation. The parameter  $g$  represents a generalized control parameter such as doping, strain, or external fields. In this example, competition between a paramagnetic (PM) insulation, FM metallic, and charge ordered (CO) a-FM phases leads to a gradual phase transition with phase coexistence over a wide parameter range and with a possibly wide variety of domain sizes and texture.

of micrometer scale, for example, in CMR materials, little is known quantitatively about domain texture (stripes, patches, etc.) and phase fraction as a function of varying temperature or strain. One of the foremost challenges in characterizing correlated electron systems which exhibit degenerate phases and phase separation is the fact that much experimental evidence of the intrinsic phase properties is indirect. Few studies and techniques have yet been able to systematically monitor with sufficient spatial resolution the PS and domain evolution across a phase transition.

### 2.5. Traditional microscopic techniques for the characterization of phase separation

The presence of both intrinsic and extrinsic nanoscale spatial inhomogeneities in the electronic, spin, or lattice structural response of strongly correlated materials, in particular, in CMR, metal-insulator transition (MIT), and high- $T_C$  superconductor systems, was initially inferred indirectly from bulk measurements such as transport [73,74], X-ray, and neutron diffraction [75,76], and angle-resolved photo-emission spectroscopy (ARPES) [77]. The macroscopic and spatially averaged quantities measured by these techniques often exhibit a broadened phase transition as a function of temperature. This broadening can be interpreted as the result of phase coexistence and the formation of an inhomogeneous phase distribution at microscopic length scales. Much experimental effort has thus been dedicated to the development and implementation of microscopic techniques to identify the underlying spatial architecture of the sample and to determine the intrinsic properties of the competing phases near the phase transition. This understanding would allow for an explanation of the observed macroscopic materials response and would be essential for the development of a theoretical description of the microscopic driving forces behind the phase behavior.

To this end, several experimental microscopy methods have been developed, foremost among them are the electron-based scattering, transmission, and tunneling probes, with each technique having its advantages and disadvantages in garnering specific information on the microscopic properties of the material. A summary of the spatial resolution and energy sensitivity of some of these techniques is shown in Figure 4 [78]. Transmission electron microscopy (TEM) and scanning electron microscopy (SEM) achieve high spatial resolution with  $\sim 1$  nm for SEM and  $\sim 0.01$  nm for TEM based on the short de Broglie wavelength of electron beams at 5–30 keV (SEM) and 50–400 keV (TEM) [79,80]. These techniques have successfully been used to characterize electronic phase separation in several correlated electron materials [81–86]. Dark-field TEM evidence of metallic and insulating phases in the manganite  $\text{La}_{5/8-y}\text{Pr}_y\text{Ca}_{3/8}\text{MnO}_3$  is shown in Figure 5(i). Although operating at keV electron energies that far exceed the energy scales of

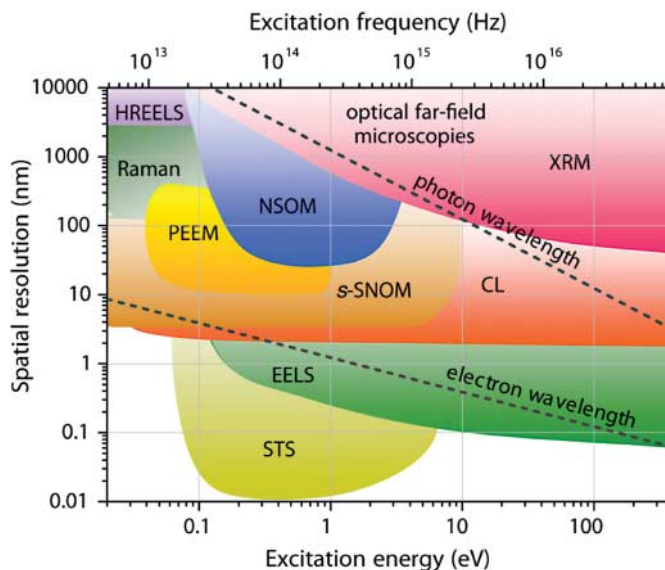


Figure 4. Ranges of spatial and spectral information achievable by different spatially resolved optical and electron-based spectroscopy techniques, including high-resolution electron-energy loss spectroscopy (HR-EELS), X-ray microscopy (XRM), photoemission electron microscopy (PEEM), NSOM, *s*-SNOM, cathodoluminescence (CL), and scanning-tunneling spectroscopy (STS). After F.J. García de Abajo, *Rev. Mod. Phys.* 82 (2010), pp. 209–275 [78]. Copyright 2010 by the American Physical Society.

the elementary excitations and processes in the materials, spectroscopic sensitivity is nevertheless achieved via energy or momentum resolved detection of the inelastic electron interaction with the medium. Electronic microscopy techniques with spectral sensitivity include electron energy loss spectroscopy (EELS), high-resolution electron energy loss spectroscopy (HR-EELS), photoelectron emission microscopy (PEEM), and cathodoluminescence microscopy (CL). PEEM with soft X-ray synchrotron radiation, in particular, is emerging as a useful technique for the study of multiferroics, as it can detect FM and *a*-FM order through X-ray dichroism and resolve their domain structures [87]. Improvements in aberration correction mean that tens of nanometer resolution is now possible. The advantage of the high spatial resolution of these techniques, however, is associated with the need to operate at high or even ultrahigh vacuum (HV/UHV) and the need for special sample or surface preparation. For TEM, the penetration depth of electrons into the material limits sample thicknesses to  $t \lesssim 100$  nm. For SEM measurements the sample is required to be conductive to prevent charge accumulation. Owing to their high surface sensitivity PEEM and ARPES require ideally atomically clean surfaces in order to avoid signal convolution with adsorbate signatures.

With far-field optical spectroscopy techniques limited by the wavelength of light, one strategy for achieving high spatial resolution is to increase the photon energy in order to reduce the wavelength thus maximizing resolution. Scanning X-ray microscopy (XRM) achieves high contrast, element-specific microscopy and spectroscopy, with spatial resolutions down to 25–50 nm [88]. Synchrotron radiation sources are typically used, though table-top ultrafast soft X-ray sources are now available [89,90].

The scanning tunneling microscope (STM) [91,92] provides atomic resolution (down to 0.01 nm) exceeding most techniques except for TEM. The implementation of scanning tunneling spectroscopy (STS) provides a means for gaining spectroscopic information in the 0–5 eV

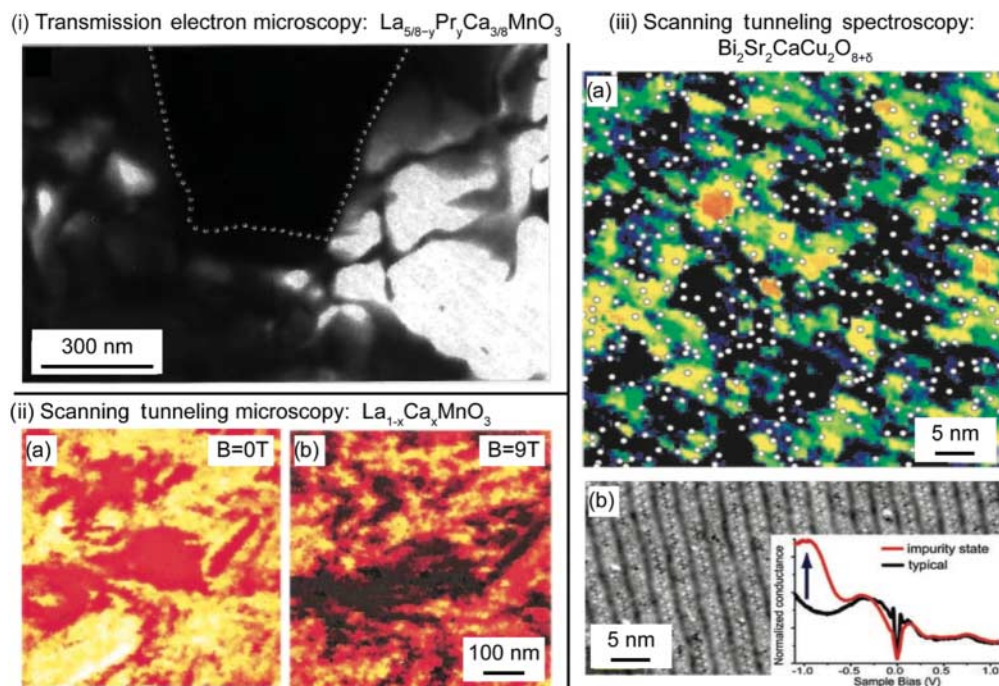


Figure 5. Examples of the nanoscale imaging of phase separation in correlated electron systems with electron and scanning probe microscopy techniques. (i) Dark-field TEM showing coexistence of insulating and metallic domains in  $\text{La}_{5/8-y}\text{Pr}_y\text{Ca}_{3/8}\text{MnO}_3$  (adapted by permission from Macmillan Publishers Ltd: Uehara *et al.*, Nature 399 (1999), pp. 560–563 [81], copyright 1999). (ii) Spectroscopic images of the tunneling conductance in  $\text{La}_{1-x}\text{Ca}_x\text{MnO}_3$ , measured using an STM (from Fäth *et al.*, Science 285 (1999), pp. 1540–1542 [98]. Reprinted with permission from AAAS). Panels (ii)-a and (ii)-b show mappings of local metal–insulator inhomogeneities for external magnetic fields of 0 and 9 T, respectively. Light areas in these panels represent insulating material while dark regions are indicative of metallic regions. (iii) STS images for locating impurity defects and correlating their presence with electronic inhomogeneities in high- $T_C$   $\text{Bi}_2\text{Sr}_2\text{CaCu}_2\text{O}_{8+\delta}$ . Panel (iii)-(a) represents an STS mapping of the superconducting energy gap with the superimposed positions of impurity sites in the substrate. Black regions indicate a wide energy gap ( $\geq 70$  meV) while the red regions indicate a small energy gap ( $\leq 20$  meV). Panel (iii)-(b) displays an atomically resolved topography image of the BiO surface of  $\text{Bi}_2\text{Sr}_2\text{CaCu}_2\text{O}_{8+\delta}$ . The inset displays the STS differential conductance signature of impurity states (from McElroy *et al.*, Science 309 (2005), pp. 1048–1052 [96]. Reprinted with permission from AAAS).

spectral range [93]. Different STS techniques have been implemented with great success in characterizing the electronic inhomogeneities in high- $T_C$  superconductor materials [94–97]. Examples of the use of STM and STS to investigate phase inhomogeneity in correlated materials are shown in Figure 5, for manganite  $\text{La}_{1-x}\text{Ca}_x\text{MnO}_3$  [98], and high- $T_C$  superconductor  $\text{Bi}_2\text{Sr}_2\text{CaCu}_2\text{O}_{8+\delta}$  [96]. Despite their high resolution and sensitivity to low-energy electronic states, the scanning tunneling feedback relies on the tunneling current between tip and sample, necessitating a conductive sample surface. Moreover, the tunneling current is dominated by near-surface electronic states. As a result, these measurements are only sensitive to bulk electronic states where the states are not perturbed by the broken translational invariance in the surface normal direction or convoluted by additional surface states.

Following the development of STM, AFM emerged as a powerful means to characterize non-conductive samples with high spatial resolution [99,100]. One of the primary advantages of AFM

is that it can readily be combined with external electric or magnetic fields and serve as a general platform for electric and magnetic force measurements with high spatial resolution. These derived techniques include electrostatic force microscopy (EFM), magnetic force microscopy (MFM), or piezoresponse force microscopy (PFM). These techniques allow for the characterization of conductive, FE [101,102], and magnetic [103–105] sample properties with nanometer spatial resolution, although not simultaneously. As they rely on static fields they have low time resolution, may perturb domain boundaries, and are insensitive to a-FM order (which is prevailing in many correlated materials, including CMR and multiferroics).

Despite the wide breadth of microscopic characterization techniques, there is a lack of a technique which can image multiple order parameters simultaneously, operate under strong magnetic and electric fields over a wide range of temperatures, access many different orders of length scales, and probe ultrafast time scales. These capabilities are the primary advantages of optical microscopy techniques, in which light of controllable temporal duration and energy directly interacts with the electronic structure of a material. In the following sections, we will discuss the resolution limitations on conventional far-field microscopy and how such limitations may be overcome through near-field measurement techniques.

### 3. Light–matter interaction and spectroscopy

Many of the microscopy techniques discussed in the previous section have been applied with great success for the real-space investigation of a wide range of atomic to mesoscopic phenomena associated with phase behavior in strongly correlated electron materials. However, they only provide limited access to the intrinsic energy scales of the elementary excitations and their coupling. The relevant energy scales of the charge, spin, and lattice excitations and collective modes are in the meV to eV energy range, corresponding to the IR to UV spectral ranges of electromagnetic radiation. Optical spectroscopy can therefore yield direct information on electronic and lattice structure, their excitations, and intrinsic dynamics [106–108]. From measurements of the optical response one can, in principle, gain highly specific insight into the underlying mechanisms of a wide range of material properties. The spectral characteristics of the optical response reflect electronic and vibrational excitations, their coupling, quasi-particle excitations, and other collective processes (polaritons, polarons). The wavevector and polarization sensitivity reflects crystal, spin, and electronic structure symmetry. With the extension to nonlinear spectroscopy [109–113], insight into the coupling of many of the above listed material excitations and parameters is possible in a unique way. With optical cycles as short as femto- and even attoseconds [114], dynamic information about the elementary electronic and nuclear motion of the elementary processes in the material can be obtained [115–117]. Optical phase information provides a means to control and enhance the specificity of many of these optical techniques.

A wide range of coherent and incoherent light sources now cover a broad photon energy range, from the THz [118,119] into the extreme ultraviolet (XUV) and X-ray regime [120,121]. Short and intense light pulses, including pulse shaping techniques for the generation of nearly arbitrary optical waveforms, are also available [122]. These are augmented by a variety of highly sensitive optical detection techniques. A suitable combination of frequency, pulse duration, and pulse energy allows for the excitation of non-equilibrium states of correlated matter not accessible by any other means. Lastly, optical spectroscopy is applicable under a wide range of internal and external stimuli including arbitrary temperature, atmospheric conditions, sample strain, and the application of strong electric and magnetic fields.

In the following section, we will first discuss the basic principles of the light–matter interaction, specific optical processes and their selection rules, and the spectroscopic signatures of different material properties.

### 3.1. Optical resonances and polarization

For most practical purposes the semi-classical description of light–matter interaction provides a sufficiently good approximation for the optical spectroscopy of condensed matter. In this model, light is treated as a wave by classical electromagnetic theory. The propagation of light through a medium and the macroscopic material response to applied optical fields are described by Maxwell's equations [123]. A quantum description is used for the medium itself, with interaction events corresponding to the quantized absorption and emission of a photon. Within this model, the optical characterization of the medium proceeds from the determination of macroscopic optical properties such as the dielectric permittivity and optical conductivity of the system to the interpretation in terms of its microscopic quantum mechanical electronic, lattice, or spin structure.

In order to understand the optical response of a material, it is first necessary to formulate a model for the response of the macroscopic system to an applied optical field.

#### 3.1.1. The macroscopic optical polarization

The response of a material to an incident electric field  $\mathbf{E}$  can be described in terms of the polarization (the induced dipole moment per unit volume)  $\mathbf{P}$ , as

$$\mathbf{P} = \epsilon_0 \overleftrightarrow{\chi} \mathbf{E}. \quad (1)$$

$\overleftrightarrow{\chi}$  is the linear electric susceptibility, an intrinsic or extrinsic property describing the response of the material to light. Relating  $\overleftrightarrow{\chi}$  to microscopic processes such as electron or lattice dynamics requires their quantum mechanical description.

For optical fields comparable to the intra- or interatomic field strength, the linear relationship between external field and polarization begins to fail, leading to nonlinear contributions to the induced optical polarization, which can be described by performing a power-series expansion of  $\mathbf{P}$  with respect to the electric field [109,110]:

$$\begin{aligned} \mathbf{P} &= \mathbf{P}_1 + \mathbf{P}_{\text{nl}} \\ &= \underbrace{\epsilon_0 \overleftrightarrow{\chi}^{(1)} \mathbf{E}}_{\text{linear}} + \underbrace{\epsilon_0 \overleftrightarrow{\chi}^{(2)} \mathbf{E}^2 + \epsilon_0 \overleftrightarrow{\chi}^{(3)} \mathbf{E}^3 \dots}_{\text{nonlinear}} \end{aligned} \quad (2)$$

Here,  $\overleftrightarrow{\chi}^{(n)}$  represent the  $n$ th order nonlinear response expressed in terms of tensors of rank  $n + 1$ .

For the linear optical response of a solid-state medium, the displacement field (in the frequency domain) is written as

$$\begin{aligned} \mathbf{D}[\omega] &= \epsilon_0 \mathbf{E}[\omega] + \mathbf{P}[\omega] \\ &= \epsilon_0 \overleftrightarrow{\epsilon}[\omega] \mathbf{E}[\omega] \end{aligned} \quad (3)$$

with  $\overleftrightarrow{\epsilon}[\omega]$  the optical permittivity (or dielectric function) of the material. In combination with Equation (1), this leads to the relationship

$$\overleftrightarrow{\epsilon}[\omega] = 1 + \overleftrightarrow{\chi}[\omega], \quad (4)$$

where  $\overleftrightarrow{\chi}$  and  $\overleftrightarrow{\epsilon}$  are complex and dimensionless quantities. For the following, when discussing anisotropic media the tensor notation of the permittivity will be maintained; for isotropic media, the permittivity will simply be denoted as a scalar  $\epsilon$ .

Often the optical properties of a medium are expressed in terms of the complex index of refraction,  $\mathcal{N} = n + i\kappa$ , which is related to the dielectric permittivity  $\epsilon$  and the magnetic

permeability  $\mu$  as

$$\mathcal{N} = \sqrt{\epsilon\mu}. \tag{5}$$

$\mu = 1$  for non-magnetic materials, and even for magnetic materials is typically very close to 1 at optical frequencies, so that the relation  $\mathcal{N} \simeq \sqrt{\epsilon}$  holds. Then the real and imaginary parts of the dielectric permittivity are associated with the index of refraction  $n$  and absorption index  $\kappa$  of a medium by

$$\begin{aligned} \text{Re}[\epsilon] &= n^2 - \kappa^2, \\ \text{Im}[\epsilon] &= 2n\kappa. \end{aligned} \tag{6}$$

An alternative approach is to express the material response in terms of an induced current,

$$\mathbf{j}[\omega] = \overleftrightarrow{\sigma}[\omega]\mathbf{E}[\omega], \tag{7}$$

where  $\overleftrightarrow{\sigma}[\omega]$  is the optical conductivity, a linear response function analogous to  $\overleftrightarrow{\chi}[\omega]$  in Equation (1). It is related to the permittivity by

$$\sigma[\omega] = -i\omega\epsilon_0(\epsilon[\omega] - 1). \tag{8}$$

Measurement of the real and imaginary parts of  $\epsilon[\omega]$ ,  $\sigma[\omega]$ , or  $\mathcal{N}[\omega]$  for a given material provides information about resonant behavior that derives from the microscopic interactions of the charge carriers and lattice with light.

### 3.1.2. The resonant response

For non-conducting media the optical permittivity associated with the induced motion of polarizable bound charges and nuclei can be described using a driven and damped harmonic oscillator with the harmonic potential defined by a force constant  $K_e$ . In a time varying electric field, the charge motion and resulting optical permittivity of the material is given by a Lorentzian as [107]

$$\epsilon[\omega] = \epsilon_\infty + \frac{n_e e^2}{m_e \epsilon_0} \frac{1}{(\omega_0^2 - \omega^2 - i\gamma\omega)}. \tag{9}$$

where  $n_e$  represents the valence electron density,  $\omega_0 = \sqrt{K_e/m}$  is the resonance frequency of the harmonic oscillator with damping parameter  $\gamma$ ,  $\epsilon_\infty$  is the high frequency dielectric constant, and  $m_e$  and  $e$  are the electron mass and elementary charge, respectively.

While the above description rests on a purely classical model, these resonances are the result of transitions between quantum mechanical energy levels. To account for the fact that electrons are bound in differing states a sum over all electronic resonances and a fraction factor (or oscillator strength) accounting for the number of electrons sensitive to the resonance may be introduced into the permittivity description

$$\epsilon[\omega] = \epsilon_\infty + \frac{n_e e^2}{m_e \epsilon_0} \sum_j \frac{f_j}{(\omega_j^2 - \omega^2 - i\gamma\omega)}. \tag{10}$$

The resonance frequency  $\omega_j$  corresponds to a transition between two states with energy difference  $\Delta E = \hbar\omega_j$ . The oscillator strength  $f_j$  is then the probability of the transition related to the transition dipole moment from the ground state  $|0\rangle$  to the excited state  $|j\rangle$

$$f_j = \frac{2}{3} \frac{\omega_j m_e}{\hbar e^2} |\langle 0|\mu|j\rangle|^2 \tag{11}$$

with transition dipole operator  $\mu = e\mathbf{r}$ .

### 3.1.3. Drude description for the free carrier response

For delocalized free-carrier absorption the permittivity can be expressed in terms of the Drude model, where in the absence of a restoring force Equation (9) reduces to

$$\epsilon[\omega] = \epsilon_\infty - \frac{\omega_p^2}{\omega(\omega + i\gamma_0)}, \quad (12)$$

where

$$\omega_p^2 = \frac{n_e e^2}{\epsilon_0 m^*}. \quad (13)$$

The linear response of electrons is then governed by their characteristic collision/scattering rate  $\gamma_0 = \tau^{-1}$  and plasma frequency  $\omega_p$ , with  $m^*$  the electron effective mass for the material. The Drude free electron response can be seen as a special case of a relaxor model with hypothetical resonance frequency at DC (i.e., a heavily over-damped electron plasma).

### 3.1.4. Vibrational polarization

In the following, we describe the light–matter interaction phenomena that can occur as a result of a material's vibrational mode. For the case of molecules, these can be spatially localized (e.g., a bond) vibrational modes, or spatially delocalized phonon modes in periodic crystalline materials. We begin by considering a microscopic polarization that can be induced through the application of an external time varying electromagnetic field

$$\mathbf{p}[t] = \mathbf{p}_p + \overleftrightarrow{\alpha} \mathbf{E}_0[t] \quad (14)$$

with permanent dipole moment (if present)  $\mathbf{p}_p$ , optical polarizability tensor  $\overleftrightarrow{\alpha}$ , and the incident electric field  $\mathbf{E}_0[t]$  oscillating at angular frequency  $\omega = 2\pi\nu$ .

The vibrational nuclear motion around an equilibrium position is described in terms of a set of normal coordinates  $Q_N$  with resonance frequencies  $\nu_N$  depending on material composition and symmetry. For small oscillation amplitudes in the harmonic oscillator approximation, the atomic motion along the normal coordinate directions can be expressed as

$$Q_N[t] = Q_{N0} \cos[\omega_N t] \quad (15)$$

with amplitude  $Q_{N0}$ .

The lattice vibration may independently induce a change in both the optical polarizability and the dipole moment. The polarizability may be expanded around the equilibrium normal coordinate  $x_E$

$$\alpha_{ij}[Q] = \alpha_{ij}[x_E] + \sum_N \left( \frac{\partial \alpha_{ij}}{\partial Q_N} \right)_{x_E} Q_N + \dots \quad (16)$$

Similarly, the dipole moment may be expressed as

$$\mathbf{p}[Q] = \mathbf{p}[x_E] + \sum_N \left( \frac{\partial \mathbf{p}}{\partial Q_N} \right)_{x_E} Q_N + \dots \quad (17)$$

Combining Equations (15)–(17), the time-dependent dipole moment is given by

$$\begin{aligned}
 \mathbf{p}[Q] = & \mathbf{p}[x_E] + \underbrace{\sum_N \left( \frac{\partial \mathbf{p}}{\partial Q_N} \right)_{x_E} Q_{N0} \cos[\omega_N t]}_{\text{IR}} + \underbrace{\overleftrightarrow{\alpha}[x_E] \mathbf{E}_0 \cos[\omega t]}_{\text{Elastic}} \\
 & + \underbrace{\left( \sum_N \left( \frac{\partial \overleftrightarrow{\alpha}}{\partial Q_N} \right)_{x_E} Q_{N0} \cos[(\omega \pm \omega_N)t] \right) \frac{\mathbf{E}_0}{2}}_{\text{Raman}} + \dots .
 \end{aligned} \tag{18}$$

The different terms in Equation (18) can be interpreted as different optical interactions between the medium and the light. The first term simply represents the static, permanent dipole moment. The second term encompasses IR active vibrational modes which are given by the dipole moment derivative with respect to the normal coordinate. The third and fourth terms in Equation (18) comprise elastic and inelastic scattering events. Elastic Rayleigh scattering is described by the third term, while the fourth term represents inelastic Raman scattering.

### 3.2. Optical selection rules

In this section, we discuss in more detail the properties of the light–matter interaction, in particular, their tensorial characteristics which provide the rich specificity and symmetry selectivity of the optical response. We will revisit several of these processes again in later sections where we will discuss specific implementations of these different spectroscopies in *s*-SNOM.

#### 3.2.1. Linear optics

As described in Eq. (1), the linear optical polarization depends on a second-rank susceptibility tensor which we denote  $\overleftrightarrow{\chi}^{(1)}$ , with tensor elements

$$\chi^{(1)} = \begin{pmatrix} \chi_{xx}^{(1)} & \chi_{xy}^{(1)} & \chi_{xz}^{(1)} \\ \chi_{yx}^{(1)} & \chi_{yy}^{(1)} & \chi_{yz}^{(1)} \\ \chi_{zx}^{(1)} & \chi_{zy}^{(1)} & \chi_{zz}^{(1)} \end{pmatrix}. \tag{19}$$

While generally  $\chi_{ij}^{(1)} = 0$  for  $i \neq j$ , these off-diagonal elements can acquire imaginary values for optically active (chiral) materials or magnetic materials. Crystals can be categorized based on the relationships between the diagonal elements. If  $\chi_{xx}^{(1)} = \chi_{yy}^{(1)} = \chi_{zz}^{(1)}$  the crystal is isotropic, if  $\chi_{xx}^{(1)} = \chi_{yy}^{(1)} \neq \chi_{zz}^{(1)}$ , the crystal is uniaxial, and if  $\chi_{xx}^{(1)} \neq \chi_{yy}^{(1)} \neq \chi_{zz}^{(1)}$  the crystal is biaxial. The anisotropic susceptibility tensor gives rise to a wavelength- and polarization-dependent material response. This results in the well-known phenomena of birefringence (off-resonance) and dichroism (near or on resonance) for uniaxial crystals, which can be probed through changing the orientation of the polarization and wavevector with respect to the crystallographic axes. This effect is wholly anisotropic (called trirefringence and trichroism) for biaxial crystals.

Birefringence is typically detectable over a broad wavelength range, but is often a small effect. A larger contrast can be obtained in the IR, by tuning the frequency to be resonant with a phonon mode of the material. This provides a means to study variations in crystallographic orientation.

#### 3.2.2. Raman scattering

In addition to the elastic scattering term in Equation (18), the inelastic scattering term gives rise to the Raman response for the *N*th normal mode, expressed as the induced dipole moment in the

form

$$p_N = \left( \frac{\partial \overleftrightarrow{\alpha}}{\partial Q_N} \right)_{x_E} Q_{N0} \cos[(\omega \pm \omega_N)t] \frac{E_0}{2}. \tag{20}$$

Thus, in addition to the elastic Rayleigh scattering at frequency  $\omega$  discussed above, sidebands occur at  $\omega \pm \omega_N$  with the frequency shift  $\omega_N$  corresponding to the normal mode frequency (Figure 6). Although this is a wavemixing mechanism between a photon and a lattice vibration, due to the linear dependence of the inelastically scattered intensity on the excitation intensity it is a linear optical process. Our discussion focuses on Raman scattering from optical phonon modes [107,124], but can readily be generalized to any excitation that produces a similar modulation of the polarizability.

The function  $\overleftrightarrow{R}_N = (\partial \overleftrightarrow{\alpha} / \partial Q_N)_{x_E}$  characterizing the material response is known as the Raman tensor. The sidebands at  $-\omega_N$  and  $+\omega_N$  are the Stokes and anti-Stokes shifts and correspond to the creation and annihilation of phonons of that frequency, respectively. Since for most modes near room temperature  $\hbar\omega_N > k_B T$ , the thermal population of excited modes and thus the probability of an anti-Stokes event is correspondingly small.

The induced polarization for the  $N$ th phonon mode is given in terms of the tensor components  $R_{N,ij}$

$$\begin{pmatrix} p_{N,x} \\ p_{N,y} \\ p_{N,z} \end{pmatrix} = \begin{pmatrix} R_{N,xx} & R_{N,xy} & R_{N,xz} \\ R_{N,yz} & R_{N,yy} & R_{N,yz} \\ R_{N,zx} & R_{N,zy} & R_{N,zz} \end{pmatrix} \times \begin{pmatrix} E_{in,x} \\ E_{in,y} \\ E_{in,z} \end{pmatrix}. \tag{21}$$

Since the symmetries of all expected phonon modes and the corresponding Raman tensors can be determined from the crystallographic space group of a material, Raman scattering can directly probe crystal symmetry and orientation. If the crystal symmetry is known, desired phonon modes can be targeted and studied under specific experimental conditions. Conversely, the observation of specific Raman modes in a given geometry can be used to determine crystallographic orientation.

Unlike molecules which exhibit spatially localized vibrational modes at discrete energy levels, phonons arise from the collective lattice vibrations due to the periodic unit cell arrangement. As a quasiparticle, these modes follow a well-defined dispersion relationship and carry momentum. Momentum conservation of the phonon–photon interaction has two significant consequences. First, due to small photon wavevectors only phonon modes with small wavevectors (i.e., near the center of the Brillouin zone) are probed. Secondly, additional considerations emerge in terms of the vectorial nature of the phonon propagation. In the case of polar phonon modes (those which are also infrared active), the macroscopic electric field associated with the phonon oscillation modifies the

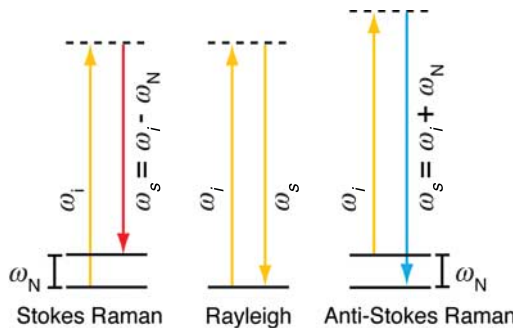


Figure 6. Schematics of the Raman scattering process. In contrast to elastic Rayleigh scattering, Stokes and anti-Stokes Raman scattering involve a frequency shift of the incident light to lower and higher frequencies, respectively, corresponding to the excitation or emission of, e.g., a vibrational quantum.

restoring force, resulting in a propagation direction-dependent phonon frequency. Specifically, for modes whose propagation direction  $\xi$  is parallel to the phonon polarization direction (longitudinal optical, LO) the frequency is found to be higher than that for modes for which  $\xi$  is perpendicular to the polarization direction (transverse optical, TO). As a result, an energy splitting arises between the TO and LO modes [107].

From momentum conservation of the incident  $k_i$  and scattered  $k_s$  light, the phonon propagation direction  $q$  is given as  $q = k_i - k_s$ . Then, if  $q \parallel \xi$  the LO mode is excited, while for  $q \perp \xi$  the TO mode is selected. Through an appropriate use of the TO–LO splitting as discussed below, additional crystallographic information can be gained.

### 3.2.3. Nonlinear optics

The light–matter interactions discussed thus far have all been linearly related to the incident electric field. However, for intense incident electric fields, the polarization induced in a material will have a nonlinear dependence on the incident field, as described in Equation (2) [111]. These nonlinear effects arise due to the induced polarization generating an internal electric field which can modify the interaction of the applied field with the material itself. This can also be thought of as a change in the interaction potential experienced by the excited electron, assuming an effective anharmonic oscillator behavior.

The  $\overleftrightarrow{\chi}^{(n)}$  in the expansion in Equation (2) are susceptibility tensors describing the physical material response to the incident electric and magnetic fields, analogous to the linear case. These tensors increase in rank with the increasing order of the optical process, and by Neumann’s principle possess at least the symmetry of the crystallographic point group of the material [110]. They may also possess additional symmetry, due to changes in selection rules and additional degrees of freedom associated with the number of photons involved in the excitation. Nonlinear techniques therefore provide a powerful means for probing symmetry in the form of crystallographic and magnetic structure and associated phonon, electronic, and spin transitions.

### 3.2.4. Second-harmonic generation

The lowest-order nonlinear response term in the power-series expansion with respect to the electric field,

$$P^{(2)}[2\omega] = \epsilon_0 \overleftrightarrow{\chi}^{(2)} E^2[\omega] \tag{22}$$

describes second-harmonic generation (SHG), where two photons of frequency  $\omega$  combine to produce one photon of frequency  $2\omega$ . In the most general case,  $\overleftrightarrow{\chi}^{(2)}$  is a third rank polar tensor with elements  $\chi_{ijk}$ , where  $i, j,$  and  $k$  are the Cartesian coordinates  $x, y,$  and  $z$ . The notation can be simplified due to permutation symmetry to

$$\begin{pmatrix} P_x[2\omega] \\ P_y[2\omega] \\ P_z[2\omega] \end{pmatrix} = \epsilon_0 \begin{pmatrix} \chi_{xxx} & \chi_{xyy} & \chi_{xzz} & \chi_{xyz} & \chi_{xzx} & \chi_{xyx} \\ \chi_{yxx} & \chi_{yyy} & \chi_{yzz} & \chi_{yzy} & \chi_{yzx} & \chi_{yyx} \\ \chi_{zxx} & \chi_{zyy} & \chi_{zzz} & \chi_{zyz} & \chi_{zxz} & \chi_{zyx} \end{pmatrix} \times \begin{pmatrix} E_x^2[\omega] \\ E_y^2[\omega] \\ E_z^2[\omega] \\ 2E_y[\omega]E_z[\omega] \\ 2E_x[\omega]E_z[\omega] \\ 2E_x[\omega]E_y[\omega] \end{pmatrix} \tag{23}$$

with  $E_x, E_y, E_z$  the electric field components of the incident light, and all the Cartesian coordinates defined with respect to the crystal axes of the sample.

By consideration of the crystallographic symmetry of the material, it is possible to determine the allowed components of the susceptibility tensor for all of the 32 crystal groups. In the 11 crystal point groups with inversion symmetry  $\overleftrightarrow{\chi}^{(2)} = -\overleftrightarrow{\chi}^{(2)} \equiv 0$ , so that the bulk SHG response is forbidden in the dipole approximation, where higher-order multipole contributions to the nonlinear response are neglected [110]. Thus, liquids, gases, and amorphous solids will not produce SHG in the bulk. However, surfaces and interfaces inherently break inversion symmetry and SHG can be a sensitive probe of interfacial processes [125], for example, adsorption [126], chemical reactions [127], and melting [128]. Non-centrosymmetric crystal groups will additionally produce a bulk SHG response. SHG is therefore ideal for probing FE materials, which are inherently non-centrosymmetric due to the lattice structural symmetry-breaking associated with the spontaneous formation of a permanent electric dipole. However, depending on the material and susceptibility components, the surface and bulk SHG may be comparable in magnitude, and are often difficult to distinguish [129,130].

The symmetry sensitivity of SHG also provides access to magnetic ordering phenomena. Spin ordering breaks *time inversion symmetry*, which allows magnetic-field induced SHG contributions [131–133], denoted MSHG or the nonlinear magneto-optical Kerr effect (N-MOKE) [134,135]. The spin symmetry is described by an *axial* tensor, denoted  $\chi^{(c)}$  (or  $\chi^{(\text{magn})}$ ) in contrast to the usual time-invariant polar crystallographic tensor  $\chi^{(i)}$  [136]. This can incorporate spontaneous or magnetic field-induced magnetization effects. The strength of the MSHG signal and its parity with respect to magnetization depends on the incident polarization with respect to the direction of magnetization [137]. Many magnetic materials possess a center of inversion and therefore bulk SHG is dipole forbidden. However, MSHG allows the investigation of surface magnetism and also interfacial magnetism in multilayer structures, systems of high technological interest [138,139]. Importantly, because the magnetic response arises from symmetry considerations rather than a net magnetic moment, SHG is sensitive even to a-FM ordering, which is difficult to probe in general [140].

The total SH response in a magnetically ordered material is then the sum of crystallographic and magnetic components:

$$P_i[2\omega] \propto (\chi_{ijk}^{(i)} + \chi_{ijk}^{(c)})E_{jk}^2[\omega]. \quad (24)$$

Since the symmetries of the  $\chi_{ijk}^{(i)}$  and  $\chi_{ijk}^{(c)}$  contributions are usually different, it is often possible to distinguish their contributions through polarization anisotropy measurements. They will also exhibit different spectral behavior [51].

In lossless media  $\chi^{(i)}$  is real, and  $\chi^{(c)}$  is imaginary, so there is no interference between the two contributions [131,141]. However, the tensors are complex for absorbing media, leading to interference, i.e.

$$I[2\omega] \propto (|\chi^{(i)}|^2 + |\chi^{(c)}|^2 \pm 2|\chi^{(i)}||\chi^{(c)}|\cos(\phi))E^4[\omega] \quad (25)$$

with  $\phi$  the phase between the spin and crystallographic responses. Reversing the spin direction leads to a 180° phase shift, so that the sign of the interference term is also reversed and the overall intensity is altered. The same principle applies to the reversal of the direction of spontaneous polarization in a FE crystal. This allows the distinction of even anti-parallel domain structures (magnetic, a-FM, and FE), which is not possible with incoherent techniques such as phonon Raman scattering.

### 3.2.5. Other nonlinear optical techniques

SHG can be considered the degenerate case of a three wave mixing process. More generally, the induced polarization can radiate at any frequency which is a linear combination of the frequencies

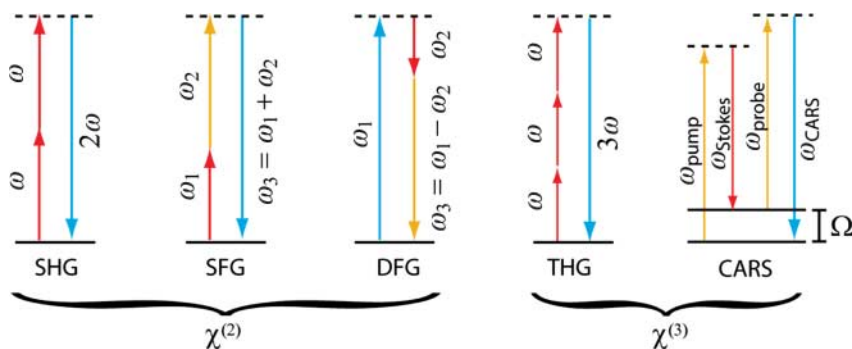


Figure 7. Common nonlinear optical interactions and their energy-level diagrams. SHG, sum frequency generation (SFG), and difference frequency generation (DFG) are second-order processes. Third-harmonic generation (THG) is the degenerate case of four wave mixing and is a third-order process. Coherent anti-Stokes Raman scattering (CARS) is the coherent third order analog to Raman spectroscopy.

of the incident waves, so that

$$P[\omega_3] = \epsilon_0 \overset{\leftarrow}{\chi}^{(2)} E[\omega_1] E[\omega_2]. \tag{26}$$

This allows for sum-frequency generation (SFG) with the energy conservation condition  $\hbar\omega_3 = \hbar\omega_1 + \hbar\omega_2$  and difference frequency generation (DFG) corresponding to  $\hbar\omega_3 = |\hbar\omega_1 - \hbar\omega_2|$ , including the degenerate case of optical rectification, and similarly for higher-order processes (see Figure 7). Electro-optical and magneto-optical effects can also be viewed as nonlinear optical mixing in the limit where one of the field components has zero frequency, i.e. is a DC or slowly varying field.

SFG has been employed extensively for imaging biological structures and for chemical analysis [142,143]. Both SFG and DFG allow the choice of input frequencies  $\omega_1$  and  $\omega_2$  over a broad energy range, enabling tuning to an electronic, vibrational, or quasiparticle resonance in a sample in order to gain additional, e.g. magnetocrystalline and chemical sensitivity [144–146]. In its doubly resonant (DR) implementation SFG allows for the determination of electron–electron or electron–phonon interaction by exciting multiple coupled vibrational or electronic resonances [147].

Four wave mixing (FWM) techniques are based on the third-order optical susceptibility  $\chi^{(3)}$ . Since these are odd-order processes, they are permitted for all materials, including centrosymmetric point groups. Third-harmonic generation at  $3\omega$  provides symmetry and spectroscopic information about excitations of both odd and even parity [148–150]. Coherent anti-Stokes Raman scattering (CARS) is a type of resonant FWM [151], with energy conservation  $\omega_{\text{CARS}} = \omega_{\text{pump}} + \omega_{\text{probe}} - \omega_{\text{Stokes}}$ . As a coherent process, this enables the chemical sensitivity of Raman scattering in combination with the symmetry sensitivity of nonlinear spectroscopy. Multi-dimensional spectroscopy further provides a means to probe anharmonic potentials and intra-system coupling [152,153].

#### 4. Optical microscopy: Far-field imaging

Optical microscopy is experimentally appealing, being compellingly simple compared to X-ray or electron-based microscopies, and readily applicable under ambient and atmospheric conditions. Suitable coherent and incoherent light sources are available over a wide spectral range, and with short pulse durations can provide simultaneous ultrafast temporal resolution. Thus, far-field microscopy and micro-spectroscopy have found a range of applications for the investigations of

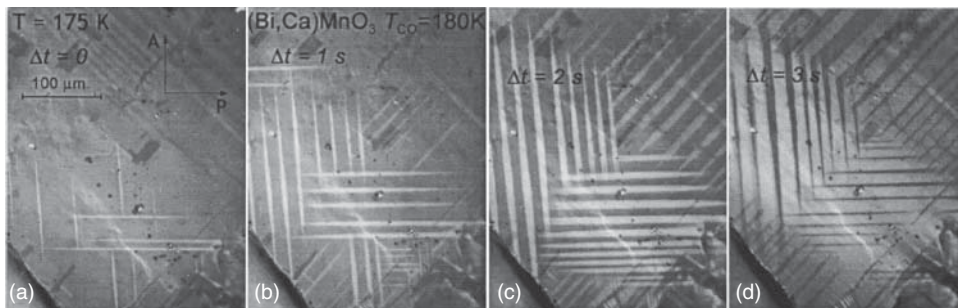


Figure 8. Temporal evolution of the CO phase of  $\text{Bi}_{0.2}\text{Ca}_{0.8}\text{MnO}_3$  when cooled below the transition temperature, with contrast due to its birefringence measured by polarized microscopy. Bright regions correspond to the structurally distorted CO domains, which display high optical anisotropy. The CO domains nucleate and grow within the cubic parent lattice (dark regions). From V. Podzorov *et al.*, Phys. Rev. B 64 (2001), p. 140406 [156]. Copyright 2001 by the American Physical Society.

correlated electron materials, despite the spatial resolution being insufficient in most cases to directly study mesoscopic properties.

Although far-field microscopy is not the focus of this review, in this section, we provide some representative examples that highlight some of the valuable insights optical imaging can provide on the microscale. We focus, in particular, on vibrational Raman microscopy and nonlinear second-harmonic microscopy, which provide unique phonon, crystallographic, and ferroic order information likely to be relevant to the study of strongly correlated matter on the nanoscale. After a discussion of the limitations of far-field microscopy in terms of spatial resolution, we will extend the discussion of these techniques into their corresponding near-field implementations in the subsequent sections.

#### 4.1. Optical microscopy techniques

##### 4.1.1. Birefringence and dichroism microscopy

Linear optical measurements can probe crystal anisotropy and associated differences in electronic and lattice structure. By studying optical birefringence in a polarizing microscope configuration, it is possible to gain information about, e.g., crystal orientation and strain, and it is widely used as a standard identification technique in biology and mineralogy [154]. Magnetic effects also produce birefringence [155], as discussed in subsequent sections. In correlated materials, coexisting phases will typically display different indices of refraction and optical absorption properties, which may be significant enough to allow imaging of the growth and nucleation of domains [156,157]. An example of this is shown in Figure 8, where coexisting CO and cubic PM phases in  $\text{Bi}_{0.2}\text{Ca}_{0.8}\text{MnO}_3$  appear as bright and dark regions, respectively. The appearance of the CO phase is characteristic of a martensitic transition, with the cooperative motion of atoms producing a different crystal structure, rather than a long-range diffusion-type phase transition [158]. The CO phase is highly distorted due to strain interactions, and therefore has large birefringence and appears bright in observation with  $90^\circ$  crossed polarizer and analyzer.

##### 4.1.2. Raman microscopy

Raman scattering provides chemical fingerprinting and material identification through the measurement of vibrational modes, which has long positioned it as a powerful analytical tool. The invention of the laser significantly facilitated Raman spectroscopy, which quickly emerged

as a simple means to measure specific zone center phonon frequencies [159–162] due to the tensor-based selection rules and accelerated theoretical developments [163,164]. The vibrational frequencies probed directly reflect lattice structure and material composition, and consequently are highly sensitive to perturbations in the crystal lattice arising from phase transitions or strain [165–167]. The capability to study structural phase transitions in complex oxides was established early, for example in  $\text{VO}_2$  [168]. Raman spectroscopy also provides direct access to soft modes associated with displacive phase transitions [169], allowing for the study of phase transitions in e.g. quartz [170],  $\text{BaTiO}_3$  [164,171], and other perovskites [172].

Experimentally, Raman scattering is performed using a monochromatic illumination source, and the spectral sidebands corresponding to the inelastically scattered light are measured. Spectral rejection of the laser line from the weaker Raman signal can be achieved with a multi-grating monochromator or dielectric filters. The use of a multi-grating monochromator is necessary to resolve Raman lines from low-frequency modes such as acoustic phonons (Brillouin scattering), albeit at the expense of signal intensity. The combination of dielectric filters with a simple single grating spectrometer provides higher sensitivity but typically limits the detection to higher frequency phonons.

Even with effective suppression of the excitation light, the typically small Raman scattering cross-sections lead to low signal levels that complicate detection and measurement of micrometer-scale samples or sample features [173]. In order to improve the spatial resolution and signal collection efficiency, confocal Raman microscopy has emerged as a widespread characterization tool [174], with high numerical aperture microscope objectives providing spatial resolution down to the diffraction limit and simultaneously increasing the collection efficiency. Micro-Raman has found widespread applications in both the study of isolated nanostructures and the spatially resolved study of bulk crystals and thin films.

In particular, as discussed below, micro-Raman spectroscopy has been essential for many studies of the carbon allotropes of carbon nanotubes and graphene [175]. It has furthermore been widely applied for the structural and chemical identification of semiconductor nanostructures [176, 177] and complex oxides exhibiting phase transition behavior [178,179].

Finite size effects on the phase transition behavior and their relation to domain formation [178] and phonon confinement [180,181] has been another area of interest. Optical crystallography can be performed, identifying the FE domain structure of  $\text{BaTiO}_3$  based on the polarization anisotropy of the Raman response [182]. Applications to correlated electron systems such as superconductors and multiferroics have also become commonplace via either vibrational interactions [183] or magnons [184]. However, the study of isolated nano-crystals of sub-diffraction volume size are prone to very weak signals. Furthermore, in the conventional backscattering geometry, as necessary to achieve appreciable signal levels, the degrees of freedom in terms of tensor elements that can be probed are limited, thus restricting the specificity with respect to crystal symmetry. New implementations with increased spatial resolution, higher sensitivity, and crystallographic selectivity are thus highly desired.

#### 4.1.3. *Second-harmonic generation microscopy*

As discussed in Section 3.2.3, nonlinear optical techniques provide access to spectroscopic, crystallographic, and magnetic information not accessible in linear interactions. Furthermore, nonlinear imaging provides high contrast [185], making it ideal for imaging a wide variety of materials, from biological samples to correlated electron materials. The nonlinear response can vary by several orders of magnitude more than the linear response within a sample, particularly close to resonances, and the frequency difference between incident and detected photons allows for efficient background suppression, providing highly selective and specific contrast.

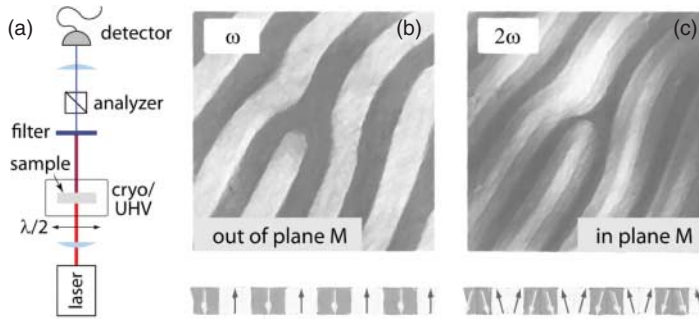


Figure 9. Basic transmission set-up for imaging domain structures with SHG (a). The sample environment may be cryogenic UHV, or strong magnetic field. Magnetic domains in a magnetic garnet thin film, resolved using the linear Faraday effect (b) and MSHG in transmission (c). SHG can detect the in-plane component of the magnetization, allowing much more sensitive determination of the magnetization direction. The image is  $50 \mu\text{m} \times 50 \mu\text{m}$ . Figure (b) and (c) after V. Kirilyuk *et al.*, *Appl. Phys. Lett.* 70 (1997), pp. 2306–2308 [139]. Copyright 1997 American Institute of Physics.

The experimental implementation of second-harmonic generation (SHG) imaging requires careful consideration of incident  $k$ -vector direction, input and output polarization, and relative crystal orientation in order to select specific  $\chi_{ijk}$  components sensitive to the properties of interest. While the SHG response can provide high contrast, signal levels are typically low due to the nonlinear nature of the process, and pulsed laser sources are required. Effective spectral filtering is needed to reject the fundamental light from the SHG radiation. A simple set-up for SH spectroscopic and polarization measurement in transmission is shown in Figure 9(a). Here, the input and output polarization are controlled, and detection is performed with a photodiode, PMT or CCD, depending on the spectroscopic or imaging application. Amplitude and polarization are usually measured, but the phase of the SH response can also be determined through interference with a known reference beam or between different contributions to the SH response. This phase-sensitivity allows domain imaging in a wide range of e.g. ferroic materials. Additionally, with this implementation the sample environment can readily be controlled. This can be an important consideration, operating, for example, in vacuum to avoid oxidation and allow cooling to cryogenic temperatures, as desired for probing of correlated phenomena.

SHG is sensitive to FE, FM, and a-FM order and these properties can be independently probed through their different symmetry susceptibility components. From Equation (25), a reversal in the spin orientation or spontaneous polarization direction will lead to a  $180^\circ$  phase shift. The phase sensitivity of SHG then produces destructive interference at anti-parallel domain walls [186]. This phase contrast can also be converted to an intensity contrast by interfering with a reference SH beam, for example, generated from a  $c$ -cut quartz crystal [187–189]. FE domain imaging using these properties has been performed in, e.g.,  $\text{LiNbO}_3$ ,  $\text{LiTaO}_3$ , and  $\text{BaTiO}_3$  [190–194]. SHG has also been used to study the poling, growth, and topology of domains in bulk crystals and Langmuir–Blodgett films [187,193,195,196].

The same principles apply to magnetic SHG domain imaging, with the phase determining the obtainable contrast in the MSHG image. The use of MSHG has several advantages over linear magneto-optical techniques. Typically the crystallographic and magnetic contributions to the overall SH signal are comparable in magnitude, unlike linear techniques where the magnetic response is very small. The latter leads to only small polarization anisotropy through the magneto-optical Faraday or Kerr effects, with birefringence of often less than  $1^\circ$ . Therefore, in order to map

magnetic domains with linear optics, very precise polarization control and contrast improvement through e.g., lock-in detection or background subtraction is necessary.

A comparison of wide-field MSHG and linear magneto-optical imaging in a magnetic garnet thin film is shown in Figure 9 [139]. This measurement was performed in transmission, with the same system used and detection of either the fundamental  $\omega$  light or the SHG  $2\omega$  light to construct the image. For the detected fundamental light, a “labyrinth-type” domain structure can be resolved through the birefringent Faraday effect. However, this geometry is only sensitive to the component of magnetization perpendicular to the film surface. The MSHG image reveals additionally the in-plane component of the magnetization, from the interference between the bulk crystallographic and magnetization-induced contributions to the SHG signal. From the MSHG image, it is possible to deduce that each of the linear up and down domains consists of two subdomains with tilted magnetization directions [197].

As mentioned earlier, the sensitivity of SHG to any form of symmetry breaking, including that of time-reversal, allows the imaging of domains in even a-FM crystals. This has been demonstrated in materials such as NiO, CoO, KNiF<sub>3</sub>, and Cr<sub>2</sub>O<sub>3</sub> [198]. However, several of these materials belong to centrosymmetric crystallographic point groups, so that the interference required for domain imaging arises from a different mechanism than that between the crystallographic and magnetic contributions to SH, described in Equation (25). In the case of NiO, this is the interference with the bulk magnetic dipole response of the material [145]. For Cr<sub>2</sub>O<sub>3</sub>, circularly polarized light was used to produce interference between real and imaginary components of the susceptibility tensor and allow domain imaging [199]. This is shown in Figure 10. This allowed resolution of all six possible a-FM domain configurations associated with the spin flop transition in Cr<sub>2</sub>O<sub>3</sub>. The a-FM vector usually lies along the optical ( $z$ )-axis of the crystal, but for external magnetic fields  $>5.8$  T the spins flop into the basal  $xy$  plane, with three possible orientations.

One of the greatest strengths of SHG for probing correlated materials is its sensitivity to several ferroic orders simultaneously. This allows probing of multiferroic materials in order to investigate the relationship between, for example, the FE and (a-)FM domains. An example of this is shown in Figure 11, in the hexagonal manganite YMnO<sub>3</sub>. FE domain contrast (left), a-FM domain contrast (center), and coupled FE and a-FM domains (right) in poled YMnO<sub>3</sub> are enabled through selection

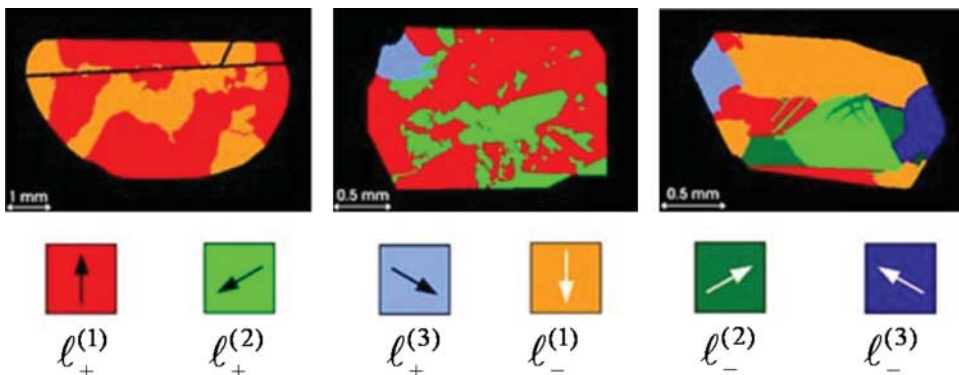


Figure 10. SHG imaging, with false color labeling, of a-FM domains in Cr<sub>2</sub>O<sub>3</sub> after the spin flop transition for three different samples. The six possible domain configurations, with  $\pm$  a-FM vector oriented at 0°, 120°, and 240° with respect to the  $y$ -axis, are shown. The sample on the left shows 180° domains for spins oriented along  $y$ . The middle sample exhibits all three a-FM orientations, for the + domain. Finally, the sample at right has all six configurations. Adapted from M. Fiebig *et al.*, Phys. Rev. B 54 (1998), p. 681 [199]. Copyright 1998 by the American Physical Society.

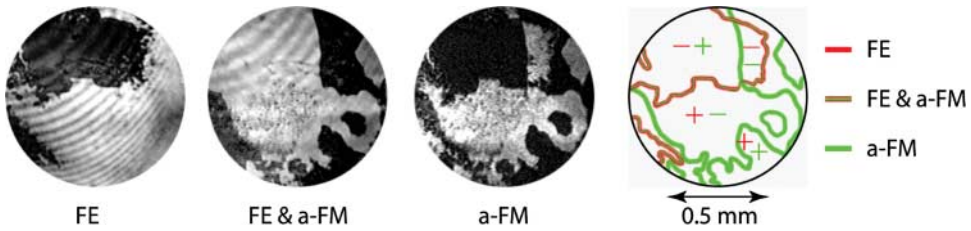


Figure 11. SHG imaging of FE, a-FM, and coupled domain structure in  $\text{YMnO}_3$ . From comparison of the a-FM and FE images, it is possible to see that a change in the FE domain orientation coincides with a change in a-FM domain orientation, a characteristic of the magneto-electric coupling in this intrinsic multiferroic material. The schematic on the right shows the clamped (red/green line) and free (green line) a-FM domain walls. Reprinted by permission from Macmillan Publishers Ltd: M. Fiebig *et al.*, *Nature* 419 (2002) p. 818, copyright 2002 [68].

of the appropriate tensor components. In this case, according to symmetry considerations, the FE response should only be visible for fundamental or SHG polarization in the  $z$ -direction, and the a-FM response requires  $x$  or  $y$  polarized light. However, the magneto-electric coupling of the response leads to the presence of an a-FM response (established through spectroscopic behavior) even for  $z$ -polarized light, allowing simultaneous resolution of both ferroic responses with  $k \parallel y$  (discussed in more detail in Section 6).

Since FE and (a-)FM domains are usually small compared to the wavelength of light, a poling of large regions of the material is necessary for the domain visualization, so that information regarding the intrinsic domain size and orientation is usually lost in far-field measurements. However, SHG provides the unique capability for non-perturbative, contactless direct imaging of FE and a-FM domains simultaneously making its extension into the nanoscale very desirable.

#### 4.2. Far-field diffraction limit

A discussion of near-field imaging is incomplete without a summary of the limitations of far-field microscopy. The achievable spatial resolution in far-field microscopy is limited by both the aberration and diffraction of the optics in the imaging system and the general loss in  $k$ -vector information in the transition from the evanescent near- to propagating far-field. While aberration effects may be corrected through improvements in the quality of the imaging optics, the resolution limit for optical microscopy in its typical implementation is defined by the diffraction limit [200,201]. This arises as a consequence of the wave-like nature of light as it passes through the finite sized apertures of the optical imaging elements.

The limit on the spatial resolution of a given imaging system may be derived by considering the field emitted by a point source and the field collected to form an image at the image plane of an optical system. The momentum distribution of light emitted by a point source is composed of a continuum of all spatial frequency (wave-vector) components  $k_x$ ,  $k_y$ , and  $k_z$ , with  $z$  the propagation direction [28].

Far-field free space propagating modes are defined by the energy–momentum dispersion relation  $\omega/k = c$ . As a consequence, waves with wavevector components greater than the free-space wavevector  $k$  ( $k_x^2 + k_y^2 + k_z^2 > |\mathbf{k}|^2$ ) are evanescent ( $\text{Im}[k_z]$ ) and attenuate quickly with distance  $z$ . The propagation of light to the image plane thus effectively acts as a low-pass momentum-space filter removing any contributions from evanescent solutions in the reconstruction of the image of the point source. Therefore, when the remaining propagating momentum contributions recombine the image, the image is blurred compared to the original source. If the light is spatially filtered by another aperture of diameter  $D$  at a distance  $f$  from the source (e.g., a lens), then the  $k_x$  and  $k_y$

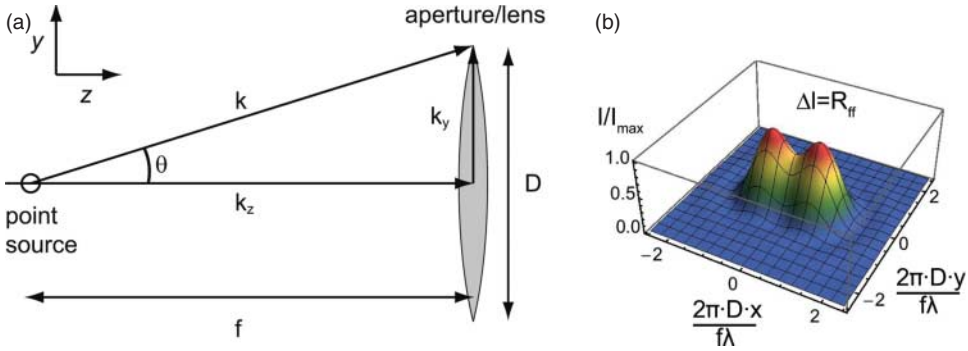


Figure 12. Geometric relationship between point source optical emitter and a far-field collection lens with diameter  $D$ , at a distance  $f$  from the point source (a). Diffraction and Airy distribution for two point sources with separation at the Rayleigh limit  $R_{ff}$  (b).

components are further limited by the collection aperture of the lens. The ability to distinguish two point emitters separated by  $\Delta l$  in the far-field depends on the bandwidth of the spatial frequency components  $\Delta k^2 = \Delta k_x^2 + \Delta k_y^2$  (including positive and negative frequencies) and is limited by  $\Delta k \Delta l = 1$ .

The description for the resolution attainable through an optical microscope was realized early in the development of the modern microscope, with first formulation by Abbe [200]. Within the paraxial approximation,  $\sin \theta \approx \tan \theta = D/2f = k_y/k_z$ , with  $k_z \approx k$  (Figure 12(a)). This leads to a minimum distance at which two point sources can be separated and distinguished from one another

$$l_{\min} = \frac{1}{\Delta k_y} = \frac{2\lambda f}{\pi D} = \frac{\lambda}{\pi \text{NA}}, \tag{27}$$

where  $\text{NA} = \sin[\theta] \approx D/2f$  is the numerical aperture of the system.

The Rayleigh criterion is the most commonly used form of the diffraction limit, and is based on the Airy disk spatial pattern of diffraction through a circular aperture. Here,  $l_{\min}$  is determined by the distance at which the maximum of the Airy distribution of one point source overlaps the minimum of the Airy distribution of the second point source [201]. The angular diffraction described by the Airy function has a minimum located at approximately  $\sin[\theta_{\min}] = 1.22\lambda/D = l_{\min}/f$ , with  $l_{\min}$  the distance from the maximum of the intensity distribution to the first minimum. This then defines the resolution for a particular imaging system  $R_{ff} = l_{\min}$ , as shown in Figure 12(b).

Even using short-wavelength light with high NA objectives, the spatial resolution is in practice limited to a few hundred nanometers. This problem is exacerbated in the mid-IR spectral range where many phonon and low-energy carrier excitations in solid state occur, and where far-field resolution is limited to several micrometers, even using coherent synchrotron or infrared laser sources [202–204]. In order to overcome the limited resolution of far-field imaging, it is necessary to be sensitive to the large wavevector evanescent light contributions, which is the realm of near-field microscopy discussed in the next section.

### 5. Optical microscopy: near-field imaging

In this section, we describe the near-field light–matter interaction for the purpose of sub-diffraction limited spatial resolution imaging. We specifically address the optical response of the tip and coupled tip-sample system for the two most common *s*-SNOM implementations, which are differentiated by the significance of the tip scattering and near-field coupling effects, as discussed

in footnote 1. Typically, in linear elastic  $s$ -SNOM, scattering dominates, while in tip-enhanced implementations such as Raman and nonlinear optics the plasmonic field enhancement plays a significant role. These different  $s$ -SNOM implementations lead to different experimental considerations. As a result, we discuss the choice of feedback mechanism, scanning probe tips, extraction of the near-field signal, and application of various optical spectroscopies in this context.

### 5.1. Fundamental principles of near-field microscopy

The concept of an experimental apparatus with optical contrast and spatial resolution below the diffraction limit is typically dated back to a proposal by E.H. Syngé in the late 1920s [205,206]. The idea of Syngé was to achieve sub-diffraction limited imaging using the transmission of light through a small ( $\sim 10$  nm) metallic aperture to illuminate an object placed in close proximity. Unfortunately, due to the technological limitations at that time, Syngé was unable to implement his proposal. The experimental challenges were fourfold: (1) a sufficiently intense light source is needed, (2) the sample needs to be positioned with nanometer scale precision, (3) the sample surface must be sufficiently flat, and (4) an opaque plate or film with a small aperture needs to be fabricated.

With the evolution of more advanced scientific instrumentation and fabrication techniques, all of these obstacles were eventually overcome. Lasers provided the desired intense illumination source. Sub-nanometer spatial control could be achieved through the use of piezo-electric scanner-positioners, which enabled the development of different scanning probe microscopy techniques as a platform for the near-field microscope. Finally, advances in sample preparation and micro-fabrication techniques eventually allowed for the development of suitable near-field probes, which replaced Syngé's need for a small aperture plate.

Following first demonstrations in the microwave regime [207], the experimental realization of Syngé's proposal for sub-diffraction limit spatial resolution in the optical regime was achieved in 1983 by Pohl *et al.* [2]. The technique, initially dubbed "optical stethoscopy", utilized a metal-coated quartz crystal with a sharpened ( $\sim 30$  nm) tip apex as near-field probe. By pressing the quartz crystal against a surface, the metal coating at the sharp crystal tip deformed to create a small aperture. Scanning the aperture across a grating test structure, a spatial resolution of 25 nm could be determined [2].

Parallel developments led to the STM [91] and subsequently to the AFM [99,100]. These techniques allow for the precise control of the tip height above a sample surface via either tunneling current or atomic force feedback with precision down to the atomic scale. This major advance in nanoscale characterization was soon combined with and adapted for sub-diffraction optical imaging to yield the first spatial characterization of evanescent fields at optical frequencies [208].

Following the arrival of scanning probe microscopy, small aperture probes were developed by applying a metal coating to tapered optical fiber tips [3,7,8]. These fiber-based small aperture probes, held close to a surface of interest by scanning probe feedback, enabled the technique then widely known as NSOM or SNOM (Figure 13(b)). Here, the small aperture in the metal coating of the fiber tip acts as the practical realization of the aperture in an opaque slide proposed by Syngé, with the additional advantage that it allows for facile optical excitation via the optical fiber.

Different NSOM/SNOM measurement techniques and spectroscopic implementations have been applied towards the characterization of a wide variety of material systems. However, the approach has a limited spectral range as the optical fiber generally restricts wavelengths to the visible to near-infrared regimes. Furthermore, the small amount of light transmitted through the probe aperture further limits resolution and sensitivity attainable via NSOM. As described by Bethe in 1944, the total power of light transmission  $P_{\text{trans}}$  through a small aperture of radius  $a$  in a metallic

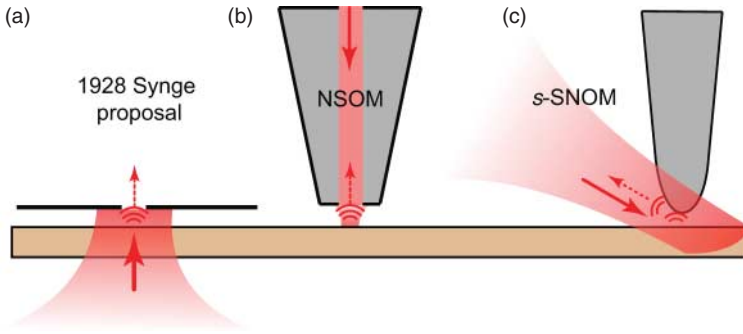


Figure 13. The experimental schematic for Syngge’s original 1928 proposal for sub-diffraction imaging based on a sub-wavelength size aperture (a). Schematics of the general experimental implementations for aperture-based NSOM based on a tapered optical fiber (b), and scattering-based *s*-SNOM near-field microscopy (c).

film is given by [209]

$$P_{\text{trans}}(\lambda, a, E_{\text{inc}}) = \underbrace{\frac{64}{27\pi} \left(\frac{2\pi a}{\lambda}\right)^4 a^2}_{\sigma_{\text{eff}}} \cdot \underbrace{\frac{c}{2} \varepsilon_0 E_{\text{inc}}^2}_{\text{incident irradiance}}, \quad (28)$$

where  $c/2 \cdot \varepsilon_0 E_{\text{inc}}^2$  represents the incident irradiance on the aperture and the term  $\sigma_{\text{eff}}$  is the effective transmission cross-section of the aperture.

The rapid and nonlinear decrease in aperture transmission with its decreasing diameter means that an increase in spatial resolution of NSOM comes at the expense of a severe signal decrease. In most practical cases, this limits the spatial resolution of NSOM to  $\simeq 50\text{--}100$  nm. Furthermore, with the transmitted power scaling as  $\propto (1/\lambda)^4$  the extension into the infrared spectral range proved difficult, even with appropriate infrared transparent fiber materials. Despite a wide range of efforts to improve fiber and aperture designs, signal limitations, and other fundamental challenges including fiber dispersion and imaging artifacts,<sup>2</sup> NSOM in general has not lived up to initial expectations. While it has found a range of applications for routine sample characterization, intrinsic limitations of NSOM have triggered the search for alternative approaches for near-field microscopy.

One general limitation in achieving ultrahigh optical spatial resolution that needs to be overcome is the following: With increasing spatial resolution  $\delta$ , the sample volume probed will decrease ( $\propto \delta^2$  to  $\delta^3$  depending on dimensionality of the sample in terms of surface versus bulk signal), leading to a decrease in the optical signal for a given illumination intensity. A mechanism is thus desired by which the sensitivity would, ideally intrinsically, increase with increasing spatial resolution. The apertureless or scattering-type near-field microscopy approach discussed in the following section meets that requirement.

### 5.1.1. Scattering-scanning near-field optical microscopy

The concept of scattering or apertureless near-field optical microscopy was developed throughout the 1990s using both STMs [9,10] and AFMs [10–12]. Initial demonstrations, showing that a sharp scanning probe tip as a near-field scatterer can provide high optical spatial resolution, laid the groundwork for the technique of *s*-SNOM. Spatial resolution beyond the diffraction limit is provided by the enhancement and spatial field localization of the incident far-field radiation at

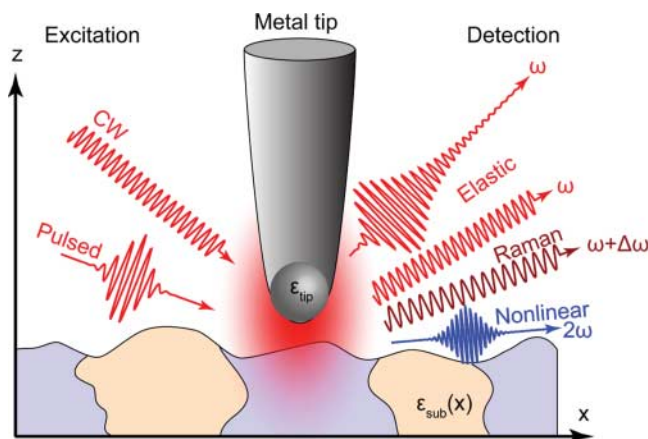


Figure 14. In *s*-SNOM, continuous wave and pulsed optical excitations drive a near-field coupled tip–sample polarization via the field localization and enhancement provided by the tip apex (via antenna or plasmonic resonances, analogous to the DC lightning rod effect). Different tip-scattered and radiated signals are shown, including elastic, inelastic, e.g. Raman, ultrafast, and nonlinear processes, that provide spectroscopic near-field imaging contrast after suitable far-field and background subtraction, with spatial resolution to first order determined by the tip apex radius.

the tip apex and scales with apex radius to first order. Conceptually, the high optical resolution is enabled by the large wavevector components of the near-field of the apex, which are projected via scattering into detectable far-field radiation. This gives spectroscopic access to the optical properties of the sample surface on nanometer length scales.

A wide range of different optical and spectroscopic techniques can readily be implemented, providing elastic, inelastic, and nonlinear optical imaging contrast, each with its own unique capabilities and advantages. Figure 14 illustrates the localized field enhancement surrounding the AFM/STM tip, generated by the incident light field, giving rise to scattered light from the nanoscale tip–sample coupled interaction volume in the form of, for example, elastic scattering, inelastic Raman scattering, the ultrafast free induction decay of surface vibrational or electronic oscillators, and nonlinear wavemixing.

*s*-SNOM implementations are generally differentiated based on the degree of field enhancement achieved at the tip apex. For the case of weak field enhancement using non-resonant dielectric or metal-coated tips, the tip primarily serves to scatter the induced near-field of the coupled tip–sample polarization. This is the case in *elastic s*-SNOM. This yields only a weak near-field signal compared to the far-field background, which arises from scattering from sample inhomogeneities and tip shaft illumination by the diffraction-limited focus. In tip-enhanced spectroscopy, the non-linear dependence of the signal on the local field strength, for example, in Raman scattering or nonlinear optics, leads to a relatively weaker background signal.

An understanding of the optical properties of the tip and the nature of the optical interaction with the sample is therefore critical not only in the design of a specific *s*-SNOM experiment, but also for the interpretation of the optical signals. The following sections will thus describe models for the local field enhancement and coupling between the tip and sample. In Section 5.1.2, we discuss the simplest model approximating the tip as a polarizable sphere, which provides a good initial qualitative understanding of the imaging mechanism in elastic *s*-SNOM. Sections 5.1.3 and 5.1.4 are concerned with the large field enhancement generated by noble metal tips exhibiting plasmonic and antenna resonances. The effect of local field enhancement on inelastic and nonlinear

spectroscopic signal levels in tip-enhanced spectroscopy will be discussed using a prolate ellipsoid as a model system.

5.1.2. The coupled dipole model

For *s*-SNOM measurements using elastic light scattering as an optical contrast mechanism, the desirable measurable quantities are the amplitude and phase of the near-field signal. One of the simplest descriptions of the scattering process is to approximate the tip apex as a polarizable sphere above a planar substrate [25,211], as shown schematically in Figure 15(a). This model qualitatively captures the tip–substrate coupling and yields a simple analytic formula for the resulting effective polarizability to describe the imaging contrast. We consider the sphere, composed of the same material as the tip and with frequency-dependent dielectric permittivity  $\epsilon_{\text{tip}}[\omega]$ , separated from the surface by a distance  $d$ . In the presence of the incident optical electric field  $\mathbf{E}_{\text{inc}}$ , the resulting induced optical polarization  $\mathbf{p}_{\text{sph}} = \overleftrightarrow{\alpha}_{\text{sph}} \epsilon_0 \mathbf{E}_{\text{inc}}$  can be expressed in terms of the Clausius–Mosotti relation for the polarizability  $\overleftrightarrow{\alpha}_{\text{sph}}$  of a dielectric sphere in air, given by

$$\alpha_{\text{sph},ij} = 4\pi r^3 \left( \frac{\epsilon_{\text{tip}} - 1}{\epsilon_{\text{tip}} + 2} \right) \delta_{ij}. \tag{29}$$

The matrix representation is used to account for the polarization dependence. While the polarizability of an isolated sphere is isotropic, the substrate surface differentiates the coupling of in-plane (*s*-polarized) and out-of-plane (*p*-polarized) polarizations.

We first consider the case for *p*-polarized light corresponding to an electric field of  $\mathbf{E}_{\text{inc}} = E_{\text{inc}} \hat{z}$ . The fields associated with the resulting surface charge distribution are equivalently described by a hypothetical image dipole of relative strength  $\beta = (\epsilon_{\text{surf}} - 1)/(\epsilon_{\text{surf}} + 1)$ , located a distance of  $-d$  beneath the substrate surface. As a result of this sphere–substrate coupling, the effective polarization arises from the incident electric field and the image field [212] and can then be expressed as

$$p_{\text{eff},z} = \alpha_{\text{sph},z} \left( 1 + \frac{\alpha_{\text{eff},z} \beta}{2\pi (2d)^3} \right) \epsilon_0 E_{\text{inc},z} = \alpha_{\text{eff},z} \epsilon_0 E_{\text{inc},z}. \tag{30}$$

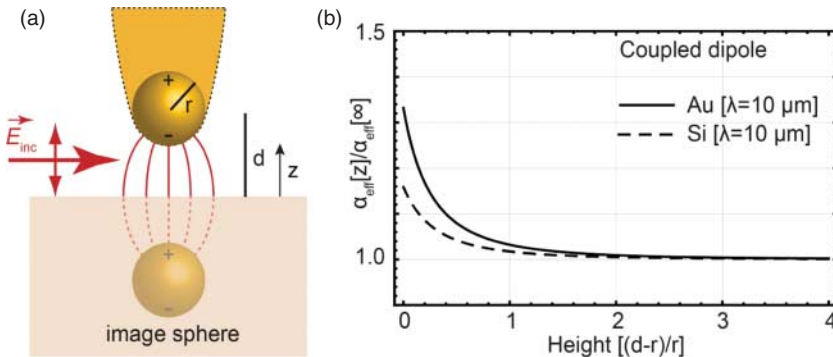


Figure 15. Model of effective polarizability of coupled tip–sample system approximating the tip as a sphere with radius  $r$  and tip–sample separation  $d$  and subject to an external field  $E_{\text{inc}} \hat{z}$  (a). Different coupling to Au and Si substrates with sphere–sample separation as illustrated here underlies the material-dependent contrast achievable in elastic *s*-SNOM (b).

The relation for  $\alpha_{\text{eff},z}$  given in Equation (30) can be solved to yield an expression for the out-of-plane effective polarizability for the tip–sphere:

$$\alpha_{\text{eff},z} = \alpha_{\text{sph},z} \left( 1 - \frac{\alpha_{\text{sph},z} \beta}{16\pi d^3} \right)^{-1}. \quad (31)$$

The associated optical field enhancement in the gap between the sphere and the substrate surface at a height  $z$  (for  $z < d$ ) can correspondingly be expressed as a sum of the field contributions originating from the incident external field, the dipole moment of the tip, and its image dipole:

$$\begin{aligned} E_{\text{tot},z}[z] &= E_{\text{inc},z} + E_{\text{sph},z} + E_{\text{imsph},z} \\ &= \left( 1 + \frac{\alpha_{\text{eff},z}}{16\pi(d-z)^3} + \frac{\alpha_{\text{eff},z}\beta}{16\pi(d+z)^3} \right) E_{\text{inc},z}. \end{aligned} \quad (32)$$

In contrast to  $p$ -polarized incident field, for  $s$ -polarized  $\mathbf{E}_{\text{inc}} = E_{\text{inc}}\hat{\mathbf{x}}$ , the image dipole of the tip aligns antiparallel to the tip dipole. Here, the relation for the effective polarizability of the tip–sphere in the in-plane direction is given by

$$p_{\text{eff},x} = \alpha_{\text{eff},x} \epsilon_0 E_{\text{inc},x} = \alpha_{\text{sph},x} \left( 1 + \frac{\alpha_{\text{eff},x}\beta}{4\pi(2d)^3} \right) \epsilon_0 E_{\text{inc},x}. \quad (33)$$

This yields an effective polarizability in the in-plane direction of

$$\alpha_{\text{eff},x} = \alpha_{\text{sph},x} \left( 1 - \frac{\alpha_{\text{sph},x}\beta}{32\pi d^3} \right)^{-1}. \quad (34)$$

The corresponding field in the tip–sample gap region at a height  $z$  can be expressed as

$$\begin{aligned} E_{\text{tot},x}[z] &= E_{\text{inc},x} - E_{\text{sph},x} + E_{\text{imsph},x} \\ &= \left( 1 - \frac{\alpha_{\text{eff},x}}{32\pi(d-z)^3} + \frac{\alpha_{\text{eff},x}\beta}{32\pi(d+z)^3} \right) E_{\text{inc},x}. \end{aligned} \quad (35)$$

Note that for an  $s$ -polarized incident electric field, the polarizability and field in the tip–sample gap are also increased, but to a much smaller extent than in the case of a  $p$ -polarized incident field.

As an example, Figure 15 shows the normalized polarizability of a tip approaching Si and Au substrates for excitation at  $\lambda = 10 \mu\text{m}$ , with similar behavior at any off-resonant wavelength. While an increase in polarizability is observed for both systems at a distance comparable to the apex radius, a larger increase is seen for the case of Au. The difference in coupling with sensitivity to the dielectric function of the sample constitutes the general contrast mechanism in  $s$ -SNOM.

### 5.1.3. Field enhancement and local field factor

In most  $s$ -SNOM spectroscopy measurements the detected signal exhibits a nonlinear dependence on the local field, with both incident field and induced polarization experiencing a field enhancement at the tip. The field in the immediate vicinity of a structure or surface will experience a local variation  $\mathbf{E}_{\text{loc}}[\omega]$  arising from a modification of the incident field  $\mathbf{E}_{\text{inc}}[\omega]$  through the Fresnel factor, by local geometric features, or in general from the intrinsic and extrinsic optical properties

and resonances of the material. The field enhancement factor  $F[\omega]$  can be defined as

$$F(\omega) = \frac{\mathbf{E}_{\text{loc}}[\omega]}{\mathbf{E}_{\text{inc}}[\omega]}. \quad (36)$$

For an  $n$ th order optical process (nonlinear if  $n > 1$ ) with corresponding polarizability tensor  $\overleftrightarrow{\alpha}^{(n)}$ , the induced optical polarization at frequency  $\omega_{\text{out}}$  can be written as

$$\mathbf{p}[\omega_{\text{out}}] = \overleftrightarrow{\alpha}^{(n)} F[\omega_1] \mathbf{E}_{\text{inc}}[\omega_1] \cdots F[\omega_n] \mathbf{E}_{\text{inc}}[\omega_n]. \quad (37)$$

The field radiated by the induced polarization will experience an additional enhancement [213,214] by a factor of  $F[\omega_{\text{out}}]$ , leading to an effective radiating polarization of

$$\mathbf{p}_{\text{eff}}[\omega_{\text{out}}] = \mathbf{p}[\omega_{\text{out}}] F[\omega_{\text{out}}]. \quad (38)$$

For the detected intensity  $I_{\text{out}} \propto \mathbf{p}_{\text{eff}}^2$  we find

$$I_{\text{out}} \propto (F[\omega_{\text{out}}] \prod_n F[\omega_n])^2. \quad (39)$$

Therefore, for a linear optical process where  $n = 1$

$$I_{\text{out}} \propto (F[\omega_{\text{out}}] F[\omega_{\text{in}}])^2. \quad (40)$$

Note that the field enhancement factors are in general frequency dependent.  $F[\omega_{\text{in}}]$  and  $F[\omega_{\text{out}}]$  can only be approximated as equal if the frequency difference between incident and detected light is small compared to their spectral variations. In this case, for a linear optical process, this gives rise to an approximately fourth-power dependence of the  $s$ -SNOM signal with field enhancement. That nonlinear scaling in field enhancement is a key contributor to the high sensitivity of  $s$ -SNOM in its different implementations and is responsible for signal contrast even at very high spatial resolution, as opposed to aperture-based NSOM. The dependence on input laser power, however, is unchanged and scales linearly or nonlinearly depending on spectroscopic application, as in the far-field case.

#### 5.1.4. Plasmonic field enhancement

The tip-sample coupling model discussed above need to be expanded further to account for specific material and geometry-dependent antenna or plasmon resonances of the tip [215]. Plasmonic resonant structures and materials are characterized by wavelength-dependent features with large amplitude and with a strong shape dependence, unlike the relatively weak wavelength dependence of the optical properties of, for example, Pt or Si  $s$ -SNOM tips. From Equation (29), it can be seen that for a sphere in air/vacuum, if  $\text{Re}(\epsilon_{\text{tip}}[\omega]) = -2$ , the polarizability exhibits a resonant enhancement. For the case of noble metals, where this condition is met in the visible spectral range, this corresponds to the localized surface plasmon resonance (LSPR) for spherical particles. The LSPR can be viewed as a result of a restoring force in the collective free electron motion, arising from the geometric constraints of finite size particles [216]. In general, for nanoparticles or quasi-infinite tips, however, the spectral LSPR position depends on their shape and size [217].

Owing to this complex shape- and size-dependent behavior, the LSPR and associated local field enhancement are typically calculated numerically [218–221]. However, the truncation of the semi-infinite tip shape for finite element methods can introduce numerical artifacts and calculations are time-consuming. Therefore, in order to develop an understanding of the plasmon resonant

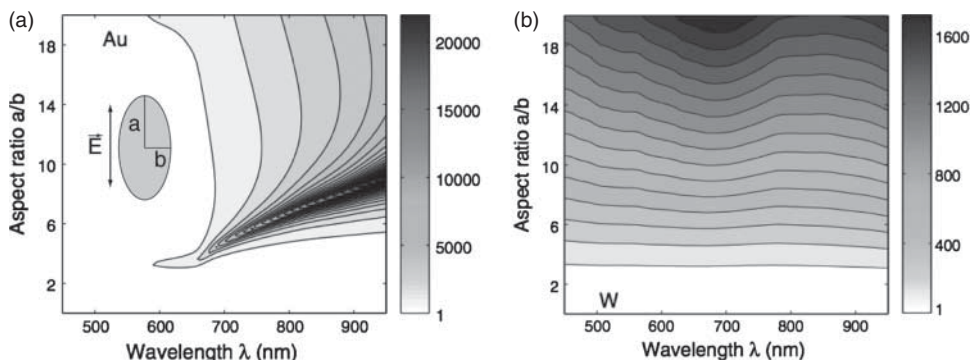


Figure 16. Polarizability of a gold prolate ellipsoid with varying aspect ratio  $a/b$  showing the characteristic plasmon-resonant behavior and a red-shift with increasing aspect ratio (a). Values are normalized to a non-resonant spherical particle. In contrast, a prolate W ellipsoid exhibits no plasmon resonance, and about an order of magnitude weaker field enhancement and a flat spectral response (b). Adapted from C.C. Neacsu *et al.*, *Appl. Phys. B* 80 (2005), pp. 295–300 [215]. With kind permission from Springer Science and Business Media.

behavior of noble metal structures, simple analytical models that readily reveal the underlying relevant structural and material parameters can be used, albeit at the expense of quantitative accuracy [222].

In order to examine the general features of plasmon resonances and their dependence on geometric and material parameters, we approximate the tip as a prolate ellipsoid [215] with dielectric function  $\epsilon_{\text{tip}}$  embedded in a dielectric medium  $\epsilon_{\text{d}}$ . The polarizability of the ellipsoid along the major axis  $a \parallel z$  and with minor axis  $b$  is given by [216]

$$\alpha_{\text{ell},z} = \frac{4\pi ab^2}{3} \left( \frac{\epsilon_{\text{tip}} - \epsilon_{\text{d}}}{\epsilon_{\text{d}} + A_i(\epsilon_{\text{tip}} - \epsilon_{\text{d}})} \right). \quad (41)$$

The depolarization factor  $A_i$  is a function of  $a$  and  $b$  and approaches  $\frac{1}{3}$  for  $a = b$  [216], reducing Equation (41) to the Clausius–Mosotti relation for a sphere (Equation (29)). The polarizability is directly related to the local field enhancement via the particle volume  $F[\omega] \simeq \alpha[\omega]/V$ .

Figure 16(a) shows the relative polarizability of a prolate Au ellipsoid in air as a function of aspect ratio, calculated using experimental dielectric values [223]. The polarizability exhibits the expected resonant behavior and associated field enhancement in the visible spectral range, a property which can be exploited for increasing sensitivity in surface-enhanced Raman scattering (SERS) and tip-enhanced Raman scattering (TERS). With increasing aspect ratio a continuous redshift of the resonance peak is observed as well as an associated narrowing of the spectral peak position due to decreased material ohmic damping as the resonance is tuned away from the Au interband transition. For comparison, the relative polarizability for W is shown in Figure 16(b) with a flat and featureless spectral response expected for non-plasmon resonant behavior.

Owing to the frequency-dependence of  $F[\omega]$ , appropriate illumination wavelengths must be selected for maximum field enhancement. For the case of Au tips, typical resonances are found to be in the red to near-IR spectral range [215]. Ag tips generally exhibit a blue-shifted resonance. Ag can provide larger values of the polarizability and thus field enhancement compared to Au, due to reduced Drude damping [223]. However, due to the deterioration of Ag under ambient conditions, Au is more commonly used.

Since tip plasmon resonances have Q-factors on the order of 10, for SHG or large Raman shifts  $F[\omega_{\text{in}}] \neq F[\omega_{\text{out}}]$  in general. However, in particular, for the case of Raman scattering with frequency

shifts less than the plasmon linewidths,  $F[\omega_{\text{in}}] = F[\omega_{\text{out}}]$  often provides a good approximation. This relates to the common assumption in SERS and TERS of  $I_{\text{Raman}} \propto |F|^4$  [224].

For the case of a tip, as for an ellipsoidal structure, the field enhancement not only shows a strong frequency dependence but also a polarization anisotropy due to the structural asymmetry [218]. This arises from an increased polarizability along the tip axis ( $p$ -polarized) compared to the perpendicular ( $s$ -polarized) case. Measured  $p$ -polarized TERS enhancement values of up to  $|F|^4 \sim 10^4$ – $10^5$  are typical for free-standing tips (see, e.g., [225] and references therein). This is in good agreement with theoretical predictions of  $F \simeq 10$ – $50$  [218,219,221,222,226,227] for typical apex radii of 10–20 nm.

In addition to the enhancement due to the tip itself, further field enhancement results from the evanescent coupling of the tip to a metallic substrate [222]. This can provide an additional up to tenfold field enhancement, yielding  $F$  values of up to  $\sim 100$ . This effect is critical in for single molecule sensitivity of TERS and enhanced signal levels in  $s$ -SNOM in general.

## 5.2. Experimental considerations and implementations of $s$ -SNOM

There are many experimental considerations that enter into the design of an  $s$ -SNOM experiment, guided by a combination of resonant and non-resonant field enhancement and tip-scattering, and sample dielectric and resonant properties. A wide variety of commercial tips for scanning probe applications which are suitable for  $s$ -SNOM applications are available. Focused ion-beam milling (FIB), lithography, or electrochemical etching can be applied for more specific tip fabrication and modification. The type of sample, desirable optical process, and choice of tip dictate the most suitable tip–sample distance control feedback mechanism, with contact or dynamic cantilever or tuning fork-based AFM techniques possible, including contact, non-contact, or shear force feedback.

This section also covers the general experimental implementations of both elastic  $s$ -SNOM and tip-enhanced spectroscopy. In particular, near-field demodulation and amplification techniques in elastic  $s$ -SNOM are addressed. Similarly, the tensor-based selection rules as they apply to TERS and SHG for the study of crystalline materials are described.

### 5.2.1. Scanning probe tips for $s$ -SNOM

As discussed above, the choice of tip for near-field scattering and field-enhancement is guided by intrinsic (e.g., optical dielectric material response) and extrinsic (e.g., geometry, or plasmon and antenna resonances) optical properties of the tip. For elastic  $s$ -SNOM, where the tip oscillation in tapping or dynamic non-contact AFM modes is necessary for background demodulation as discussed in Section 5.2.4, conventional Si and  $\text{Si}_3\text{N}_4$  cantilever AFM tips can often be used. Since the cantilever itself can frequently obscure the free line of sight, it is important that the tip apex is visible to the illumination and detection optics. As an example, two commonly used commercially available cantilever tips with good apex visibility are shown in Figure 17: Bruker OTESPA (a) and Nanosensors ATEC-NC (b). To obtain increased signal levels Pt- or Au-coated tips provide larger (non-plasmon resonant) optical polarizability, but often have increased apex radius compared to uncoated variants. It is also possible to use carbon nanotube functionalized tips [228,229].

The use of plasmon resonant tips in  $s$ -SNOM provides additional local field enhancement. This approach is particularly suitable for the combination of  $s$ -SNOM with intrinsically weak, yet spectroscopically highly selective optical processes such as Raman or nonlinear optical spectroscopy. In the following, we provide a summary of the key considerations for the fabrication and use of plasmonic tips.

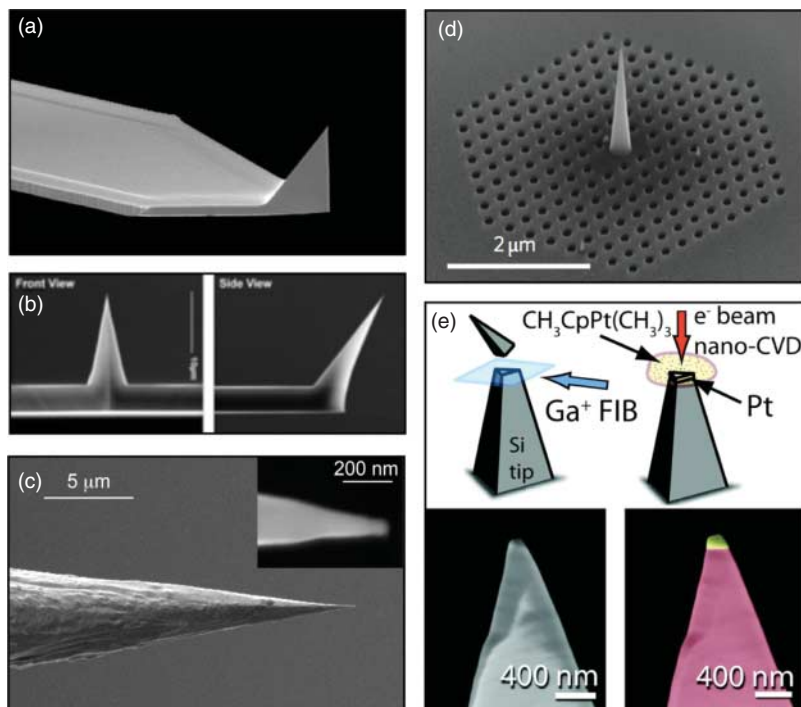


Figure 17. SEM images of various tips for *s*-SNOM applications. Commercially available tips, e.g. Bruker OTESPA (a) and Nanosensors ATEC-NC (b). Electrochemically etched polycrystalline Au tip produced via a DC etch process using HCl / Ethanol [230] (c), inset: high-resolution image of the tip apex. Photonic crystal for light concentration to a central CVD-grown tip from Ref. [231] (d). Modified commercial tip with modification for improved *s*-polarization sensitivity (e). Figure (e) adapted from R. Olmon *et al.* Phys. Rev. Lett. 105 (2010), p. 167403 [232]. Copyright 2010 by the American Physical Society.

As the spectral characteristics and amplitude of the LSPR depend sensitively on the material and shape of the tip, reproducible fabrication of noble metal scanning probe tips with nanometer structural precision is required. From the discussion on elliptical particles in Section 5.1.4, a larger degree of elongation (i.e., sharper tips) produces a larger local field enhancement. Various methods for the fabrication of plasmonic Au and Ag tips have been explored and developed, including thermal vapor deposition of metals onto commercially available tips [233–235], electrochemical etching [236–238], focused ion-beam (FIB) milling [27], and template stripping [239]. Thermal evaporation of noble metals onto commercial tips is a common technique due to the relative ease of tip fabrication, but despite recent technical improvements in the process, achieving consistent field-enhancement has remained challenging [235,240,241].

Several tip fabrication procedures developed for STM tips [242], based on electrochemical etching involving the anodic dissolution of a metal wire immersed in an electrolytic solution, can be adapted for the fabrication of *s*-SNOM tips. Through the choice of metal, electrolyte, solvent, and voltage (DC versus AC), high reproducibility can be achieved. For Au, hydrochloric acid is commonly used as the electrolyte, where the  $\text{AuCl}_4^-$  complex facilitates the transport of Au ions away from the wire while the formation of  $\text{H}_2$  provides the necessary reducing environment to avoid metal oxidation. Although not strictly necessary [238], the etching solution is frequently diluted with ethanol to reduce surface tension [230,236]. Using a DC voltage and a solution of ethanol and concentrated HCl in a 1:1 ratio, tips can be fabricated with apex radii down to 10 nm.

An AC voltage without ethanol can also yield TERS-active tips with smooth surfaces. Reduced surface roughness can be achieved by annealing the Au wire prior to etching [238]. Shown in Figure 17(c) is an SEM image of an electrochemically etched Au tip with a smooth surface and a small tip apex radius. Suitable etching techniques for Ag are still underdeveloped. The main procedures are based on  $\text{HClO}_4$  and  $\text{NH}_4\text{OH}$  as electrolytes [237,243].

Template stripping appears as a particularly effective means to obtain smooth tips with nanometer spatial control [239,244]. Tips can also be fabricated by attaching plasmonic nanoparticles to dielectric tips [245,246].

Tip designs for special *s*-SNOM applications have been fabricated via lithographic and ion-beam processes. FIB milling in particular allows high structural control [15]. Various tip designs have been explored to improve field enhancement for plasmon-enhanced spectroscopies [247,248]. Novel tip designs have even been explored to improve background suppression using a nanofocusing mechanism based on plasmonic mode compression in a photonic crystal and subsequent nanofocusing into a tip, as shown in Figure 17(d) [231]. It is also possible to fabricate tips for elastic *s*-SNOM via electron beam-assisted chemical vapor deposition in combination with focused ion beam milling (FIB) to improve in-plane (*s*-polarized) polarization sensitivity [232] (Figure 17(e)).

### 5.2.2. Tip-sample distance control

For cantilever-based tips it is possible to use conventional AFM feedback mechanisms. Contact mode in particular minimizes the tip-sample separation leading to maximum field enhancement at the surface [241], but can lead to rapid tip deterioration and sample perturbations [249–251]. Improved tip performance and durability can be achieved through the use of protective coatings [240]. Tapping and dynamic non-contact AFM modes minimize tip deterioration, and allow demodulation of the weak near-field signal in elastic *s*-SNOM, but also diminish the enhancement duty cycle [235,252].

For tip-enhanced spectroscopy, the primary consideration is to maximize the time-averaged local field enhancement, calling for a scanning probe feedback mechanism that maintains the tip in close proximity to the sample (large duty cycle). Furthermore, electrochemically etched tips cannot readily be mounted onto AFM cantilevers. Such etched tips are suitable for STM with no additional processing [18,237,253,254], and STM offers the advantages of sub-nanometer tip-sample separation leading to high field enhancement. The requirement for conductive samples, however, renders STM unsuitable for insulating and semiconducting crystalline materials, although a conductive surface layer may be used [255].

An alternative to STM for electrochemically etched tips is shear-force AFM (sf-AFM), which maintains a constant tip-sample separation at a distance of a few nanometers. Developed specifically for near-field imaging [256] the sf-AFM feedback mechanism is based on the viscous damping experienced by a tip located within a few nm and oscillating parallel with respect to a sample surface [257]. Metal wire or fiber tips are generally mounted onto a high-Q quartz tuning fork, with the oscillation amplitude detected via electrodes deposited onto the tines of the fork. Tip oscillation parallel to the sample surface and small amplitudes on the order of 1 nm [257] allow the tip to be held at a constant and close tip-sample separation, while avoiding physical contact.

### 5.2.3. Focusing optics

Additional considerations arise in terms of the illumination and detection optics used, where it is desirable to maximize the NA to achieve minimal illumination focus size in order to reduce the

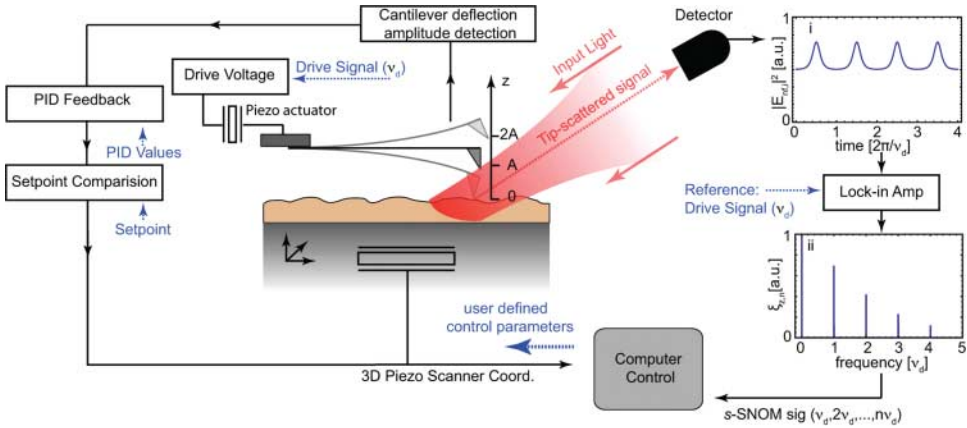


Figure 18. General schematic of linear optical *s*-SNOM measurements. Illustrated is the combination of dynamic force feedback of the AFM, correlated with the detection of the optical signal with different harmonics of the tip-dither frequency ( $\nu_d, 2\nu_d, \dots, n\nu_d$ ).

background and to maximize signal collection efficiency [173]. While high NA can be achieved with oil immersion objectives in combination with beam-shaping techniques in axial illumination [258,259], the through-sample illumination and detection is unusable in the study of opaque samples. For opaque or thick samples, side illumination is typically employed, with NA  $\sim 0.5$  the practical limit achievable with conventional optics. In order to achieve a higher NA, parabolic mirrors [260,261] or top illumination [254] can be used.

5.2.4. *Linear elastic light scattering in s-SNOM*

Since the elastic *s*-SNOM signal is generally weak, and *a priori* difficult to separate from the far-field background, a modulation scheme must be applied for its discrimination [11,12,19,25]. This is achieved in the dynamic non-contact AFM mode, where a piezo actuator initiates oscillatory vertical motion of the AFM tip by driving the AFM cantilever at a dither frequency  $\nu_d$  near the fundamental flexural resonance frequency. The resulting vertical tip motion with an amplitude of tens of nanometers periodically modulates the near-field interaction [262].

An experimental layout for linear optical *s*-SNOM is shown in Figure 18. The light is focused onto the tip-sample gap, with a focus size that exceeds the nanometer-scale tip-apex emitter area by many orders of magnitude. The tip-scattered light  $E_{nf}$ , despite local field enhancement and antenna effects mediating the coupling of the apex near-field to detectable optical far-field, is in general much weaker than the far-field background  $E_{bg}$ . However, while the near-field interaction scales in tip-sample distance with apex radius as discussed above, the background signal varies comparatively little over that distance. The near-field signal can then be isolated through the use of lock-in detection at both the fundamental and higher harmonics of the tip dither frequency.

The cantilever motion  $z_{tip}[t]$  for typical elastic *s*-SNOM measurements can be approximated as sinusoidal with oscillation amplitude  $A$  and distance of closest approach to the surface  $d$  ( $d = 0$  when in contact with the surface):

$$z_{tip}[t] = A(1 + \cos[\nu_d \cdot t]) + d. \tag{42}$$

As shown in Equation (31), the effective polarizability of the tip and thus the total scattered field is highly dependent on the height above the sample surface. The scattered field can be expanded

in terms of harmonics of  $\nu_d$  (see Figure 18 inset ii),

$$\mathbf{E}_{\text{nf}}[t] = \sum_{n=-\infty}^{\infty} \mathcal{E}_{\text{nf},n} \exp[in\nu_d t]. \quad (43)$$

The quantity  $\mathcal{E}_{\text{nf},n}$  is a complex value, whose absolute value represents the magnitude of the scattered field and whose real and imaginary parts define the phase  $\phi$  of the scattered light:

$$\phi = \arctan \left[ \frac{\text{Im}[\mathcal{E}_{\text{nf},n}]}{\text{Re}[\mathcal{E}_{\text{nf},n}]} \right]. \quad (44)$$

Methods of interferometrically amplifying the  $s$ -SNOM signal and determining its intrinsic phase will be discussed in the following sections.

*Interferometric  $s$ -SNOM signal amplification.* Several challenges exist for the precise determination of the local dielectric sample properties that give rise to the  $s$ -SNOM spectral signal. The scattering geometry itself influences spectral amplitude and phase. In addition, the interference of  $\mathbf{E}_{\text{nf}}$  with the background field  $\mathbf{E}_{\text{bg}}$  gives rise to a “self-homodyne” interference with uncontrolled phase. The superposition of the weak near-field signal component  $\mathbf{E}_{\text{nf}}$  and the large background field  $\mathbf{E}_{\text{bg}}$  each with their own characteristic phases,  $\phi_{\text{nf}}$  and  $\phi_{\text{bg}}$ , respectively, can be described as follows:

$$\mathbf{E}_{\text{det}}[t] = \mathbf{E}_{\text{nf}}[t] \exp[i(\omega t - \phi_{\text{nf}})] + \mathbf{E}_{\text{bg}}[t] \exp[i(\omega t - \phi_{\text{bg}})]. \quad (45)$$

The intensity at the detector may be expressed as

$$I_{\text{det}}[t] = \mathbf{E}_{\text{det}}[t] \mathbf{E}_{\text{det}}^*[t] \quad (46)$$

$$= |\mathbf{E}_{\text{bg}}[t]|^2 + |\mathbf{E}_{\text{nf}}[t]|^2 + 2|\mathbf{E}_{\text{bg}}[t]||\mathbf{E}_{\text{nf}}[t]| \cos[\Delta\Phi], \quad (47)$$

where  $\Delta\Phi = \phi_{\text{bg}} - \phi_{\text{nf}}$  represents the phase difference between the background and near-field signals.

Both  $\mathbf{E}_{\text{nf}}$  and  $\mathbf{E}_{\text{bg}}$  amplitude may be described by a Fourier expansion of the harmonics of the tip-dither frequency, as described in Equation (43). Owing to the long wavelength compared to the tip dither amplitude, the frequency distribution of the background field is largely constrained to the DC ( $n = 0$ ) and fundamental ( $n = 1$ ) frequency ( $|\mathcal{E}_{\text{bg},0}| > |\mathcal{E}_{\text{bg},1}|$ ). In contrast, with dither amplitude comparable to the apex radius, the near-field signal is spread over many harmonics. For  $n = 0$  and 1, the amplitude of the background is greater than or comparable to the near-field signal ( $|\mathcal{E}_{\text{bg},0}| \gg |\mathcal{E}_{\text{nf},0}|$ ,  $|\mathcal{E}_{\text{bg},1}| \simeq |\mathcal{E}_{\text{nf},1}|$ ). At harmonics  $n \geq 2$ , however, the near-field may exceed the background ( $|\mathcal{E}_{\text{bg},n \geq 2}| \ll |\mathcal{E}_{\text{nf},n \geq 2}|$ ). As a result, Equation (46) may be expressed in terms of the dominant background contribution, for demodulation at a specific  $n$  harmonic:

$$I_{\text{det},n}[t] = |\mathcal{E}_{\text{bg},0}|^2 + |\mathcal{E}_{\text{nf},n}[t]|^2 + 2|\mathcal{E}_{\text{bg},0}||\mathcal{E}_{\text{nf},n}[t]| \cos[\Delta\Phi]. \quad (48)$$

The disadvantage in non-interferometric detection is the uncontrolled background phase that can vary as the sample is scanned below the tip. The limitations of self-homodyne amplification can be overcome through the application of a reference field ( $\mathbf{E}_{\text{ref}} \gg \mathbf{E}_{\text{bg}}$ ) of controlled optical phase. Here, the phase of the reference field can be varied by adjusting its optical pathlength, allowing for the implementation of homo- or heterodyne amplification of the near-field signal. Several variants of interferometric  $s$ -SNOM techniques have been developed, each with specific attributes for amplifying the near-field signal and characterizing its phase [19,25,263–265].

In conventional homodyne amplification, both the magnitude and phase of the scattered near-field are determined by measuring the magnitude of the  $s$ -SNOM signal for, e.g., two discrete

reference phases separated by a phase difference of  $\pi/2$ . The total field at the detector can then be expressed as

$$\mathbf{E}_{\text{det}}[t] = \mathbf{E}_{\text{nf}}[t] \exp[i(\omega t - \phi_{\text{nf}})] + \mathbf{E}_{\text{bg}}[t] \exp[i(\omega t - \phi_{\text{bg}})] + \mathbf{E}_{\text{ref}}[t] \exp[i(\omega t - \phi_{\text{ref}})] \quad (49)$$

For most measurements, the homodyne reference field is assumed to exceed the strength of all other signal contributions  $\mathbf{E}_{\text{ref}} \gg \mathbf{E}_{\text{bg}} \gg \mathbf{E}_{\text{nf}}$ . The intensity at the detector may be written as the sum of six terms:

$$I_{\text{det}}[t] = |\mathbf{E}_{\text{ref}}[t]|^2 + |\mathbf{E}_{\text{bg}}[t]|^2 + |\mathbf{E}_{\text{nf}}[t]|^2 + 2|\mathbf{E}_{\text{ref}}[t]||\mathbf{E}_{\text{bg}}[t]| \cos[\phi_{\text{ref}} - \phi_{\text{bg}}] \\ + 2|\mathbf{E}_{\text{bg}}[t]||\mathbf{E}_{\text{nf}}[t]| \cos[\phi_{\text{bg}} - \phi_{\text{nf}}] + 2|\mathbf{E}_{\text{ref}}[t]||\mathbf{E}_{\text{nf}}[t]| \cos[\phi_{\text{ref}} - \phi_{\text{nf}}]. \quad (50)$$

By applying lock-in filtering on  $n\nu_d$ , all terms except the ones that contain the modulated  $\mathbf{E}_{\text{nf}}$  in Equation (50) are suppressed (with the exception of a weak modulation of  $\mathbf{E}_{\text{bg}}$ ). Under the assumption that the reference field is large compared to the background and near-field, the last term in Equation (50) dominates the signal. The resulting detector signal can then be expressed as

$$U_{\text{det},n} = C_{\text{det}} 2|\mathcal{E}_{\text{ref},0}||\mathcal{E}_{\text{nf},n}| \cos[\Delta\Phi]. \quad (51)$$

$\Delta\Phi$  represents the phase difference between the reference and near-field signal, and  $C_{\text{det}}$  is the detector efficiency. While this is similar to the self-homodyne case, both the magnitude and phase of the homodyne arm now represent controllable parameters. Applying two-phase interferometry by measuring the near-field magnitude twice with the reference phase shifted by  $\pi/2$ , both the magnitude and phase of the near-field light may be determined, i.e.

$$\Delta\Phi = \arctan \left[ \frac{U_{\text{det},n}(\phi_{\text{ref}} - \pi/2)}{U_{\text{det},n}(\phi_{\text{ref}})} \right]. \quad (52)$$

*“Pseudo-heterodyne” s-SNOM detection.* As an alternative to the discrete phase variation described above, a continuous phase modulation can be applied to the reference field [19]. This approach also provides for improved background suppression. By modulating the reference phase at frequency  $\nu_r$  the reference field may be expressed as

$$\mathbf{E}_{\text{ref}}[t] = \mathbf{E}_{\text{ref}} \exp[i\gamma \cos[\nu_r t]] \exp[i(\omega t - \phi_{\text{ref}})]. \quad (53)$$

with phase amplitude  $\gamma$ . Decomposing the reference field into its Fourier expansion components, it can be expressed as

$$\mathbf{E}_{\text{ref}}[t] = \left( \sum_{m=-\infty}^{\infty} \mathcal{E}_{\text{ref},m} \exp[im\nu_r t] \right) \exp[i(\omega t - \phi_{\text{ref}})]. \quad (54)$$

The coefficients of the Fourier series are found to be

$$\mathcal{E}_{\text{ref},m} = \mathcal{E}_{\text{ref}} J_m[\gamma] \exp \left[ \frac{im\pi}{2} \right], \quad (55)$$

where  $J_m[\gamma]$  is a Bessel function.

As before, when the reference field is much stronger than any of the background fields  $\mathbf{E}_{\text{ref}} \gg \mathbf{E}_{\text{bg}}$ , any self-homodyne effect of the signal will be suppressed. Neglecting the background field

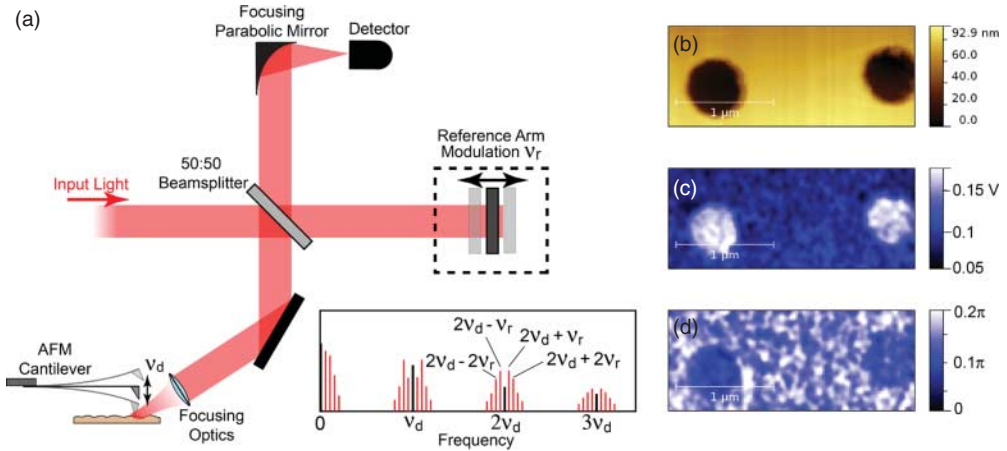


Figure 19. Schematic for interferometric pseudo-heterodyne amplification of near-field *s*-SNOM signals (a), with the inset showing frequency spectrum for demodulation. The AFM dither frequency and reference mirror modulation frequency are denoted by  $\nu_d$  and  $\nu_r$ , respectively. Topography (b), near-field amplitude (c), and phase (d) for a Au/Si calibration grid.

the total intensity at the detector can be expressed in terms of the near-field and reference field as

$$\begin{aligned}
 I_{\text{det}} &= |\mathbf{E}_{\text{nf}} + \mathbf{E}_{\text{ref}}|^2 \\
 &= \left| \left( \sum_{n=-\infty}^{\infty} \mathcal{E}_{\text{nf},n} \exp[in\nu_d t] \right) \exp[i(\omega t - \phi_{\text{nf}})] \right. \\
 &\quad \left. + \left( \sum_{m=-\infty}^{\infty} \mathcal{E}_{\text{ref},m} \exp[im\nu_r t] \right) \exp[i(\omega t - \phi_{\text{ref}})] \right|^2. \tag{56}
 \end{aligned}$$

This gives rise to sideband frequencies  $\nu_{n,m} = n\nu_d + m\nu_r$ . The total detected signal at a sideband frequency  $n\nu_d + m\nu_r$  can then be expressed as

$$U_{\text{det},n,m} = C_{\text{det}} \left( 2(\mathcal{E}_{\text{ref}} \cdot \mathcal{E}_{\text{nf},n}) J_m[\gamma] \cos \left[ \phi_{\text{nf}} - \phi_{\text{ref}} - \frac{m\pi}{2} \right] \right). \tag{57}$$

Shown in Figure 19 is the experimental arrangement of the pseudo-heterodyne setup, along with a frequency spectrum illustrating the appearance of sidebands at frequencies shifted by  $\pm m\nu_r$  for each cantilever harmonic  $n\nu_d$ . Also shown is the *s*-SNOM amplitude and phase from pseudo-heterodyne detection on a Au/Si calibration grid.

From Equation (57), measurement of an even sideband ( $m = \text{even}$ ) provides the in phase real part of the near-field signal, while for  $m = \text{odd}$ , the sideband measures the out-of-phase imaginary part of the Fourier component. Through the measurement of two sidebands (denoted  $j$  and  $l$ ) the magnitude of the near-field component can be found via the relation

$$\mathcal{E}_{\text{nf},n} \propto \frac{\exp[i\phi_{\text{ref}}]}{2C_{\text{det}}E_{\text{ref}}} \left( \frac{U_{\text{det},n,j}}{J_j[\gamma]} + i \frac{U_{\text{det},n,l}}{J_l[\gamma]} \right). \tag{58}$$

For the special case in which sidebands of  $j = 1$  and  $l = 2$  are chosen with a modulation phase amplitude of  $\gamma_{12} = 2.63$ ,  $J_1[\gamma] = J_2[\gamma]$  and the expression for the magnitude of the near-field can

be further simplified to

$$\mathcal{E}_{\text{nf},n} \propto \frac{\exp[i\phi_{\text{ref}}]}{2C_{\text{det}}E_{\text{ref}}J_1[\gamma_{12}]}(U_{\text{det},n,2} + iU_{\text{det},n,1}). \quad (59)$$

Experimentally, this phase modulation amplitude corresponds to a modulation depth for the mirror in the reference arm of  $\Delta l = \gamma_{12}\lambda/(2 \cdot 2\pi) \simeq 0.21\lambda$ . Finally, the phase difference between the near-field and reference field can be derived from the arctangent of the two detected signal components,

$$\Delta\Phi = \arctan\left[\frac{U_{\text{det},n,1}}{U_{\text{det},n,2}}\right]. \quad (60)$$

### 5.2.5. Near-field spectral behavior

While the coupled dipole model qualitatively describes the *s*-SNOM signal generation, it fails to adequately predict the details of the spectral characteristics. Several more refined models have been developed which consider a more realistic model geometry to describe the tip [222,266–268]. Many of these models, however, require extended numerical simulations in order to reconstruct the optical electric field distribution of the tip. An analytic expression can be obtained by approximating the tip as a spheroid and using a specific distribution of point-charges to model the electric field distribution of the tip [269]. This model well reproduces observed elastically scattered *s*-SNOM spectra in certain cases.

In general, spectroscopic *s*-SNOM measurements are characterized by dispersive lineshapes as a result of the coherent coupling of multiple source terms to the near-field tip-sample interaction. In IR *s*-SNOM, just like any other experimental configuration that involves reflection and diffuse scattering [270], the signal response includes the intrinsic material dielectric function with both resonant absorption and dispersion as well as non-resonant terms [264]. Furthermore, extrinsic tip size and geometry affect the induced coupled tip-sample polarization [269,271]. The result is variations in lineshapes that do not necessarily correlate with the intrinsic vibrational or electronic far-field spectra. In certain cases, and in particular for weakly dispersive, e.g., molecular vibrational resonances, the spectral near-field *s*-SNOM phase directly reflects vibrational energy and intrinsic line width without the need to resort to specific model geometries for the tips [272,273].

The spectral behavior of the *s*-SNOM signal may change as the tip approaches a resonant sample due to coupling affecting the maximum enhancement position. This typically corresponds to a red-shifting of the predicted *s*-SNOM signal [269]. This behavior is displayed for the case of SiC modeled under the coupled dipole model in Figure 20. For SiC, the longitudinal and transverse optical phonon modes result in the formation of a surface phonon-polariton mode which can dramatically increase the magnitude of the *s*-SNOM signal. The observed peak in the *s*-SNOM signal shifts to lower energies as the tip approaches the surface.

### 5.2.6. Microwave near-field impedance microscopy

The previous sections illustrate the principle of elastic *s*-SNOM at optical frequencies. Parallel to the development of optical *s*-SNOM, a complementary set of near-field measurement techniques have emerged to characterize the dielectric properties of surfaces at lower frequencies. Operating in the microwave frequency regime ( $\sim 100$  MHz–100 GHz) these measurements utilize the near-field coupling of a microwave circuit to a sample surface to provide material specific information. Here, the near-field coupling can be expressed in terms of the local impedance of the substrate in the vicinity of the near-field probe, with spatial resolution theoretically limited only by tip apex radius.

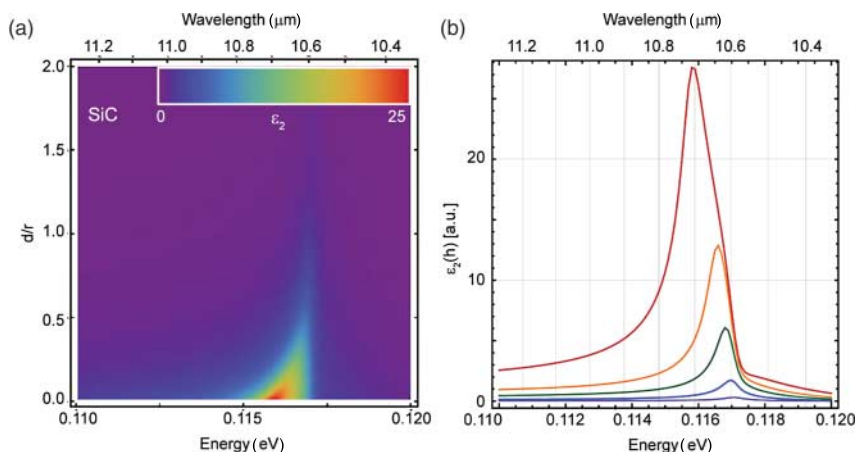


Figure 20. Simulated  $s$ -SNOM signal for the second-harmonic of the dither frequency  $\mathcal{E}_2$  above a SiC surface (a). Line cuts showing the increase and shift of the peak  $s$ -SNOM signal for heights of 0 (red), 0.25 $r$  (orange), 0.5 $r$  (green),  $r$  (blue), and 2 $r$  (purple) with  $r$  representing the radius of curvature of the AFM apex (b).

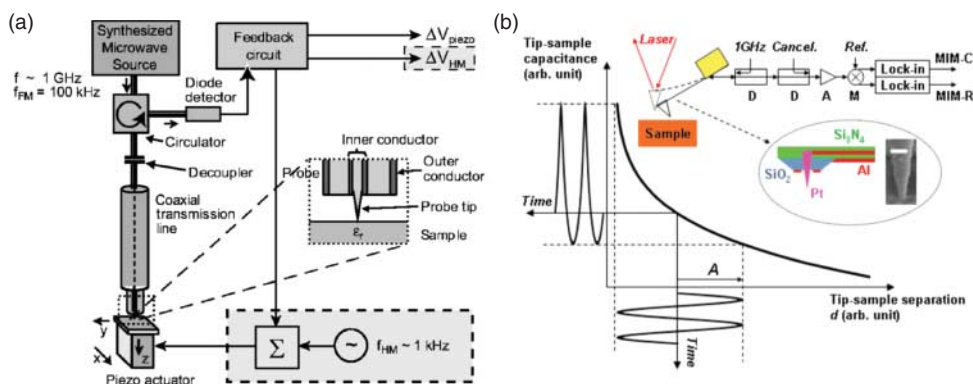


Figure 21. Experimental layouts for two different microwave near-field microscope designs. A near-field probe is held above the surface using height modulation distance control (a) (adapted from A. Tselev *et al.*, Rev. Sci. Instrum. 74 (2003), pp. 3167–3170 [276]). Panel (b) shows a microwave probe which also serves as an AFM tip and which is held in feedback with the surface via tapping mode AFM (adapted with permission from Lai *et al.*, Nano Lett. 9 (2009), pp. 1265–1269 [278]. Copyright 2009 American Chemical Society).

In general, the microwave probes in these techniques are sensitive to the local complex permittivity and conductivity of the sample [274,275]. A variety of operation/detection modes have been developed for microwave microscopy techniques, and the microwave probe can be either resonant or non-resonant. For the case of resonant probes, changes in the resonance frequency and quality factor of the probe induced via near-field coupling to the surface are measured. Non-resonant probes are used to measure surface reflection or transmission [275].

Conventional scanning tunneling, shear-force, and atomic force-based dynamic feedback have been used to position and control the microwave probe near the surface. In addition, for resonant probes, the probe-sample separation can be modulated and the probe resonance frequency shift used as a feedback mechanism.

Two experimental implementations of microwave near-field microscopes are illustrated in Figure 21. Panel (a) displays an apparatus where the microwave probe is an open-ended coaxial

transmission line resonator with capacitive coupling to a feed line [276]. The probe tip extends the center conductor of the coaxial resonator to a sharp point which enhances the electric fields at the sample. Feedback with the surface is achieved via the probe resonance and height modulation of the sample surface [276]. Panel (b) shows a near-field microwave set-up which utilizes dynamic atomic forces to establish feedback with the sample surface. Here, the capacitance established between the tip and surface is a sensitive function of the distance separating the two [277]. The inset of panel (b) illustrates the relationship between the complex tip geometry and the microwave electronics. In this case, information on the dielectric properties of the surface is gathered by measuring the microwave circuit response as the AFM tip periodically moves above the surface [277].

With its sensitivity to the low-frequency dielectric properties, near-field microwave microscopy techniques are well developed and have been implemented to characterize a variety of systems, including superconductive materials [278–281], metal–insulator transition materials [282,283], CMR materials [284,285], FEs [286,287], and systems with electronic inhomogeneities [277]. In contrast to *s*-SNOM, which operates in the infrared to visible spectral region, microwave impedance microscopy is limited in its ability to probe specific electronic or structural resonances due to its low microwave frequency. However, with its compact integrated design with driving field delivered and detection via waveguides to the scanning probe tip, it can more easily be applied at cryogenic temperatures and high magnetic fields which are more challenging for *s*-SNOM with free space light delivery. The variety of correlated materials to which near-field microwave microscopy has been applied also demonstrates the potential of *s*-SNOM, which is not only sensitive to the DC conductivity, but can provide additional information about structure, symmetry, electronic, and vibrational resonances, and coupling of parameters.

### 5.2.7. Tip-enhanced Raman scattering

Plasmon-enhanced spectroscopies benefit from the local field enhancement at the tip apex, ideally amplified via a plasmon resonance. The plasmon resonance increases the capture cross section of the tip acting as an optical antenna [215]. The resulting larger local field enhancement, associated with a decrease in field strength in the overall focus area (for reasons of energy conservation) would increase the contrast between the tip-localized near-field signal and the far-field background from the diffraction limited focus area. With signal levels generally insufficient to employ demodulation schemes, tip-enhanced techniques ideally require an intrinsically large near- to far-field contrast, provided by the large field enhancement. This leads to new experimental considerations and possibilities, though the fundamental imaging mechanism is identical to elastic *s*-SNOM.

*Development of TERS.* The development of TERS can be thought of as a derivative of SERS [288–291]. In SERS field enhancement is obtained via the typically coupled plasmon resonances of rough or specifically patterned noble metal substrates or colloidal particles [292,293]. Very high Raman enhancement factors of up to  $\sim 10^{14}$  have been reported ( $F \simeq 10^3\text{--}10^4$ , see Equation (40)) [294,295]. More modest values of up to  $\sim 10^{10}$  reported recently [296,297] are nevertheless sufficient for single-molecule sensitivity [296]. However, the distribution of localized “hot spots” is random or at least difficult to control [298].<sup>3</sup> Therefore SERS lacks the capability for spatially resolved nanoscale imaging and spectroscopy. By contrast, the inverse geometry, i.e. a localized “hot spot” of field enhancement, for example, at the end of a scanning probe tip, would allow for spatially resolved imaging.

The development of TERS originated from this desire for a controllable SERS probe and evolved from early predictions of large-field enhancement at the apex of noble metal tips [11,221,226] and subsequent application to nonlinear processes [299]. Initial demonstrations of TERS were performed on molecular systems under resonant Raman excitations for maximum signal levels [233,234]. Ultrahigh spatial resolution with TERS was demonstrated in the study of

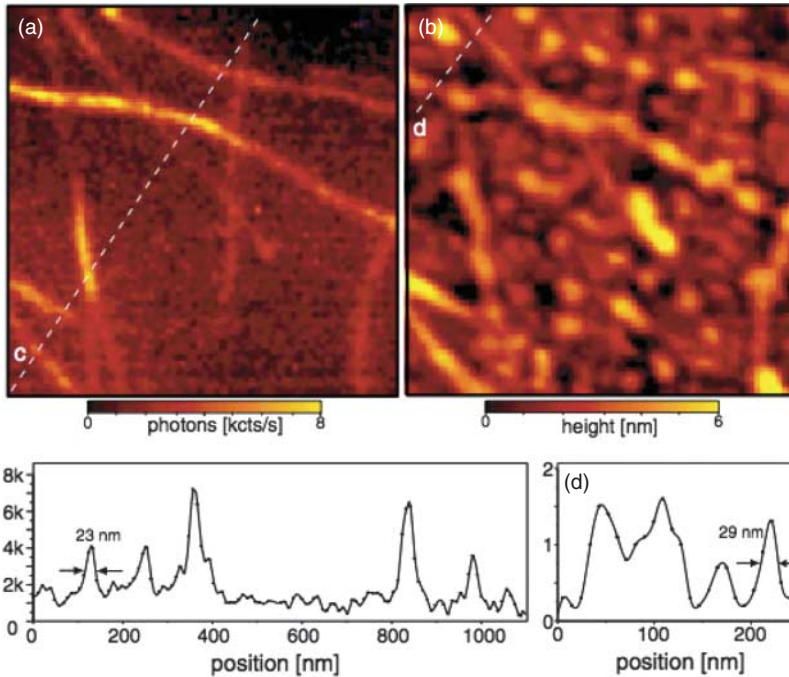


Figure 22. Single-wall carbon nanotube  $G'$ -band TERS image (a) and corresponding topography (b). Cross-section taken along the dashed lines in the optical image (c) and topography (d). Adapted from A. Hartschuh *et al.* Phys. Rev. Lett. 90 (2003), p. 095503 [15]. Copyright 2003 by the American Physical Society.

carbon nanotubes (CNTs) [15]. The initial focus on molecular systems and carbon nanostructures can be attributed to the large Raman scattering cross-sections of dye molecules and the CNT phonon modes excited at resonant frequencies. Shown in Figure 22(a) is the integrated TERS intensity of the  $G'$  nanotube mode and (b), the topography, with corresponding cross-sections along the dashed lines in (c) and (d), respectively. Improvements in signal detection, general instrumentation, and plasmonic tip fabrication allowed for single molecule TERS for the case of resonant dyes [237,253,300,301]. With the development of more complex tip geometries, high enhancement even with dielectric substrates and almost background-free Raman spectral imaging have been demonstrated [247].

With the ability to probe the chemical fingerprint region with ultrahigh spatial resolution, the extension of TERS to biological systems has been explored [235,241,302]. TERS has successfully been used to study the complex PS in polymer films [303,304]. The nonlinear extension of TERS to coherent anti-Stokes Raman scattering has also been demonstrated [305].

*Field enhancement in TERS.* For a surface with uniform molecular coverage the Raman enhancement factor  $M$  is determined from the measured near- and far-field optical intensities  $I_{NF}$  and  $I_{FF}$ , respectively, the size of the far-field focus  $A_{FF}$ , and the spatial extent of the tip-enhanced region  $A_{NF}$

$$M = \frac{I_{NF} A_{FF}}{I_{FF} A_{NF}}. \quad (61)$$

While  $A_{FF}$  can readily be calculated based on the illuminating wavelength and NA of the illuminating optics,  $A_{NF}$  is determined by the tip apex size on the order of  $\sim 10$  nm. More generally, for

the volume-based response in phonon TERS  $A_{\text{NF}}$  and  $A_{\text{FF}}$  in Eq. (61) are replaced by the probed volume.

For the case of molecular systems on metallic substrates, enhancement values of  $M \sim 10^7$ – $10^9$  have been measured [237,253,300,301], consistent with the large values expected for the strong near-field tip-sample coupling between a metallic tip and substrate as discussed above. As in SERS, where large enhancement factors arise for coupled metallic structures,  $M$  values of that magnitude are generally sufficient for single molecule sensitivity. For the case of crystalline or biological samples, where the use of metal substrates for additional field enhancement is difficult or impossible, TERS enhancement values of up to  $M \sim 10^4$ – $10^5$  are found for free-standing tips (see, e.g., [225] and references therein for an excellent discussion regarding experimentally achieved enhancement values). This is in good agreement with theoretical predictions of  $F \simeq 10$ – $50$  [218,219,221,222,226,227] for apex radii of 10–20 nm, with theoretical overestimates resulting primarily from numerical artifacts [220] and imperfections in tip fabrication techniques.

*TERS of crystalline solids: Phonon selection rules.* While the development of TERS for the study of molecular systems, driven by the need for an analytical technique with nanoscale chemical sensitivity, has benefitted from the additional large field enhancement from metallic substrates, studies of crystalline solids have been limited. As discussed above, the lattice  $k$ -vector dependence of Raman scattering and related tensor-based selection rules would provide additional degrees of freedom to determine nano-crystalline order and symmetry. What needs to be considered, however, is the anisotropy of the field enhancement for  $s$ - and  $p$ -polarized light, with in general  $F_p > F_s$ , which can be expressed via a field enhancement tensor  $\overleftrightarrow{F}$ . It follows from Equation (40) that the effective polarization for the  $N$ th phonon mode is then given by

$$\mathbf{p}_{\text{eff},N} = \overleftrightarrow{F}[\omega_{\text{out}}] \overleftrightarrow{R}_N \overleftrightarrow{F}'[\omega_{\text{in}}] \mathbf{E}_0, \quad (62)$$

with the exact form of the tensor depending on the coordinate system used, as discussed below. By the appropriate selection of the elements of  $\overleftrightarrow{F}$  and  $\mathbf{E}_0$  it then becomes possible to selectively probe-specific Raman tensor components and increase the degrees of freedom compared to conventional Raman scattering.

One of the established applications of Raman scattering is in measuring the built-in strain of semiconductor devices via induced phonon frequency shifts [165,167], leading to a strong desire for corresponding experiments with nanoscale spatial resolution. With its large Raman cross-section, much of the crystalline TERS research has focused on silicon. However, a significant far-field background originates from the bulk, which frequently obscures the near-field response.

We illustrate this problem by considering a Si TERS experiment using illumination at  $\lambda = 633$  nm based on the discussion in Ref. [173]. Because of the opacity of Si, side-illumination optics are required, where an objective with  $\text{NA} = 0.35$  generates an elliptical far-field focus with an area  $A = 7.6 \mu\text{m}^2$  with an optical skin depth of  $\sim 5 \mu\text{m}$ . Estimating a near-field probe volume of  $10^3 \text{nm}^3$  and a realistic TERS enhancement factor  $M = 10^4$ , from Equation (61), we expect a near- to far-field contrast  $I_{\text{NF}}/I_{\text{FF}} = 2.6 \times 10^{-4}$ . While this provides a lower estimate and experimentally measured values are generally larger, this poor contrast nevertheless presents a significant concern for TERS studies of bulk crystalline materials in general.

The depolarization of the tip-scattered light by the tip provides a means to overcome this limitation. A nanoscopic scatterer such as a tip will modify the polarization state of  $\sim 10\%$  of the tip-scattered TERS signal [306]. For conditions where the TERS selection rules predict the detection of  $p$ -polarized light only, a small portion of near-field signal will then be detected in the  $s$ -polarized configuration as well. By orienting the crystallographic directions of the sample and incident and detected polarization such that far-field Raman scattering is forbidden, the observation

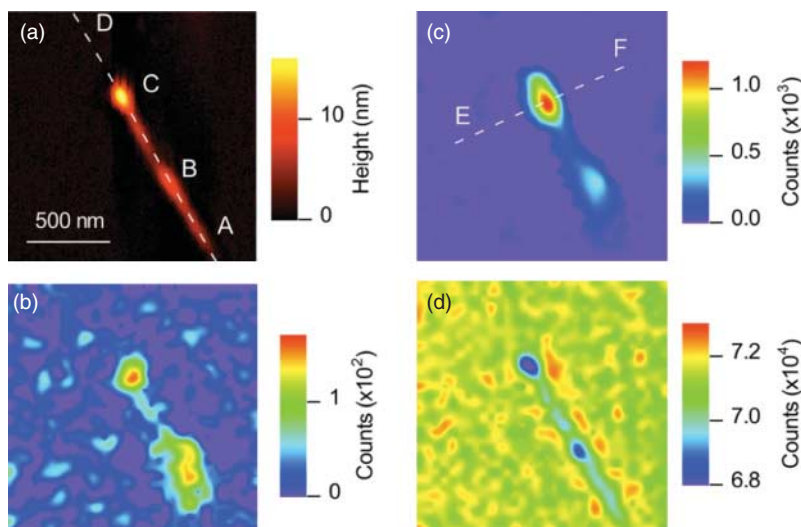


Figure 23. Topography of Ge nanowire (a) and corresponding TERS images at (b)  $283\text{ cm}^{-1}$ , (c)  $298\text{ cm}^{-1}$ , and (d)  $510\text{--}530\text{ cm}^{-1}$  representing phonon modes characteristic for amorphous Ge, crystalline Ge, and the Si substrate, respectively. Point C has a Raman signal approximately four times larger than the rest of the nanowire, due to coupling between the Au nanoparticle on the tip and one attached at the top of the nanowire. Point B is a defect region on the nanowire, with a larger amorphous signal than the rest of the nanorod. Adapted from Y. Ogawa *et al.*, *Appl. Phys. Lett.* 99 (2011), p. 053112 [318]. Copyright 2011 American Institute of Physics.

of near-field modes with enhanced contrast, at the expense of an overall reduced signal level, is enabled [307–311].

The sample strain manifests itself in Raman spectra via the redshift of the main Raman mode at  $520\text{ cm}^{-1}$  [167]. Thus, via the systematic study of this depolarization effect TERS imaging of strained Si became possible [307,310,312,313]. Although practical applications have remained difficult due to an overall low TERS signal levels, the application to the characterization of nanoscale semiconductor devices seems promising.

TERS studies of isolated nanostructures benefit from the reduced bulk volume exposed to far-field excitation, thus exhibiting an improved near- to far-field contrast. To date, a number of TERS studies have been carried out on crystalline nanostructures, including studies on the strain distribution in Ge/Si quantum dots and their effect on the surrounding Si substrate [245], strained Si/Ge structures [314], ferroelectric nanocrystals [315,316], and inhomogeneity in the crystal phase of CdSe nanowires [317] Figure 23(a) shows the topography of a Ge nanowire [318]. Panels (b)–(d) show the TERS intensities at 283, 298, and  $510\text{--}530\text{ cm}^{-1}$ , respectively. As expected, the Si mode from the substrate, at  $510\text{--}530\text{ cm}^{-1}$ , is diminished on the rod, while the Ge modes at 298 and  $283\text{ cm}^{-1}$  are enhanced, with spatial variation in the crystalline and amorphous Raman modes due to defects.

While the depolarization during the tip-scattering process is observed, the effect is weak [308] and can be neglected if the dominant tip-scattered polarization ( $p$ -out) is favored by the selection rules. It is expected that the near-field wavevector is largely unmodified from the far-field excitation. This is evidenced by the lack of asymmetric broadening of the Raman modes to the low-frequency side, indicating that the far-field Raman selection rules are retained in the near-field [319]. By considering the additional tip selection rules, it therefore becomes possible to extend the full capability of the Raman selection rules to the nanoscale. This allows for the isolation and study

of Raman-active phonon modes and their spatial variation. Conversely, the modes observed under a given experimental configuration provide insight into the crystallographic orientation, and by extension, the formation of structural domains.

### 5.2.8. Nonlinear *s*-SNOM

Nonlinear techniques frequently provide new and complementary information compared to linear and inelastic scattering. In combination with *s*-SNOM, they represent a versatile approach for spectroscopic imaging with ultrahigh spatial resolution and sensitivity to symmetry and phase. In particular, the tip locally breaks symmetry and provides excitation with a broad range of *k*-vectors, overcoming the standard far-field momentum considerations and allowing access to nanoscale symmetry behavior [215]. This allows the distinction of, for example, FE and FM domains of arbitrary orientation, and the imaging of coexisting domains on the nanometer scale in multiferroics. Furthermore, with the broad wavelength range and a variety of nonlinear processes discussed in Section 3.2.3, it is possible to study spatially varying properties with frequency-selective excitations.

As discussed earlier, the nonlinear optical response of a material reflects sample symmetries and the coupling of elementary electronic or lattice excitations. This can provide information about local crystallographic structure and magnetic ordering, as well as surface specific states and processes for the case of second-order nonlinear optical interactions in particular. While using nonlinear techniques for *s*-SNOM, however, it is important to additionally consider the effect of the tip, which as a nanoscale object exhibits novel nonlinear properties in itself. The lack of translation invariance of nanoparticles means that the standard crystallographic symmetry description of the nonlinear response does not simply apply. In particular, size and shape will influence the nonlinear response [320,321]. The constraints imposed by momentum conservation are lifted, resulting in new and additional selection rules [322,323]. The nonlinear response is therefore a combination of intrinsic material symmetry, geometric considerations including the surface and bulk response, and choice of incident and output *k*-vector.

In this discussion, we will focus on SHG as the lowest-order nonlinear response, but the symmetry considerations are generalizable to the other second-order and higher-order nonlinear processes. For the case of a spherical nanoparticle of a centrosymmetric material, no SHG is generated in the bulk within the dipole approximation due to the lack of symmetry-breaking [322, 324,325]. In the surface response, the linear dipole mode aligned in the direction of the pump polarization will also not produce SHG emission as the surface polarization densities at both polar regions of the sphere are out of phase and therefore destructively interfere. Instead, a dipolar mode arises due to retardation in the phase across the particle diameter, essentially a nonlocal excitation effect [326]. This SHG dipole is oriented along the polarization direction of the pump beam, so that no SHG will radiate in the exact forward and backward directions. Higher-order multipolar contributions to the nonlinear polarization can also occur for large particles [327,328].

*s*-SNOM tips can be considered within this context, as partially asymmetric ( $\infty$ mm) nanostructures, with broken mirror symmetry along the tip axis, i.e. a hemispherical structure. Even with a centrosymmetric material, this geometric symmetry-breaking leads to fully local dipole-allowed SHG contributions for polarization along the tip axis [215]:

$$P^{(2)}[2\omega] = \epsilon_0 \overleftrightarrow{\chi}_s^{(2)}[\omega, 2\omega] F[2\omega] F^2[\omega] E^2[\omega]. \quad (63)$$

Here,  $\chi_s^{(2)}$  denotes the nonlinear susceptibility tensor with the components  $\chi_{s,\perp\perp\perp}^{(2)}$ ,  $\chi_{s,\perp\parallel\parallel}^{(2)}$ , and  $\chi_{s,\parallel\perp\parallel}^{(2)}$ , where  $\perp$  and  $\parallel$  refer to the local spatial components perpendicular and parallel to the

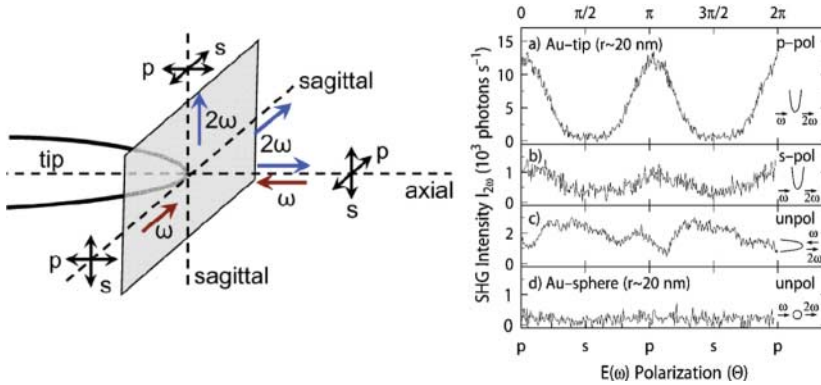


Figure 24. Experimental geometry for probing the SH response of a nanoscopic tip (left).  $k[\omega]$  is directed along the axial or sagittal directions, with  $p$ -polarization defined as along the tip axis for sagittal illumination and detection. Right: SHG polarization dependence for various input and output configurations: sagittal illumination of the  $\infty$  mm tip,  $p_{out}$  (a) and  $s_{out}$  (b), where the signal is dominated by the local dipole-allowed SH; axial illumination of a tip (c), where SHG is forbidden; and forbidden SH illumination in the forward direction in a gold nanosphere (d). Adapted from C.C. Neacsu *et al.*, Phys. Rev. B 71 (2005), Article no. 201402 [323]. Copyright 2005 by the American Physical Society.

surface.  $F(\omega)$  and  $F(2\omega)$  are the local field correction factors for the pump fundamental  $\omega$  light and generated SH  $2\omega$  light, as discussed above.

The symmetry breaking leads to different polarization selection rules for SHG in nanoscopic metal tips compared to surfaces or spherical particles. In addition to the dipole-allowed surface SHG, the bulk nonlocal process discussed for the case of spherical nanoparticles can also generate SHG, but in the case of tips these different mechanisms for SHG are separable. For sagittal pump illumination and collinear  $p$ - and  $s$ -polarized detection, SHG is dominated by the apex-localized, local dipole allowed  $p_{in} - p_{out}$  contribution, from the  $\chi_{s,\perp\perp\perp}^{(2)}$  term (see Figure 24). For axial excitation and collinear axial detection SHG is forbidden by symmetry, analogous to the case of small spherical metal nanoparticles discussed above (Figure 24(c) and (d)).

Just as in the case of elastic and Raman scattering, SHG emission is enhanced when the fundamental excitation or SHG emission frequencies correspond to a resonance in the local optical field factor. This is the case for surface-enhanced SHG [213,329,330] with rough Au surfaces. However, the surface and bulk contributions to the SHG signal are often difficult to separate without, for example, surface modifications [129,130]. The efficiency of nonlinear processes in single and coupled Au nanoparticles on a tip has been investigated and optimized [246,331–333] and the magnitude and symmetry response is well understood in terms of nonlinear Mie and Rayleigh scattering, with an effective surface susceptibility  $\overleftrightarrow{\chi}_s$  [334]. Additionally, there is considerable interest in developing nanoprobes with enhanced nonlinear properties, by using nanowires or nanocrystals with high nonlinear susceptibilities [335–337], but this is challenging due to the difficulty in optimizing for the wavelengths involved in various wavemixing properties.

In the context of SHG  $s$ -SNOM, the main source of SHG can be from the apex surface region of the tip where the local polarization density  $P[2\omega]$  is induced, or the sample just beneath the tip, depending on the relative nonlinearity of tip and sample,  $\chi_{tip}^{(2)}$  and  $\chi_{sample}^{(2)}$  [338]. The near-field SHG response has a complex dependence on incident and output polarization and tip and sample symmetry and material properties, so that crystal orientation and incident  $k$ -vectors must carefully be chosen to probe parameters of interest. With the tip predominantly enhancing the electric field along its axis, the SHG response will be dominated by susceptibility components selected by

that field, according to the tensor equation (23). In spite of the promise of this technique for obtaining nanoscale symmetry and structural information, thus far there has been relatively little SHG *s*-SNOM imaging of materials [14,339,340].

As a coherent wavemixing process, SHG also provides access to the phase of an excitation, enabling full amplitude and phase characterization of, e.g. localized plasmon dynamics. This characterization is important for *s*-SNOM tips and other optical antenna geometries, since a plasmonic resonance can be beneficial for field enhancement and therefore signal levels, but may also lead to a long dephasing time, limiting temporal resolution. These plasmon dynamics are generally very short, but full plasmon response reconstruction can be performed through, for example, frequency-resolved optical gating (FROG) [341]. For an Au *s*-SNOM tip, FROG characterization yielded a dephasing time of  $\sim 20$  fs for wavelengths close to the plasmon resonance [342]. When the incident illumination was not resonant with the tip plasmon, the tip response was essentially instantaneous. Similar experiments have probed plasmon dynamics in other Au nanostructures [343–346].

While we have emphasized the use of SHG for characterization, *s*-SNOM is compatible with almost any implementation of coherent and incoherent pump probe spectroscopy, including THz and mid-IR spectroscopy, nonlinear second- or third-order wavemixing, coherent phonon, or even multi-dimensional spectroscopies.

### 5.2.9. *Low-temperature and magnetic field s*-SNOM

One of the unique features of optical spectroscopy is its applicability at essentially arbitrary temperature, pressure, and in the presence of large magnetic or electric fields. For correlated materials, temperature, electric and magnetic field poling, and strain, in particular, are important control parameters, due to the sensitivity of phase and coupling to external perturbation. The extension of near-field microscopy and *s*-SNOM to operate under vacuum and at variable temperature and magnetic field conditions is therefore highly desirable. However, relatively few vacuum and low temperature-compatible near-field optical microscopes have been developed. The need for vacuum- and cryo-compatible materials, vibration control, space constraints in light beam delivery and signal detection, and optical alignment considerations lead to stringent design requirements.

Both fiber-based NSOM and near-field microwave impedance microscopy are readily compatible with low-temperature measurements [283,347–353]. Cooling is achieved using bath cryostats where all components are cooled [348], or flow cryostats with only sample cooling [347]. These microscopes have been used to investigate energy transfer in molecular [354] and quantum dot systems [355,356]. However, the NSOM geometry limits the optical techniques and wavelengths that can be used as well as the achievable throughput. In spite of these challenges, low temperature NSOM ultrafast probing and control of exciton dynamics in quantum dots has been demonstrated, enabled through careful dispersion compensation of the light propagating through the fiber [357].

Designs based on conventional cantilever-based AFMs are less common, due to the difficulty of incorporating optical feedback within a vacuum chamber [358–361]. These designs rely on piezomechanical feedback of the cantilever [361] or fiber feedthroughs [360,362] for maintaining distance control. For these apertureless instruments, beam delivery, alignment, and focusing onto the tip inside the chamber becomes critical. Cassegrain objectives and parabolic mirrors have both been employed as focusing elements, with the advantage of being broad wavelength and vacuum compatible. A reflective sample geometry enables the study of opaque samples, but tends to reduce the numerical aperture. UHV TERS experiments have also been performed [260,363], where a high-NA  $\simeq 1$  on-axis parabolic mirror with efficient excitation of the tip using radially polarized incident light allowed single molecule sensitivity [253].

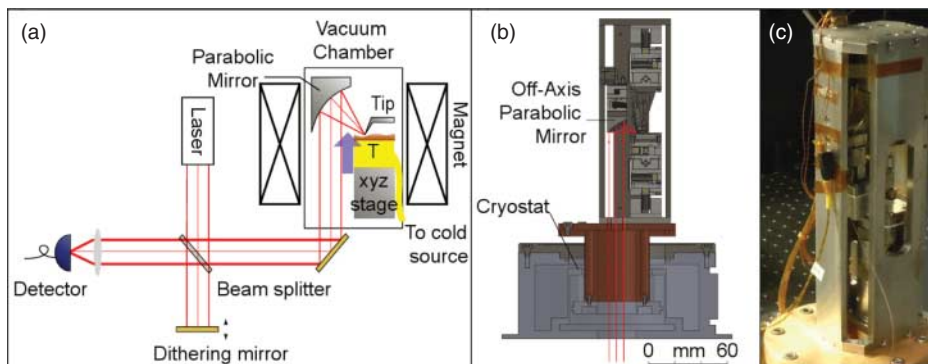


Figure 25. Cryogenic *s*-SNOM, based on an Attocube AFM with optics for tip illumination and scattered light collection. Schematic of the *s*-SNOM setup (a). The temperature control and sensor, in yellow, are immediately beneath the sample for precise temperature control. The blue arrow in the center of the vacuum chamber represents the direction of the magnetic field. Cross-sectional view of AFM and focusing (b). The AFM consists of two slip–stick motion controllers, so that the sample and AFM tip move separately. The off-axis parabolic mirror is mounted on a 2-axis goniometer to allow for independent mirror and AFM alignment. All components are held by titanium housing mounted on a flow cryostat (Janis ST500), with axial bottom illumination and detection. The dimensions are chosen such that the insertion into a high-field (6.5T) superconducting magnet is possible. Photo of *s*-SNOM inside the cryostat (c).

Recently, a new *s*-SNOM instrument operating down to 20 K, fully magnetic field compatible, and with optics covering a broad spectral range from mid-IR to visible and low dispersion has been developed for the investigation of correlated matter [362]. Figure 25 shows the details of the instrument. It is based on a modified low-temperature AFM (Attocube Systems AG), mounted on a flow cryostat. Illumination with a parabolic mirror ( $NA = 0.45$ ,  $f = 11.25$  mm) allows for the use of broad-band and ultrafast laser sources. The slender design and illumination paths allows for insertion into a high-field superconducting magnet with a bore diameter of 75 mm.

## 6. Applications of *s*-SNOM for the study of nano-scale phenomena in complex matter

Having provided a background on the fundamentals and experimental implementation of different optical spectroscopies with *s*-SNOM, in the following sections, we will discuss specific applications for the investigation of different materials systems.

### 6.1. Phase competition in metal–insulator transitions

In several transition metal oxides, the interplay between orbital, spin, charge, and lattice degrees of freedom results in dramatic changes in the conductivity as a function of, e.g., temperature or applied magnetic field. The underlying processes of these metal–insulator transitions (MIT) are often still poorly understood. From the study of the fundamental electron–electron and electron–lattice interactions close to the transitions, a better picture of the details of the electronic structure of these materials in general may be established. As discussed in Section 2.4, one of the primary challenges in understanding MIT materials is that the participating phases are often degenerate and phase separation may occur associated with the transition. Characterizing the evolution of texture and phase fraction of the participating phases through the MIT may thus yield important clues on the fundamental interactions.

In the following sections, we will discuss the implementation of near-field techniques in characterizing the MIT in several correlated electron materials. In particular, elastic *s*-SNOM measurements in the infrared can probe the emergence of a Drude response reflecting the metallic phase. We will first discuss in detail the *s*-SNOM characterization of the metal–insulator transition in VO<sub>2</sub>, one of the first known metal–insulator transition systems. Following the development of elastic IR *s*-SNOM, VO<sub>2</sub> provided an ideal model system to study the MIT in correlated electron systems on the nano-scale due to the easily accessible transition temperature at 340 K.

### 6.1.1. Metal–insulator transition in vanadium oxide

The vanadium oxides are among the most famous of materials which undergo a metal–insulator transition [50,364,365]. VO, V<sub>2</sub>O<sub>3</sub>, and VO<sub>2</sub>, with cubic, trigonal, and monoclinic crystal structures in the insulating phase, exhibit metal–insulator transitions with orders of magnitude changes in electrical conductivity at 114, 153, and 340 K, respectively [364]. All of these oxides exhibit unique phase behavior as a function of temperature, pressure, and doping [50]. The complexities of their phase transitions arise from the interplay of strong electron–electron interactions and electron–lattice effects associated with crystallographic or unit cell volume changes [366,367] at the phase transitions [365,368].

In particular, in VO<sub>2</sub> it is intensely debated whether the MIT is a Mott- or Peierls-driven process, with signatures of both appearing in the transition [368–375]. Despite its simple stoichiometry, VO<sub>2</sub> exhibits a complex phase behavior with a metallic rutile (R) structure [376], and multiple insulating phases, two monoclinic (M1 and M2), and triclinic (T) phases [377], all within a narrow temperature and strain region close to the MIT. As a result, the total free energy of the system can often be minimized through changes in structure and the formation of domains due to the interplay of short-range electronic forces and long-range stress–strain interactions. The development of a fundamental description of the driving mechanism underlying the MIT is therefore complicated by the changes in the crystal lattice structure that accompany the changes in electronic properties at the transition temperature. Even after intensive study over 50 years on bulk and thin film samples, the combination of domain structure, strain, and the subtlety of correlation effects in VO<sub>2</sub> has left a confusing picture of the underlying physics and has frustrated technological applications based upon its unique electronic properties [368,369,372,378,379].

*Infrared s-SNOM characterization of VO<sub>2</sub> thin films.* Recent measurements of the MIT in VO<sub>2</sub> have demonstrated the capability of *s*-SNOM to map spatial heterogeneities in phase on the nano-scale. As the IR dielectric properties of VO<sub>2</sub> exhibit a large change during the MIT [380], IR elastic *s*-SNOM represents a sensitive technique in imaging nano-scale phase changes. Figure 26(a) shows the change in conductivity of VO<sub>2</sub> through the MIT, derived from ellipsometry measurements, with a large change in conductivity between the insulating and metallic phases at  $\sim 10\ \mu\text{m}$  due to the Drude response. The gradual spectral change observed is a manifestation of the inhomogeneous distribution of metallic and insulating crystallites within the VO<sub>2</sub> thin film.

The application of mid-IR *s*-SNOM to image the distribution of metallic and insulating phases in VO<sub>2</sub> thin films is shown in Figure 26(b) [373]. At temperatures below the  $T_{\text{MIT}}$ , a homogeneous *s*-SNOM scattering signal was observed, corresponding to an entirely insulating film [373,381] (panel i). As the temperature is increased, metal clusters with *s*-SNOM signal 2–5 times that of the insulating phase were observed to nucleate at specific locations on the film surface (panels ii–iv). With increasing temperature, these metallic “puddles” grow in size, eventually percolating to form a continuous metallic phase (panels v–vi). The observed pattern of metallic puddles was thought to result from the seeded growth from nucleation sites, determined by interface strain, grain boundaries, or defects in the crystal structure. The evolution of the puddles is reproducible

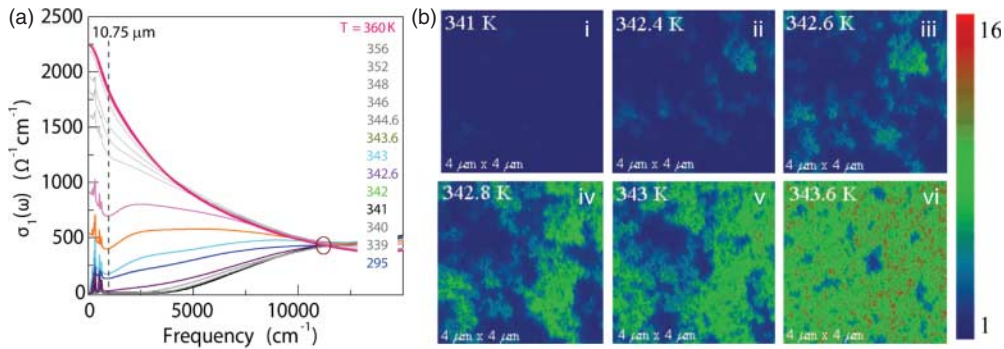


Figure 26. Optical conductivity of a VO<sub>2</sub> thin film at the metal–insulator transition, as derived from spectroscopic ellipsometry (a). Corresponding IR *s*-SNOM images (b) acquired at excitation wavelength of 10.75 μm (930 cm<sup>-1</sup>) as indicated in (a). The observed contrast due to the emerging metallic Drude response reflects the transition of VO<sub>2</sub> crystallites and gradual formation of percolated domains with increasing temperature from the initial insulating to final metallic phase. Contrast: insulating phase (blue), metallic regions (light blue, green, and red colors). Adapted from M.M. Qazilbash *et al.* Phys. Rev. B 74 (2006), p. 205118 [382]. Copyright 2006 by the American Physical Society.

at a particular temperature [381]. At  $T = 360$  K, the MIT was considered to be complete with the final disappearance of the last remaining insulating islands [373].

*Crystal structure and strain interactions in VO<sub>2</sub>.* The interest in thin films of VO<sub>2</sub>, as studied in the above work, is due to the degradation typically experienced by macroscopic bulk crystals from the large change in lattice structure during the MIT. However, the polycrystalline nature of these films leads to additional inter-crystallite strain interactions between crystallites and thus difficulty in extracting the intrinsic phase behavior. For example, measurements of thin-film systems indicate a percolative phase transition [373,381,383], while investigations on unconstrained single micro-crystals suggest that the MIT upon heating can be discontinuous [104,384–387]. Figure 27 illustrates the broadening of the MIT in the conductivity of a thin film compared to the discontinuous change associated with a single micro-crystal [104,383]. Recently, the development of vapor phase deposition protocols for VO<sub>2</sub> microcrystals has enabled the study of well-controlled, single crystal, structures whose micro-scale size and lack of defects allows them to be cycled through the MIT without degradation [104]. The lack of complicated extrinsic interactions makes these micro-crystals ideal for the study of intrinsic strain, domain, and hysteresis behavior.

Understanding the MIT in VO<sub>2</sub>, whether thin film, bulk, or microcrystal, is complicated by the multiple competing insulating crystal structures discussed above. These different insulating phases are shown in Figure 28(a), as extracted from Raman spectroscopic analysis of individual microcrystals subjected to controlled uniaxial strain [179]. The associated crystal structures for the rutile (R), monoclinic 1 (M1), and monoclinic 2 (M2) phases are shown in 29(b)–(d). For the rutile metallic phase, each of the vanadium atoms in the body-centered tetragonal lattice is surrounded by an oxygen octahedron. The monoclinic M1 insulating phase is defined by a crystal structure with a space group of P2<sub>1</sub>/c (C<sub>2h</sub><sup>5</sup>) [388]. Here, the vanadium sites are shifted from the R crystal structure first through a pairing of vanadium atoms along the  $c_R$  axis and second from a characteristic in-plane displacement of the vanadium atoms which alternates along the  $c_R$  and  $a_R$  axes, forming a “zig-zag” arrangement (Figure 28(c)). The monoclinic M2 insulating phase of VO<sub>2</sub> occurs at temperatures below  $T_{MIT}$  at elevated stress or pressure [377] or through doping of Cr [366] or Al [389]. The primary structural distinction of the M2 phase from that of the M1 phase lies in the formation of two distinct vanadium sub-lattices, with sub-lattice A showing pairing

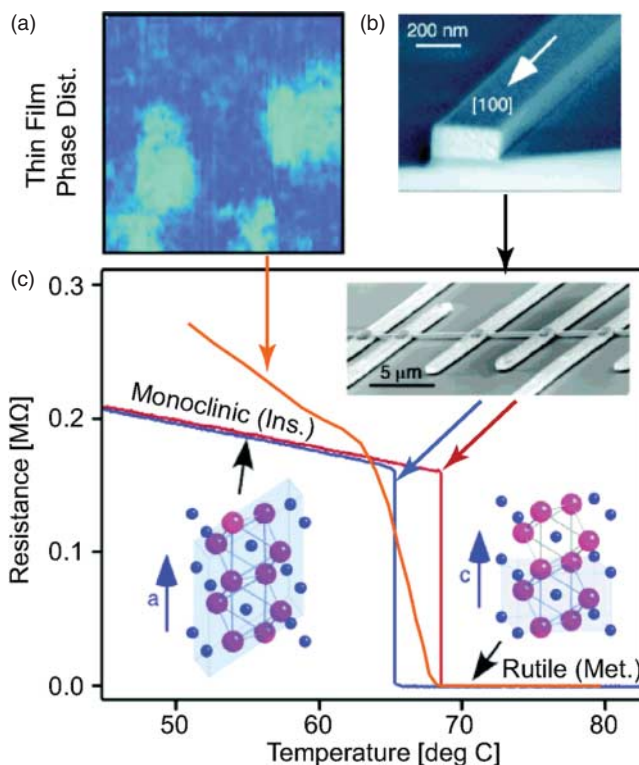


Figure 27. Polycrystalline  $\text{VO}_2$  thin films exhibit inhomogeneities and a percolative MIT transition (a), in contrast to free-standing single  $\text{VO}_2$  micro-crystals (b) with a sudden, discontinuous phase transition. This results in profoundly different DC conductivities (c) associated with the MIT in  $\text{VO}_2$  thin films versus single crystal micro-beams. Adapted from M.M. Qazilbash *et al.*, *Appl. Phys. Lett.* 92 (2008), p. 241906 [383], copyright 2008 American Institute of Physics and J. Wu *et al.*, *Nano Lett.* 6 (2006), pp. 2313–2317 [548], copyright 2006 American Chemical Society.

in the vanadium atoms but no zig-zag displacement (tilt), and sub-lattice B exhibiting tilt but no pairing. The M1 and M2 phases have different unit cell sizes, with  $c_R$  axes longer by  $\sim 1\%$  and  $\sim 1.7\%$  compared to R [366,367,376] respectively, a significant factor in minimizing strain interactions. Lastly, the triclinic phase (T) has been found to be a transitional phase between the M1 and M2 insulating phases, with progressive dimerization of sub-lattice B and a progressive tilting of sub-lattice A in moving from M1 to M2.

*Infrared s-SNOM characterization of  $\text{VO}_2$  micro-crystals.* The combination of IR *s*-SNOM and micro-Raman allowed for the simultaneous study of the phase behavior and associated domain texture during the MIT in  $\text{VO}_2$  micro-crystals [390]. Figure 29 shows AFM topography (d) and simultaneously recorded *s*-SNOM images (a–c) driving a  $\text{VO}_2$  micro-crystal initially in the M1 phase at room-temperature through the MIT. An initial superheating of the M1 phase is followed by the sudden appearance of a first metallic domain (b, f: 341 K). Subsequent domain growth leads via a roughly periodic set of insulating and metallic domains (c, f: 345 K) to the fully metallic state at temperatures of 370–390 K. The appearance of metallic domains is reflected in the Raman spectra by a sharp rise in the luminescence background (Figure 29(g), arrow). Up to  $\sim 350$  K the insulating domains of the regular domain pattern remain in the M1 phase. As the temperature is increased further and the insulating domains begin to shrink in size a

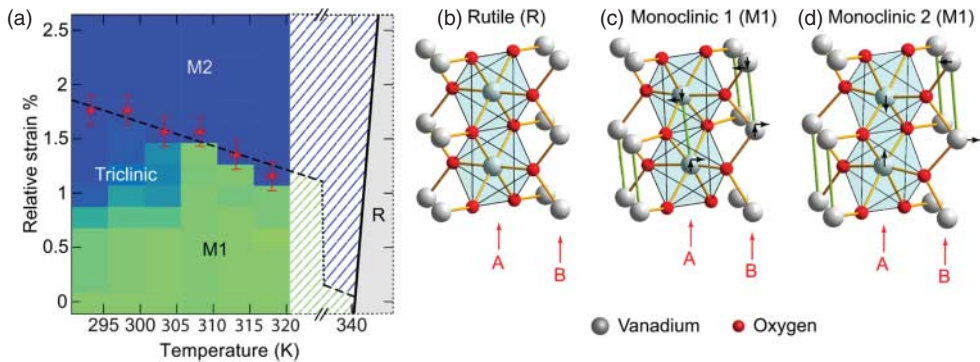


Figure 28. The temperature–stress phase diagram for  $\text{VO}_2$  under uniaxial stress (a), showing the presence of the R, M1, M2, and T phases as measured by Raman spectroscopy. The crystal structures of the primary phases of  $\text{VO}_2$  are displayed above with panels (b)–(d) with (b) representing the metallic/tetragonal-rutile (R) phase, (c) the semiconducting/monoclinic (M1) phase, and (d) the semiconducting/monoclinic (M2) phase. The vanadium atom chain sub-lattices A and B are denoted by the red vertical arrows. The distortion motion from the rutile crystal structure to the M1 and M2 phases is represented by the black arrows for each of the respective insulating phases. Adapted from J.M. Atkin *et al.*, Phys. Rev. B 85 (2011), p. 020101 [179], copyright 2012 by the American Physical Society and A.C. Jones *et al.*, Nano Lett. 10 (2010), p. 1574 [390], copyright 2010 American Chemical Society.

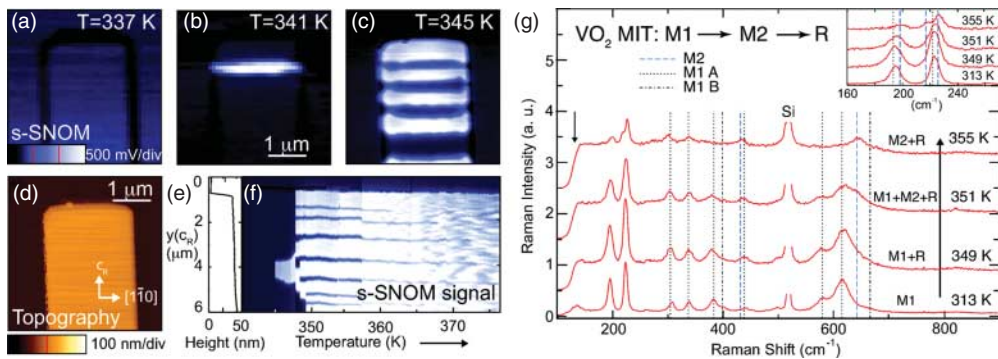


Figure 29. *s*-SNOM images (a–c) with corresponding topography (d) of a  $\text{VO}_2$  crystal ( $h = 35$  nm) initially in the M1 insulating phase (a), and its metallic/insulating domain formation (b, c) as the crystal is heated through the MIT. Corresponding longitudinal line scan tracing the spatial domain formation on a similar  $\text{VO}_2$  crystal with sample heating (e, f). The phases of the insulating domains are identified by Raman measurements (g) finding M1 + M2 + R (351 K) and M2 + R (355 K) intermediate phase coexistence regimes. Adapted from A.C. Jones *et al.*, Nano Lett. 10 (2010), p. 1574 [390]. Copyright 2010 American Chemical Society.

conversion of M1 to M2 is observed, as seen from the appearance of the characteristic M2 Raman modes (g: 351 K). Within a narrow temperature range of  $\sim 5$  K all insulating domains convert to M2 (g: 355 K) without a significant change in the total volume fraction of R. The M1  $\rightarrow$  M2 conversion occurs around 30 K below the temperature where the fully metallic state is reached.

Figure 29(f) shows the associated domain formation and spatial evolution in a repeated *s*-SNOM line-scan along the longitudinal ( $c_R$ ) axis of a crystal with corresponding topography (e) as a function of temperature. The appearance of the first metallic domain in the scan region is followed by a splitting, rearrangement, and subsequent formation of the alternating domain

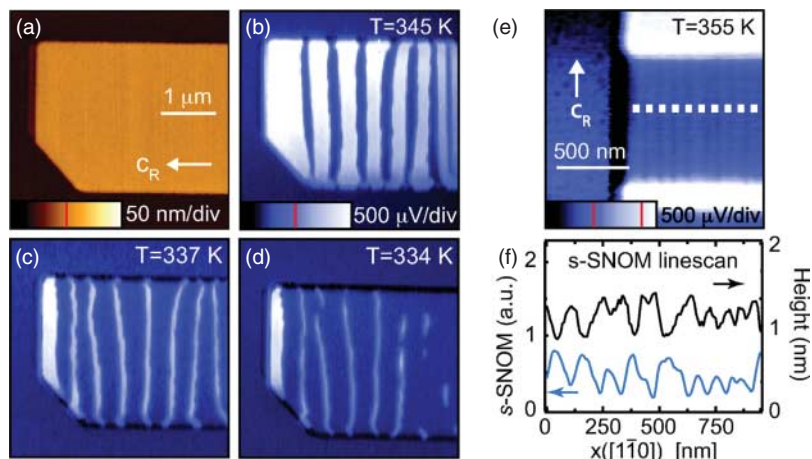


Figure 30. *s*-SNOM images (b–d) with corresponding topography (a) of a VO<sub>2</sub> crystal ( $h = 25$  nm) being cooled through the MIT. Periodic metallic and insulating domains exist slightly above  $T_{MIT}$  (b). As temperature is lowered, the size of the metallic domains decreases (c) resulting in the eventual break up and dissipation of metallic domains (d). Panels (e) and (f) display the fine structure of the insulating phase revealed by *s*-SNOM with periodic twinning of the M2 phase resulting in slight variations of the *s*-SNOM signal. These variations are attributable to the birefringence of the insulating phase. Adapted from A.C. Jones *et al.*, Nano Lett. 10 (2010), p. 1574 [390]. Copyright 2010 American Chemical Society.

pattern. With the high spatial resolution of  $\lesssim 30$  nm provided by *s*-SNOM, it can be seen that thin insulating domains persist up to  $T > 375$  K.

A sequence of *s*-SNOM images taken as a VO<sub>2</sub> micro-crystal was cooled through the metal–insulator transition displays the growth of the insulating domains and the eventual breakup of the metallic stripes into small islands, as shown in Figure 30. These metallic islands can persist within the micro-crystal to temperatures well below the nominal  $T_{MIT}$ , indicating a strain-induced supercooling of the metallic phase. Interestingly, the metallic domain evolution observed upon heating through the MIT from an initial homogeneous M1 phase is reproducible while the domain texture upon cooling is not. Additionally, the observation of slight variations in the *s*-SNOM signal in the insulating domains associated with M2 phase demonstrates the extremely high sensitivity of *s*-SNOM. These variations, illustrated in Figure 30(e) and (f), have been associated with a periodic twinning of the M2 phase [391] and associated birefringence.

Through the combination of IR *s*-SNOM to map the metal–insulator phase fraction with micro-Raman spectroscopy to identify the insulating phases, it was found that two MIT pathways seem to exist, depending on the initial sample strain. Because of the mismatch of the thermal expansion coefficients between VO<sub>2</sub> and the substrate [367], the crystallites are initially stressed predominantly along the  $c_R$  crystallographic direction at room temperature. The formation of alternating metallic and insulating domains reduces the amount of substrate-induced strain [104]. Crystallites under compressive stress existing in the M1 insulating phase were found to transition by a  $M1 \rightarrow M1 + R \rightarrow M1 + M2 + R \rightarrow M2 + R \rightarrow R$  pathway as the temperature increased from room temperature, in order to minimize the strain through the differing lattice constants associated with the insulating phases. Other crystallites under initial tensile stress, identified as beginning in either the T or M2 phase were found to transition by a  $M2 \rightarrow M2 + R \rightarrow R$  pathway [390]. This demonstrates the subtle interplay of strain and temperature in the MIT of VO<sub>2</sub>.

From image analysis of the *s*-SNOM scans, the volume fractions of metallic and insulating phases with temperature were deduced. The phase volume fraction diagrams for VO<sub>2</sub> crystallites

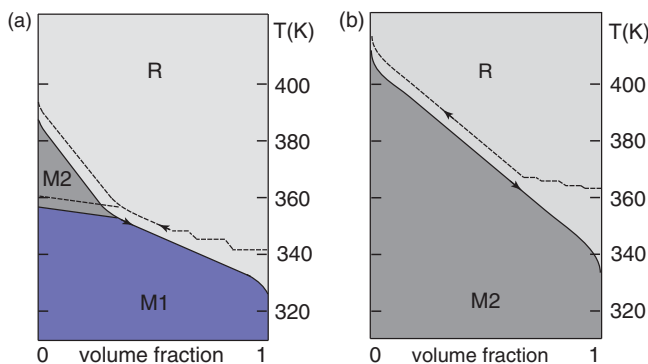


Figure 31. Temperature dependence of crystal volume fraction in the M1, M2, and R phases for a crystallite initially in the M1 phase at room temperature (a). The corresponding diagram for crystals found in the M2 phase at room temperature (b). Results derived from the combination of *s*-SNOM and micro-Raman spectroscopic imaging. Adapted from A.C. Jones *et al.*, *Nano Lett.* 10 (2010), p. 1574 [390]. Copyright 2010 American Chemical Society.

found in the M1 and M2 phase at room temperature are displayed in Figure 31(a) and (b). This result highlights the capability of *s*-SNOM to study domain texture and volume fraction for complex phase behavior in correlated matter.

### 6.1.2. Near-field microwave impedance microscopy of the MIT in CMR manganites

Low-frequency microwave near-field techniques, as introduced above, have been applied for the investigation of electronic phase transitions in the manganite  $\text{Nd}_{1/2}\text{Sr}_{1/2}\text{MnO}_3$ , a model CMR material. Thin films of  $\text{Nd}_{1/2}\text{Sr}_{1/2}\text{MnO}_3$  on  $\text{SrTiO}_3$  have attracted interest for technological applications, and display bulk-like behavior of a PM to FM transition at  $\sim 250$  K and charge/orbital ordering (COO) at  $\sim 160$  K. In addition, in the COO insulating phase at low temperatures a transition into the FM metal phase with high magnetic fields occurs.

As discussed in Section 5.2.6, microwave near-field microscopy is sensitive to low-frequency conductivity and can therefore distinguish the insulating and metallic phases. Figure 32 shows the domain evolution in the MIT in thin films of  $\text{Nd}_{1/2}\text{Sr}_{1/2}\text{MnO}_3$  as a function of applied magnetic field up to 9 T, at cryogenic temperatures [285]. Already at low fields, some FM-metallic domains were resolved (b). As the magnetic field was increased up to 6 or 7 T, additional metallic areas grew from these original nucleation sites, with a preferential alignment along the [001]- and  $[1\bar{1}0]$ -axes of the substrate. At  $\sim 9$  T, a percolating network of FM-metallic domains was formed (d).

This work provided evidence of the phase coexistence associated with the magnetic field-induced metal-insulator transition of  $\text{Nd}_{1/2}\text{Sr}_{1/2}\text{MnO}_3$ , and the important role of strain, as demonstrated by the preferential orientation of the metallic domains. This is in contrast to, e.g.  $\text{La}_{1-x}\text{Ca}_x\text{MnO}_3$ , where domains have no preferred direction, indicating that Coulomb interactions dominate over strain [86,98]. Microwave impedance microscopy is thus a valuable technique for studying phase coexistence in correlated matter, especially since the broad resistivity range displayed in these CMR materials leads to difficulty in extracting spatial information from conventional DC conductivity measurements. However, while the microwave frequencies provide high sensitivity to the Drude response, they are outside the range of electronic or phonon resonant frequencies, limiting the information about the causes of phase coexistence that can be extracted.

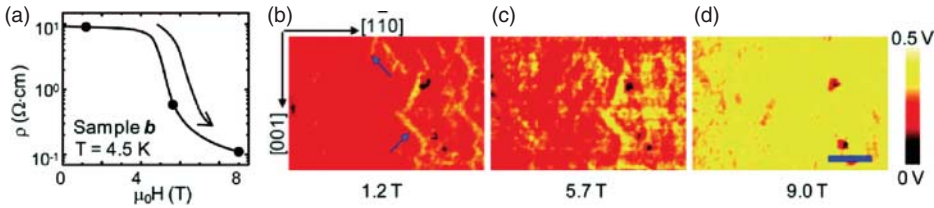


Figure 32. Resistivity of a  $\text{Nd}_{1/2}\text{Sr}_{1/2}\text{MnO}_3$  film at 10 K with increasing magnetic field  $\mu_0 H$  (a). Associated microwave impedance microscopy images mapping the formation of FM metallic domains as a function of increasing external magnetic field (b–d) at 1.2, 5.7, and 9.0 T, respectively. Scale bar, 1  $\mu\text{m}$ . Blue arrows indicate low-field FM-metallic rod-shaped domains. Adapted from K. Lai *et al.*, *Science* 329 (2010), pp. 190–193 [285]. Reprinted with permission from AAAS.

## 6.2. Low-dimensional electronic materials

As discussed previously, the 2D structure of graphene results in unique electronic and optical properties [57]. Near-field techniques have so far been utilized in studying inhomogeneities in graphene structures through microwave impedance microscopy and TERS, and in the IR to probe the plasmonic response of graphene, which supports surface plasmon polariton waves in the mid-IR spectral range, with a high degree of localization and tunability [58].

### 6.2.1. IR *s*-SNOM imaging of graphene

Using infrared *s*-SNOM, the near-field electromagnetic response of a mechanically cleaved graphene monolayer on thin  $\text{SiO}_2$  on a Si substrate has been investigated [59]. With a combination of tunable IR sources ( $\text{CO}_2$  and quantum cascade lasers), the spectral dependence of the optical response of a graphene monolayer from 883–1270  $\text{cm}^{-1}$  was studied. As the surface plasmon resonance frequency is highly dependent on the position of the Fermi level [58], and as graphene on  $\text{SiO}_2$  often exhibits a high carrier density due to uncontrolled doping, far-field Raman spectroscopy was used to locate monolayer graphene structures with similar hole doping, ensuring comparable chemical potentials for the samples studied [59].

A schematic of the IR *s*-SNOM measurement of a sample graphene flake on  $\text{SiO}_2$  is shown in Figure 33(a). Next to the graphene flake, part of the  $\text{SiO}_2$  was etched away to enable signal calibration with respect to the Si substrate. IR *s*-SNOM measurements, obtained using pseudo-heterodyne detection, are shown in Figure 33(b), with the phase relative to that observed over Si. For a range of frequencies *s*-SNOM contrast is observed between graphene,  $\text{SiO}_2$ , and Si. The intrinsic response of the thin  $\text{SiO}_2$  layer shows a peak in the *s*-SNOM signal near 1128  $\text{cm}^{-2}$ , due to the  $\text{SiO}_2$  surface phonon polariton mode [59]. At the doping level of the samples studied, the SPP mode in the graphene monolayer overlaps the surface phonon polariton mode of the thin  $\text{SiO}_2$ , leading to enhancement and blue-shifting in the  $\text{SiO}_2$  surface phonon polariton response. This behavior of the resonant *s*-SNOM signal is displayed in Figure 33(c), with the difference in the detected phase between  $\text{SiO}_2$  and the graphene monolayer in Figure 33(d).

The observed spectral *s*-SNOM response of the graphene monolayer is attributed to enhancement effects from the high density of mobile carriers in the graphene samples [59]. This hypothesis was tested by measuring the *s*-SNOM signal with different gate voltages  $V_g$  applied to the Si substrate. By controlling the carrier density in the graphene, the magnitude of the *s*-SNOM signal could be controlled. The inset of Figure 33(c) shows the results of measuring the *s*-SNOM signal at a frequency where the contribution attributable to the graphene was greatest ( $\omega = 1150 \text{ cm}^{-1}$ )

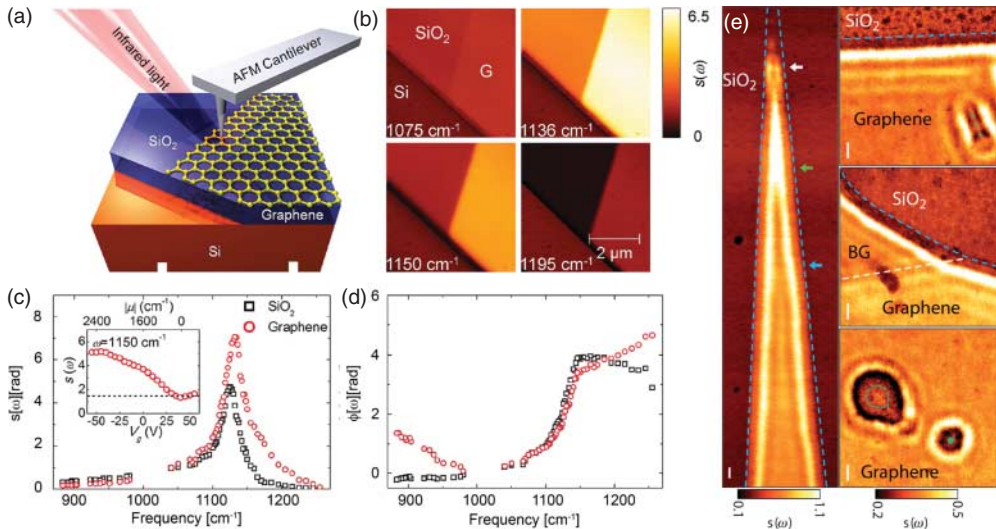


Figure 33. Experimental schematic of the IR  $s$ -SNOM characterization of a graphene (a). Optical contrast in the  $s$ -SNOM signal (denoted above as  $s(\omega)$ ) between Si, SiO<sub>2</sub>, and a graphene monolayer (G) is shown for differing excitation frequencies (b). Spectral dependence of the magnitude (c) and phase (d) of the  $s$ -SNOM signal. (Adapted from Z. Fei *et al.*, Nano Lett. 11 (2011), pp. 4701–4705 [59]). Example of  $s$ -SNOM images ( $\omega = 892 \text{ cm}^{-1}$ ) (e) showing SPP modes in graphene with an interference pattern close to graphene edges (blue dashed lines) and defects (green dashed lines and green dot), characteristic of plasmon interference. Reprinted by permission from Macmillan Publishers Ltd: Z. Fei *et al.*, Nature 287 (2012), pp. 82–85 [392], copyright 2012. Similar results were reported in Ref. [393].

for various magnitudes of  $V_g$ , with a minimum in the contrast at the charge neutrality condition  $V_g = 40 \pm 5 \text{ V}$ .

More recent IR  $s$ -SNOM measurements have directly visualized the surface plasmons in graphene. Shown in Figure 33(e) [392,393] are the characteristic interference fringes that arise from the interference of plasmons induced by the nanoscopic tip and associated large  $k$ -vectors with plasmons reflected off edges and defects in graphene. These results demonstrate the extension of the use of  $s$ -SNOM for the study of SPPs in plasmonic materials and optical antennas to the corresponding excitations in low-dimensional complex matter, where high carrier mobilities allow for SPPs with reduced damping compared to metals and tunability with electric field gating.

*Microwave impedance microscopy imaging of graphene.* Low-frequency near-field microwave impedance microscopy (MIM) has been applied to spatially map the electrical conductivity of single mechanically exfoliated graphene flakes [394]. A modified atomic-force microscope cantilever with Al transmission lines patterned on a Si<sub>3</sub>N<sub>4</sub> base operates in the near-field regime of the surface to record both real (resistive) and imaginary (capacitive) components of the effective tip impedance  $Z_{\text{tip}}$ . Figure 34 displays as an example topography (a) with schematic of the AFM and the associated MIM circuit (b).

While the graphene flakes are difficult to resolve in the topography, MIM images of these homogeneous flakes, shorted to Au contacts, show a strong microwave capacitive response. Figure 34(c) illustrates MIM images recorded over single-layer graphene flakes with Au contacts. MIM measurements were also used to characterize the quality of the electrical connection between adjacent flakes in inhomogeneous regions. Figure 34(d) and (e) illustrate how the MIM signal varies with the quality of the electrical connection between the different graphene segments. MIM images can thus clearly identify which parts of a graphene flake are electrically contiguous.

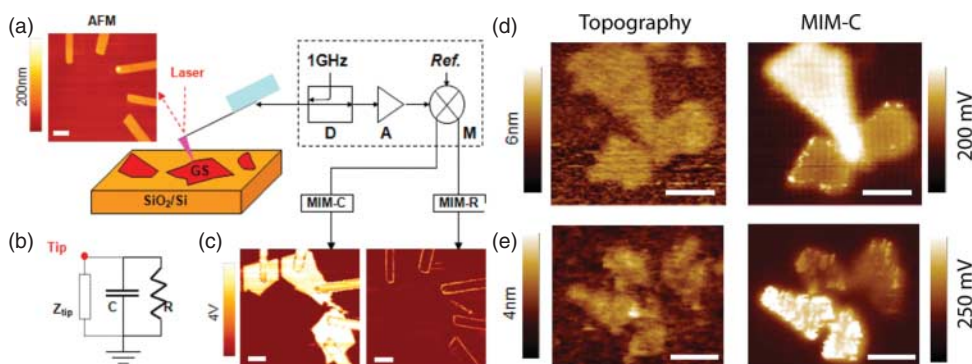


Figure 34. Implementation of microwave impedance microscopy (MIM) for mapping the conductivity response of graphene. Schematic representation of the MIM experiment (a), equivalent circuit (b) with the tip impedance  $Z_{\text{tip}}$  and sample resistance  $R$  and capacitance  $C$ . A 1 GHz signal is applied to the tip and the reflected signal is amplified and demodulated (D, directional coupler; A, amplifier; M, mixer). The MIM images (c) reveal the presence of pristine graphene flakes which are barely visible in the topography (a) (scale bar, 2  $\mu\text{m}$ ). Topography (d) and corresponding MIM capacitance map (e) for graphene flakes can reveal the electrical connectivity between regions of overlapped flakes (scale bar, 200 nm). (Adapted from W. Kundhikanjana *et al.*, *Nano Lett.* 9 (2009), pp. 3762–3765 [394]. Copyright 2009 American Chemical Society.)

*TERS of graphene and other carbon allotropes.* As discussed in Sections 4 and 5.2, Raman spectroscopy has found applications in the study of the carbon allotropes graphene and carbon nanotubes (CNTs) [395,396]. It can yield information such as the degree of  $sp^3$  hybridization, identify the presence of defects and impurities, and determine the CNT chirality, or number of graphene sheet layers [175]. Access to this information is facilitated by large intrinsic Raman cross-sections. Extending TERS for the nanoscale investigations of graphene and CNTs has therefore been a focus of considerable effort.

Initially, carbon nanotubes served as a model system to explore the resolution and sensitivity of tip-enhanced spectroscopy [397]. Through the tip-controlled pressure-induced shift in the G band [249] a resolution as high as 4 nm was demonstrated [250]. TERS has been used for structural characterization of CNTs [22,398], as the tube chirality can be determined from the combination of spectral position of the radial breathing mode and photoluminescence [399]. The D band can be used to probe the spatial distribution of defects in the tube [400]. Photoluminescence, which is also enhanced by the tip, yields insight into carrier migration and trapping by defects. CNTs have also been used to demonstrate the subsurface imaging capability of TERS [401].

Unlike CNTs, where the enhancement of the polarization parallel to the tip axes effectively drives the Raman response, this surface normal field enhancement couples poorly to graphene Raman modes with their in-plane polarizability [402]. Therefore, the Raman modes of pristine graphene, in particular, the G mode, show only a weak TERS enhancement [255,403]. The defect-related D mode, however, exhibits an appreciable TERS signal [403]. TERS is therefore very effective at probing the spatial distribution of defects. In addition, despite weak TERS enhancement, its signal strength remains sufficient for the identification of graphene layer thickness [404] based on the mode shape [402].

As an example, Figure 35(a) shows a TERS image acquired from exfoliated graphene and its spatial distribution of the 2D (green) and D (red) Raman bands. The different spectral characteristics of pristine and damaged graphene are shown in (b). The capability of TERS to probe local structural defects and inhomogeneities in carbon nanostructures with nanometer spatial resolution

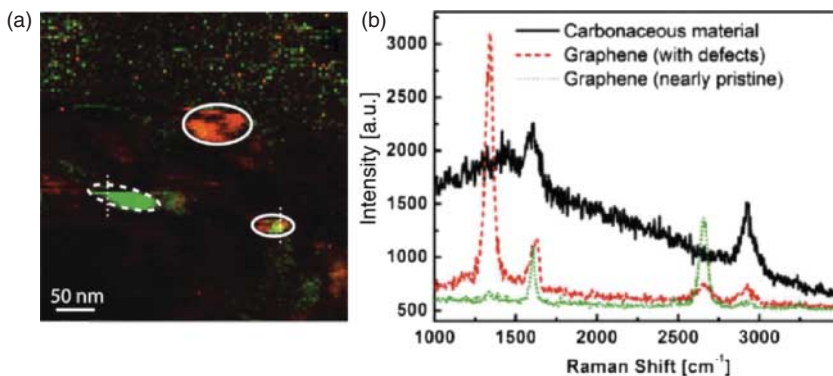


Figure 35. TERS  $400 \text{ nm} \times 400 \text{ nm}$  scan of exfoliated graphene on template stripped Au (a). Shown are the 2D band ( $2662 \text{ cm}^{-1}$ , green) and D Band ( $1350 \text{ cm}^{-1}$ , red) intensities. Regions with defects (white circles) and particularly strong graphene signals (white dashed circle) stand out, imaged with a spatial resolution of  $\sim 10 \text{ nm}$ . TERS spectra showing the characteristic Raman modes of graphene with high and low defect density (b), allowing for the discrimination of the corresponding spatial regions. Adapted from J. Stadler *et al.*, *Nano Lett.* 10 (2010), p. 4514 [254]. Copyright 2010 American Chemical Society.

can provide valuable information on structural domains in graphene, help identify the signal origin of far-field spectral characteristics, and guide graphene device fabrication.

### 6.2.2. Topological insulators

One of the first identified 3D bulk insulators with topological surface states was  $\text{Bi}_2\text{Se}_3$  [64], which exhibits a rhombohedral crystal structure composed of two Bi and three Se atomic sheets which are covalently bonded to form “quintuple layers” (QLs) of atoms. Similar to graphene, these quintuple layers can be generated through mechanical exfoliation, where dragging an AFM tip across  $\text{Bi}_2\text{Se}_3$  nanoribbons can produce varying thicknesses, down to one QL. These ultrathin  $\text{Bi}_2\text{Se}_3$  layers, with a few nanometers thickness, are expected to develop topologically non-trivial edge states. Some of the early characterizations performed using near-field microwave impedance microscopy (MIM) [405], which provides a high-resolution map of spatial variations in the local conductivity, which can be correlated with the AFM measurements of number of layers. Low conductivity was observed for one layer of  $\text{Bi}_2\text{Se}_3$ , with high conductivity for regions of 4 or 5 QLs. The observations agree with recent theoretical calculations and angle-resolved photo-emission experiments (ARPES) focusing on the 3D to 2D crossover for topological insulators [303,406]. For  $\text{Bi}_2\text{Se}_3$ , it was found that at 1 and 2 QLs, large energy gaps open up in both the bulk and the surface states. For three QLs and larger, the size of the surface gap begins to lessen. Hence, the correlation of the observed variation of the near-field response on the nanoscale with the predicted and measured band-structure of the material represents an excellent example of how near-field optical complements conventional macroscopic, spatially averaging sample characterization.

### 6.3. Domain imaging in ferroelectrics

This section describes the different methods by which FE domains can be imaged using near-field optical techniques. Since FE domains differ in crystallographic orientation, but otherwise have identical electronic and lattice structure, the optical contrast necessary for their identification and imaging must therefore be based on the optical anisotropy between the different domains. Optical

techniques for resolving domains include linear birefringence and other tensor-based selection rules in, e.g., Raman scattering and nonlinear spectroscopy.

### 6.3.1. Ferroelectric domains and domain walls

A FE material is a material that exhibits a spontaneous electric polarization  $P_s$  that can be reversed or reoriented by the application of an electric field  $E$  (poling). FEs have applications as, for example, nonvolatile memory devices and optical frequency converters [407]. The spontaneous polarization in the crystal is typically due to a relative structural displacement of the ions within the unit cell [169], where the magnitude of the displacement is the relevant order parameter. The Curie temperature  $T_C$  defines the phase transition temperature above which the spontaneous polarization is lost and the material turns paraelectric.

The net macroscopic polarization of a crystal is typically zero, due to domain formation in opposite polar directions. These domains arise from the competition between electric field energy, elastic energy, and domain wall energy, in order to minimize the total free energy of the system [408]. In equilibrium, the minimum energy in the absence of any defects would correspond to a single-domain configuration [169]. Such an equilibrium state is rarely achieved in a crystal in the absence of an external field, but has been observed in highly conducting FEs [164]. The domain walls are typically on the order of a few unit cells.

Domain structures and antiphase boundaries with typical dimensions ranging from 50 nm to 1  $\mu\text{m}$  determine technologically relevant properties such as conductivity, leakage currents, and field poling behavior [409–411]. Domain wall effects may be particularly significant in thin films, as typically domain size scales with film thickness [412,413].

Since the first direct observation of FE domains in bulk  $\text{BaTiO}_3$  and KDP crystals, various techniques that provide access to the topology of FE domains have been developed [169,414]. The scanning probe technique of piezoresponse force microscopy (PFM) can reveal nanoscale information on surface FE domain configurations [415,416], by monitoring piezoelectric surface displacements induced by the electrically biased probe tip [417–420]. While a powerful technique, this is an indirect way of measuring the electric polarization, and for the case of several different possible orientations of the spontaneous polarization, the results can be difficult to interpret.

The FE polarization in general gives rise to an associated anisotropic optical response wherever the optical response couples at least to some extent to the FE lattice distortion or the associated changes in the electronic properties. This is the case for a wide range of optical processes with suitable contrast for domain imaging arising from changes in, e.g., phonon modes, refractive index, electro-optic response, or crystallographic orientation. Both far-field and near-field techniques based on these different optical properties can then provide FE domain imaging contrast.

*Perovskite  $\text{BaTiO}_3$ .* The FE perovskites are of particular significance as model FEs due to their comparatively simple crystal structure [169]. An illustration of the prototypical perovskite  $\text{ABO}_3$  unit cell, with the A sites at the corners of the cubic lattice and the central B atom surrounded by oxygens at face center, is shown in Figure 36(a). This crystal phase is observed in many materials, including  $\text{BaTiO}_3$ ,  $\text{PbTiO}_3$ , and  $\text{SrTiO}_3$ . Also illustrated is the atomic displacement leading to the tetragonal FE phase observed in  $\text{BaTiO}_3$  and  $\text{PbTiO}_3$ . While this distortion is shown along the crystallographic  $z$ -axis, the corresponding distortions along the  $x$ - and  $y$ -axes are energetically equivalent.

Arguably, the most studied FE material to date has been  $\text{BaTiO}_3$ . It has been of crucial significance for the understanding of FE materials in general [169]. The tetragonal FE phase is observed under ambient conditions and occurs at temperatures below  $T_C = 393$  K, above which it transitions to the cubic paraelectric phase. Additional phases typical of perovskites are also observed,

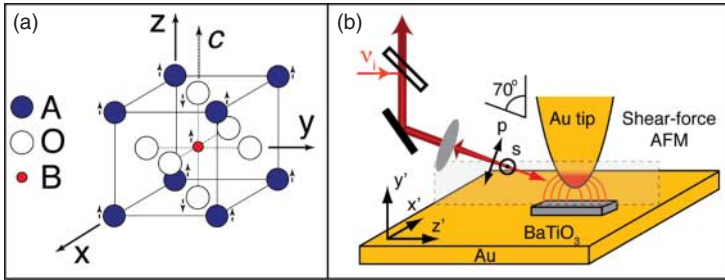


Figure 36. Illustration of the prototypical perovskite  $ABO_3$  unit cell with the A sites at the corners of the cubic lattice sites and the central B atom surrounded by oxygen octahedra (a). Also illustrated is the direction of ion migration observed during the transition to the tetragonal FE phase in, e.g.,  $BaTiO_3$  and  $PbTiO_3$ . Geometry of the experiment for the phonon Raman nanocrystallography TERS selection rules (b). The incident light is focused onto the tip-sample gap and the tip-scattered Raman signal, here collected in the backscattering direction, provides contrast via the phonon Raman anisotropy, reflecting different domain orientations. Adapted from S. Berweger *et al.* Nat. Nanotechnol. 4 (2009), p. 496 [316].

with the orthorhombic phase observed below 278 K and the rhombohedral phase below  $\sim 183$  K. While long thought to be a purely displacive FE, recent results indicate that  $BaTiO_3$  has a partial order-disorder nature, renewing fundamental interest [421].

### 6.3.2. Raman Phonon Nanocrystallography

This section describes the application of TERS for imaging FE domains, using  $BaTiO_3$  nanorods as a specific example [316]. Unlike molecular systems with localized vibrational modes, the delocalized lattice excitation with its lattice momentum introduces a wavevector-dependence in the phonon Raman response. As discussed previously, the combination of crystal orientation, incident and detected  $k$ -vector, and polarization, allows for selection of specific Raman tensor components which in turn reflect the crystal symmetry. Therefore, detection of certain combinations of LO and TO phonon modes provides optical crystallographic information. With consideration of the light polarization-dependent tip-enhancement, optical crystallography on the nanometer scale can be performed.

In the first demonstration,  $BaTiO_3$  microcrystals were investigated, motivated by the question of domain ordering in crystallites of sizes smaller than typical domain sizes in bulk material. With increasing surface area to volume ratio, the increase of the surface depolarization fields is expected to affect domain formation and phase transition behavior [178].

*Selection rules for optical phonon TERS.* The room temperature tetragonal FE phase of  $BaTiO_3$  has tetragonal symmetry with 4 mm (Schönflies:  $C_{4v}$ ) space group. It has three strong polar Raman active modes, the  $A_1$  mode and two degenerate  $E_1$  modes [164] with tensors

$$A_1(z) = \begin{pmatrix} a & 0 & 0 \\ 0 & a & 0 \\ 0 & 0 & b \end{pmatrix}, \quad E(x) = \begin{pmatrix} 0 & 0 & c \\ 0 & 0 & 0 \\ c & 0 & 0 \end{pmatrix}, \quad \text{and} \quad E(y) = \begin{pmatrix} 0 & 0 & 0 \\ 0 & 0 & c \\ 0 & c & 0 \end{pmatrix}, \quad (64)$$

where  $x$ ,  $y$ , and  $z$  denote the phonon polarization directions along the corresponding crystallographic axes, as illustrated in Figure 36(a).

Taking into account the tip-enhancement, the effective polarization for the  $N$ th phonon mode is  $\mathbf{P}_{\text{eff},N} = \vec{F} \vec{R}_N \vec{F}' E_{\text{inc}}$ . For the specific laboratory frame coordinates shown in Figure 36(b),

Table 1. Tip-enhanced phonon Raman selection rules for tetragonal BaTiO<sub>3</sub>. Here a crystal is oriented parallel with respect to the incident and scattered light. For each domain, the crystal coordinates are rotated to reflect the change in FE orientation (i.e.  $c \parallel z$ ). Contributions under the weakly enhanced  $s_{in}s_{out}$  configuration, or under oblique incidence (weak E LO mode) are neglected. From Ref. [316].

$\mathbf{q} = \mathbf{k}_i - \mathbf{k}_s$	Mode	$\mathbf{k}_i(\mathbf{e}_i\mathbf{e}_s)\mathbf{k}_s$	$I_{TERS}$	Domain
$\mathbf{q} \parallel z$	$A_1^{LO}$	$z(yy)\bar{z} = p_{in}p_{out}$	$\propto  a_{LO} ^2(F_p F'_p)^2$	$c$
$\mathbf{q} \parallel y$	$A_1^{TO}$	$y(xx)\bar{y} = p_{in}p_{out}$	$\propto  c_{TO} ^2(F_p F'_p)^2$	$a_y$
$\mathbf{q} \parallel y$	$E^{TO}$	$y(xz)\bar{y} = p_{in}s_{out}$	$\propto  c_{TO} ^2(F_s F'_p)^2$	$a_y$
$\mathbf{q} \parallel y$	$E^{TO}$	$y(zx)\bar{y} = s_{in}p_{out}$	$\propto  c_{TO} ^2(F_p F'_s)^2$	$a_y$
$\mathbf{q} \parallel x$	$A_1^{TO}$	$x(zz)\bar{x} = p_{in}p_{out}$	$\propto  b_{TO} ^2(F_p F'_p)^2$	$a_x$
$\mathbf{q} \parallel x$	$E^{TO}$	$x(zy)\bar{x} = p_{in}s_{out}$	$\propto  c_{TO} ^2(F_s F'_p)^2$	$a_x$
$\mathbf{q} \parallel x$	$E^{TO}$	$x(yz)\bar{x} = s_{in}p_{out}$	$\propto  c_{TO} ^2(F_p F'_s)^2$	$a_x$

the input and output tip enhancement tensors  $\overleftrightarrow{F}$  and  $\overleftrightarrow{F}'$  take the form

$$\overleftrightarrow{F} = \begin{pmatrix} F_s & 0 & 0 \\ 0 & F_p & 0 \\ 0 & 0 & 0 \end{pmatrix} \quad \text{and} \quad \overleftrightarrow{F}' = \begin{pmatrix} F'_s & 0 & 0 \\ 0 & F'_p & 0 \\ 0 & 0 & 0 \end{pmatrix}. \quad (65)$$

The radial tip symmetry and the weak depolarization yield diagonal tensors.  $F_p \simeq F'_p$  and  $F_s \simeq F'_s$  is a good approximation because of the generally lower phonon frequencies compared to molecular modes and in relation to the possible tip plasmon linewidth [300].

Table 1 shows the phonon TERS selection rules for three distinct crystallographic orientations, representing the three possible orthogonal FE domain configurations, for the backscattering geometry shown in Figure 36(b), with the incident and phonon Raman-scattered  $k$ -vectors approximately parallel with respect to the sample surface. Domains oriented parallel with respect to the length of the microcrystals are referred to as  $c$ -domains, while the  $a_x$  and  $a_y$  domains are oriented perpendicular to  $c$  in the sample plane and along the surface normal, respectively. Modes only present under the weakly enhanced  $s_{in}s_{out}$  configuration (e.g.  $A_1^{LO}$  for  $c$ -domain) have been omitted, as well as the  $E^{LO}$  mode, which is weak and only excited under oblique angle of incidence (e.g.  $\mathbf{q} \parallel x$  and  $x(zx)\bar{x}$ ) [164].

*FE nano-domains in BaTiO<sub>3</sub> microcrystals.* Figure 37(a) shows a tip-enhanced phonon Raman spectrum acquired on a BaTiO<sub>3</sub> nanorod with unpolarized detection. The two main peaks are the  $A_1^{TO}$  mode at 516 cm<sup>-1</sup> and the  $E^{LO}$  at 715 cm<sup>-1</sup>. Also contributing to the signal are the weaker and spectrally unresolved  $A_1^{LO}$  mode at 727 cm<sup>-1</sup> and the  $E^{TO}$  at 487 cm<sup>-1</sup> [422]. The observation of the Raman-active LO modes is characteristic of the FE state. An approach curve, shown in Figure 37(b), verifies the tip-enhanced near-field localization of the signal. A line scan across the rod is shown in Figure 37(c) with the corresponding topography shown in white. The obtained Raman enhancement of 10<sup>4</sup>–10<sup>5</sup> is consistent with the typical field enhancement of the tips of order  $F \sim 10$ –20.

Imaging of FE domains in BaTiO<sub>3</sub> is shown in Figure 38. Panel (a) shows the sf-AFM topography of the BaTiO<sub>3</sub> crystal with the corresponding spectrally integrated optical Raman signal (b). In addition to the overall reduced signal observed with the tip positioned above the rod, a region  $\sim 60 \text{ nm} \times 200 \text{ nm}$  of significantly stronger near-field signal is seen.

With the incident  $k$ -vector oriented along the rod and on the basis of Table 1, it can be deduced from the weak  $A_1^{LO}$  signal that most of the crystal has a  $c$ -domain orientation. In contrast, for the  $a_x$  and  $a_y$  domain configurations, corresponding to domains oriented perpendicular to the

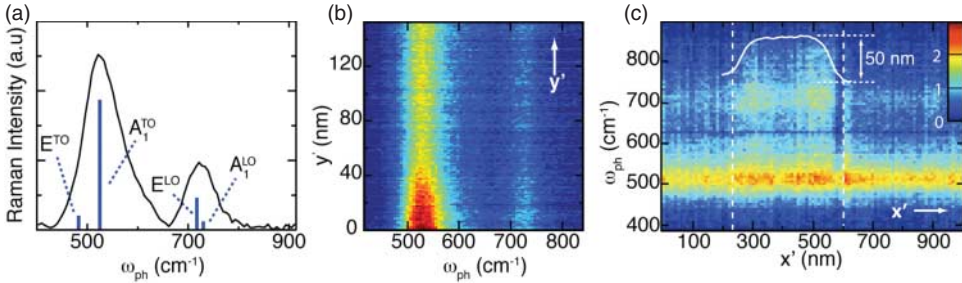


Figure 37. Phonon Raman TERS spectrum acquired on top of a BaTiO<sub>3</sub> nanorod with phonon mode assignment (a). Corresponding tip-sample distance dependence (b). Spectrally resolved line scan across the BaTiO<sub>3</sub> crystal (c) and topography (white line). Adapted from S. Berweger *et al.*, Nat. Nanotechnol. 4 (2009), p. 496. [316].

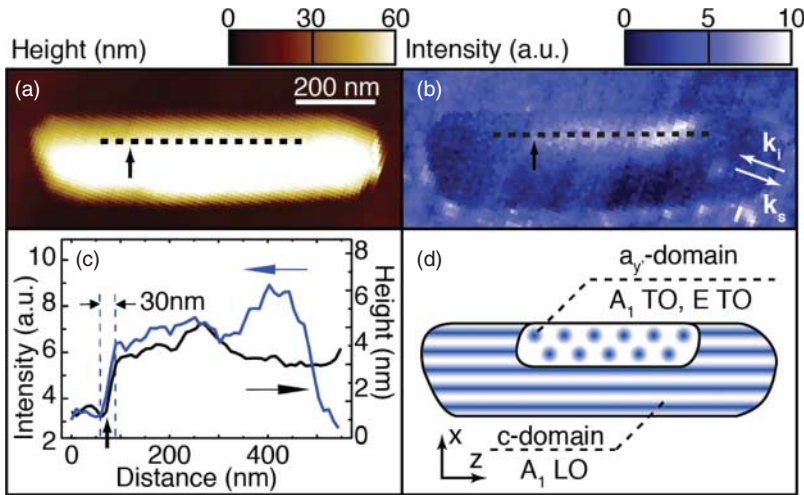


Figure 38. Shear-force AFM Topography (a) of a BaTiO<sub>3</sub> microcrystal and the spectrally integrated TERS image (b) showing FE domain contrast. (c) Cross-section along the dashed lines in panels (a) and (b). (d) Domain assignment based on the Raman selection rules. See text for details. Adapted from S. Berweger *et al.*, Nat. Nanotechnol. 4 (2009), p. 496 [316].

length of the rod, the  $E(x)^{TO}$ ,  $E(y)^{TO}$ , and the strong  $A_1^{TO}$  modes contribute. The main contrast to distinguish the dark  $c$ - from bright  $a$ -domains arises from the phonon propagating parallel or perpendicular with respect to the phonon polarization direction, exciting either the weak  $A_1^{LO}$  or strong  $A_1^{TO}$  modes.

While a further distinction of the  $a_x$  and  $a_y$  domains is not possible in the backscattering configuration, it is possible to identify the type of domain based on the shape. Since the domain boundaries of 90° domains in BaTiO<sub>3</sub> are oriented at 45° [169], the observation of a surface domain boundary parallel to  $z$  is characteristic of an  $a_y$ -domain. Thus, the domains are assigned as shown in Figure 38(d). Cross-sectional plots of the topography (a) and optical signal (b) along the respective dashed line and as shown in (c) further corroborates the domain assignment, showing a domain-boundary-induced topographic feature [423]. As shown in Figure 38(c), the lateral spatial resolution obtained is better than 30 nm.

Unlike molecular systems that can benefit from large Raman cross-sections further increased by resonant excitation, crystalline systems generally suffer from small Raman cross-sections. Even for crystalline materials with very large Raman cross sections a volume of  $\sim 1 \text{ nm}^3$  is required to obtain a cross-section comparable to that of a resonant dye molecule [315]. Nevertheless, from the near-field Raman spectra as in Figure 37(a), such a small sample volume is sufficient to provide simultaneous chemical identification as well as FE phase assignment. With only small changes in the lattice constant arising from the FE distortion these can be difficult to resolve even via high-resolution TEM, but can readily be identified due to the high symmetry selectivity of the phonon Raman response.

The results show that while the rods are smaller than typical FE domains, they are not necessarily single domain. This indicates that an increase in surface to volume ratios and the associated increasing importance of the surface free energy, including adsorbates and surface defects, may induce finite size effects on FE ordering.

### 6.3.3. Other techniques for near-field imaging of ferroelectric domains

FE domain contrast can also be achieved via the anisotropy of the microwave dielectric response, the electro-optic response, and SHG with imaging capability in corresponding near-field implementations. In many early studies, however, the use of sometimes poorly characterized and frequently polycrystalline samples, led to difficulties in distinguishing the optical FE contrast from the influence of grains, defects, and the substrates to the near-field signal. Several recent studies on well-defined samples have explored different promising new near-field contrast mechanisms, including probing domain dynamics under external fields.

*Linear optical response.* The strain at domain walls leads to a small change in the index of refraction, which can be detected through polarization sensitive measurements. This has been demonstrated using NSOM in illumination mode with 633 nm light, on  $\text{LiTaO}_3$  crystals [424,425], with a lateral resolution of about 200 nm. In collection mode, a higher resolution of  $\sim 100 \text{ nm}$  was achieved for  $\text{LiNbO}_3$  and  $\text{LiTaO}_3$ , with a transmission geometry [426,427]. These experiments provided demonstration of the capability for monitoring domain wall motion under externally applied fields. The domain walls were observed to be pinned at defects and to bow around these positions under the applied electric field [426].

Higher contrast and resolution can be obtained with IR *s*-SNOM, if the laser frequency is tuned to be resonant with a specific optical phonon mode in the material. The FE polarization-induced lattice change can lead to an anisotropy and dichroism or birefringence in the optical phonon response. The associated frequency shifts of the phonon polarization with respect to different crystallographic directions can be detected in the amplitude or phase of the near-field signal at near-resonant infrared excitation. This was demonstrated for the case of  $\text{BaTiO}_3$  [428], where  $\epsilon_{xx} = \epsilon_{yy} \neq \epsilon_{zz}$ , due to the tetragonal crystal structure, with the *z*-direction corresponding to the crystallographic *c*-axis (Figure 39). From the phonon spectrum (c) of the different tensor components it can be seen that there is a large contrast between  $\epsilon_a$  ( $\epsilon_{xx}$ ) and  $\epsilon_c$  ( $\epsilon_{zz}$ ) near a wavelength of  $20 \mu\text{m}$ , due to the proximity to the A1 and E TO modes. Figure 39(b) shows the corresponding spatially resolved domains, imaged at two wavelengths, 17.2 and  $16.7 \mu\text{m}$ . At  $\lambda = 17.2 \mu\text{m}$ , the signal from *a* domains is resonantly enhanced and they appear bright. For  $\lambda = 16.7 \mu\text{m}$ , the opposite situation applies and contrast is reversed.

It should be noted in general that the details of the contrast obtained, both in terms of amplitude and phase, can sensitively depend on a range of experimental parameters. Those include the dynamic variation of coupling with the tip-dither motion, the role of far-field interference and surface reflection, details of the tip geometry affecting coupling and scattering, as well as contributions due to variations in the surface topography.

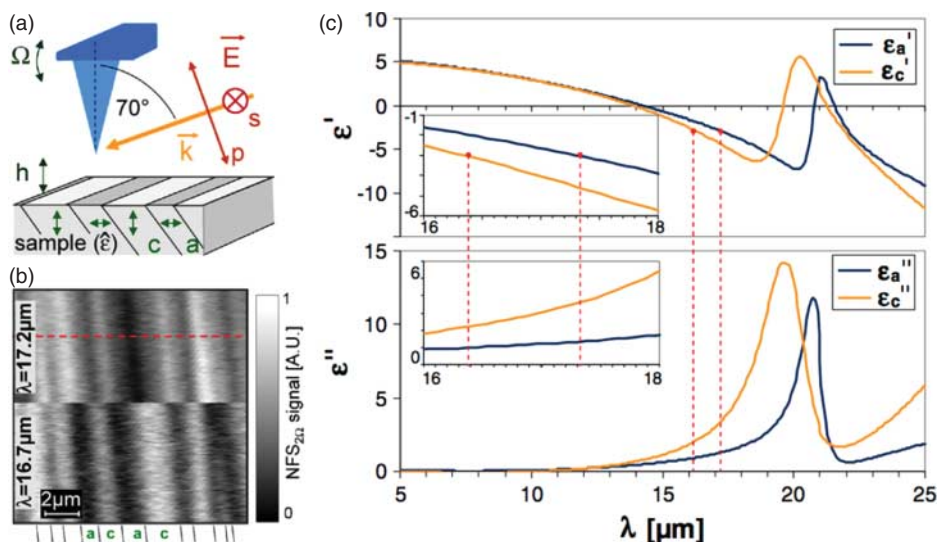


Figure 39. Schematic of the experimental configuration for IR *s*-SNOM imaging of FE domains in BaTiO<sub>3</sub> (a) IR *s*-SNOM contrast, (b) reflecting the alternation of *a* and *c* domains. Contrast reversal due to the phase change in effective polarizability for the two different wavelengths used (red dashed lines in (c)). Spectral dependence of real and imaginary parts of dielectric function (c) with phonon polarization parallel and perpendicular with respect to the *c*-axis. (Adapted from S.C. Kehr, Phys. Rev. Lett. 100 (2008), pp. 256403 [428]. Copyright 2008 American Physical Society.)

*Electro-optic domain imaging.* The use of the electro-optic response (Pockels effect) for imaging requires an external field, but can nevertheless be compatible with studying dynamical behavior through careful demodulation of the signal response. With conventional tapping mode AFM feedback and lock-in detection, *s*-SNOM implementations can resolve domains through a phase contrast. A small AC modulation of a bias field can induce a 180° phase shift in the optical signal as the spontaneous polarization switches directions, and can be used to reveal 180° domains perpendicular to the surface in bulk triglycine sulfate [429]. However, there are several possible effects which can distort the FE response, for example, piezoelectric deformation and modulated tip-sample coupling.

A similar detection mechanism, with transmissive geometry, was utilized in order to image domains in Ba<sub>x</sub>Sr<sub>1-x</sub>TiO<sub>3</sub> thin films [17,430]. Changes in the domain structure for different applied fields confirmed the origin of the optical contrast. Subsequent measurements with a GHz modulation generated by Ti:Sa pulses [431] enabled time-dependent measurements of the dynamics of the FE domains with sub-picosecond temporal resolution.

*SHG domain imaging.* In the introduction to light–matter interactions (Section 3), it was noted that SHG provides a direct probe of symmetry breaking associated with e.g. ferroelectricity. SHG, therefore, provides a more specific mechanism for probing FE domains than linear techniques, with higher contrast and without the need for demodulation, though with an overall weaker signal.

Measurements of near-field SHG using NSOM on FE single crystal samples revealed domain walls and poling structures in LiNbO<sub>3</sub> [192], with a spatial resolution of 150 nm. In this case, no phase sensitive detection was employed and the contrast arose from the enhancement of the SHG signal at the domain wall. The degree of contrast depended on the relative orientation of the domain wall and SH polarization, with almost no contrast observed when the two were parallel. The sensitivity of SHG to local crystal orientation was demonstrated on BaTiO<sub>3</sub> and PZT thin

films [432]. These experiments were in NSOM collection mode, and with careful polarization analysis the direction of the FE spontaneous polarization could be extracted [338]. The use of *s*-SNOM for SHG FE domain imaging has also been demonstrated [433]. This implementation utilized a transmission geometry with tapping mode AFM and tungsten tip in order to investigate  $\text{Sr}_5\text{Ba}_{1-x}\text{Nb}_2\text{O}_6$  thin films. The varying SHG signal again depended on local crystallite orientation, and it was not possible to extract additional orientational or FE information. However, this geometry allows simultaneous near-field and transmission far-field imaging, making it possible to separate and study surface and bulk effects.

While SHG *s*-SNOM is comparatively under-utilized it has significant promise as a probe of correlated matter. The virtue of SHG as a coherent nonlinear optical technique is its sensitivity to higher-order symmetry compared to linear optics, with the ability for phase sensitive detection. This allows for discrimination between  $180^\circ$  FE domains, difficult with any other technique. We discuss that in the context of imaging of magnetic and multiferroic material where the simultaneous ability of SHG to be sensitive to any ferroic order in general could greatly expand capabilities of tip-enhanced *s*-SNOM SHG.

#### 6.4. Magnetic domain imaging

FM domain imaging was successfully demonstrated early in the development of near-field microscopy, as the optical contrast is largely decoupled from topographic sample inhomogeneities, in contrast to many other sample properties. The use of NSOM for domain visualization can be very valuable, as the contrast does not rely on the presence of a possibly perturbing magnetic field (e.g., magnetized tips in magnetic force microscopy). As a purely optical technique it is non-perturbative, and allows for the study of domain dynamics. Both the magneto-optical Faraday effect and the magneto-optical Kerr effect can provide magnetic near-field contrast. Unlike near-field electro-optical imaging (previous section), magneto-optical imaging does not require signal demodulation, but its achievable spatial resolution in its *s*-SNOM implementation is low (as discussed below). Magnetic SHG is also compatible with both fiber-based NSOM and apertureless *s*-SNOM, and generally allows higher sensitivity and contrast.

##### 6.4.1. Magnetic domains

Magnetic ordering arises from the interaction of atomic spins in unfilled *d* and *f* orbitals, and therefore depends very sensitively on crystal structure. The most common form of magnetic ordering is anti-ferromagnetism (a-FM), where in the simplest manifestation, adjacent spins are aligned in anti-parallel directions. This produces symmetry-ordering behavior with no net magnetic moment below the magnetic ordering (Néel) temperature  $T_N$ . Ferromagnets possess a spontaneous polarization below the Curie temperature  $T_C$ , analogous to the FE polarization discussed in the previous section. All magnetically ordered materials can be assigned to a magnetic point group, based on the symmetries of their spin ordering [136]. In particular, time reversal is equivalent to spin reversal, providing another symmetry element in combination with the geometric symmetry elements. The broken time-reversal symmetry of spins can be illustrated by the Faraday effect, where the sign of the induced optical polarization rotation depends only on the direction of the **B** field, through the local sample magnetization *M*, but not the direction of light propagation. Similar to the case of FEs, domains with uniform magnetization or a-FM spin direction form even in otherwise homogeneous materials in order to minimize total energy [413]. The domain sizes are usually on the order of  $1\ \mu\text{m}$ – $1\ \text{mm}$ , but this varies significantly depending on bulk or thin film samples, crystallinity, etc. In contrast to FE domain walls, magnetic domain walls typically have a width of several hundred lattice constants, due to the spin interaction energy opposing an abrupt transition in magnetization orientation. Understanding of the nucleation of these domains,

the effects of domain walls, and interaction with grains in polycrystalline materials are important for memory storage applications.

#### 6.4.2. Magneto-optic domain imaging

The contrast in magneto-optic domain imaging arises from polarization effects due to off-diagonal components in the permittivity tensor (Section 3.2). For magnetization  $m$  along the  $z$ -axis, the permittivity tensor has the form

$$\overleftrightarrow{\epsilon} = \begin{pmatrix} \epsilon_{xx} & 0 & 0 \\ 0 & \epsilon_{yy} & 0 \\ 0 & 0 & \epsilon_{zz} \end{pmatrix} + \begin{pmatrix} 0 & -im & 0 \\ im & 0 & 0 \\ 0 & 0 & 0 \end{pmatrix}. \quad (66)$$

The imaginary off-diagonal elements cause a rotation in the polarization of light on transmission through a material (Faraday effect) or reflection off a surface (Kerr effect), which can then be converted to a contrast image through input and output polarizers.

Measurements of ferroic order in the near-field were performed soon after the invention of the NSOM, using illumination mode to image the stripe domain pattern in a thin film of yttrium ion garnet (YIG) [8]. Domain contrast was obtained due to the rotation of the polarization from the magneto-optical Faraday effect, detected through polarization analysis, with 30 nm spatial resolution [8,434,435]. This was followed soon after by the demonstration of writing and reading magnetic domains in a Co/Pt thin film with NSOM [434]. However, the high laser power required for the writing process may have led to tip damage from the temperature increase, and these experiments proved difficult to reproduce.

Subsequent measurements based on the Faraday effect have resolved domain structure with  $< 100$  nm spatial resolution in a variety of magnetic systems [436–442]. The resolution that can be achieved in these experiments is very sensitive to the angle of incidence, the relative angle of magnetic domain walls, the polarization of light, and the thickness of the magnetic film [443]. The wide angle at which light is emitted from the tip aperture also tends to lead to “smearing” at domain walls and therefore reduces the spatial resolution [444]. While this form of NSOM implementation is sensitive to magnetization out of the plane of the sample (the polar magneto-optical effect [445]), the in-plane magnetization is more difficult to study [446]. Furthermore, many of these measurements were on rough thin films, leading to topographic crosstalk, and difficulty interpreting results. Also, there is some degree of depolarization of the light propagating through the fiber [437,439], and the probe tip can also cause a large amount of depolarization [439], thus reducing sensitivity and achievable contrast.

Another approach is to take advantage of the time-reversal asymmetry associated with magnetic phenomena. The Sagnac interferometer relies on the interference between two beams which counter-propagate within a fiber (see Figure 40(a)) [447], where a phase difference can be induced due to the breaking of time-reversal symmetry, translating into an intensity change at the detector [448,449]. Sagnac interferometric near-field imaging is insensitive to any optical birefringence in the fiber, compared to standard MOKE techniques. However, the need for simultaneous detection and illumination via the NSOM tip does limit the intensity with radiation coupling in and out of the aperture. A typical experimental implementation for Sagnac interferometric near-field imaging is shown in Figure 40(a). A topographic (b) and near-field image (c) of a TeFeCo hard drive, using this technique, shows the written magnetic bits as dark regions.

One of the difficulties of linear magneto-optical NSOM is detecting in-plane components of the magnetization at normal incidence. This is due to the fact that while it is possible to have polarization control of the illumination, in NSOM collection mode predominantly in-plane polarized waves will couple into the fiber [446], but only the out-of-plane waves will produce a magnetic signal

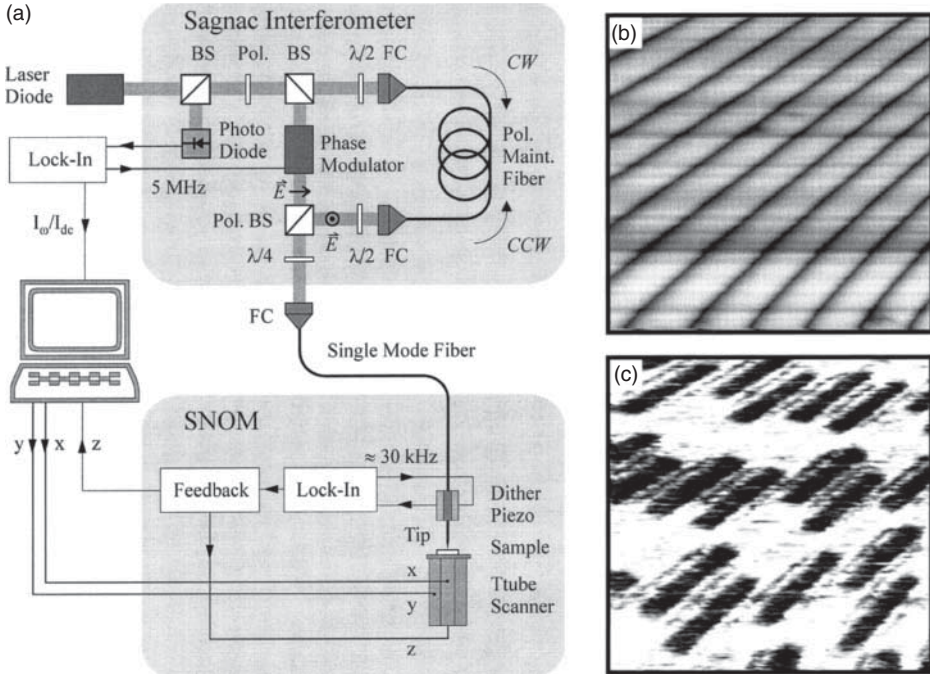


Figure 40. Schematic of Sagnac interferometer, with clockwise and counter-clockwise beam paths, coupled to a shear force AFM for near-field magneto-optical imaging (a). Shear-force topography (b) and optical image (c) of a TeFeCo hard disk. The scan size is  $14 \times 14 \mu\text{m}$ . Dark areas represent the written magnetic bits. (Adapted from A. Bauer *et al.*, J. Microsc. 194 (1999), pp. 507–511 [447]. Copyright 1999 Wiley.)

for in-plane magnetization. Apertureless *s*-SNOM can nominally detect all polarization components, but with the selective field enhancement for *p* polarization, the geometry is more sensitive to the in-plane magnetization. However, in the linear magneto-optical implementation *s*-SNOM suffers from unexpectedly low resolution. The highest yet reported resolution for an apertureless magneto-optical measurement is only  $\sim 200 \text{ nm}$ , while fiber-based NSOM has already achieved  $\sim 20 \text{ nm}$  [442,450–452]. This loss of spatial resolution with *s*-SNOM arises from the interaction of electromagnetic modes at the apex of the tip with the sample magnetic response. The most confined  $m = 0$  mode provides a singularity at the tip which enables the typically high spatial resolution in *s*-SNOM measurements. However, this mode will not contribute a magneto-optical signal due to the axial nature of the magnetic field. The signal arises from higher order, much less spatially confined modes [443] and the achievable resolution is lower. Thus, while for almost all near-field applications, *s*-SNOM provides considerable advantages over fiber-based NSOM, this is not the case for linear probing of magnetic fields. The magneto-optical *s*-SNOM implementation may benefit from engineered tip geometries, for example, with enhanced tip-perpendicular polarization sensitivity [232].

6.4.3. Magnetic SHG domain imaging

In contrast to linear optical techniques for magnetic-domain imaging, magnetic second harmonic generation (MSHG) provides high contrast and sensitivity to essentially all forms of magnetic ordering. Soon after the invention of NSOM, the possibility of using nonlinear processes attracted interest, in particular, because of the surface selectivity of SHG for media with bulk inversion

symmetry [453,454], including the case of MSHG. SHG implementations of near-field microscopy allow enhanced sensitivity to magnetization orientation, but care must be taken to account for depolarization effects from the tip (including imperfections of radial symmetry) and the distortion of the electromagnetic interaction between the probe tip and surface. While the field enhancement effect is generally small for NSOM fibers and typically can be neglected in linear measurements, the high intensities required for nonlinear characterization can lead to substantial modifications in SH generation [338,432,455].

Second-harmonic near-field imaging was demonstrated using NSOM in collection mode with uncoated glass fiber tips in order to reduce probe heating issues [456]. The intensity variations in the SH signal on a Ni(100) surface, with few micrometer size, were concluded to represent magnetic domains with different orientations of magnetization. These domains were not correlated with topographic features and could be manipulated through an external field. Additionally, the domain wall transition region was found to be approximately 150 nm, close to the Bloch wall thickness. Subsequently, the ability of SHG NSOM to study in plane magnetic domains was demonstrated on garnet films in transmission [457], and Co thin films [458].

### 6.5. *Multiferroics: Coupled ferroic order and domains*

In the previous sections, we have discussed the application of *s*-SNOM in different optical implementations which allow for probing of FE and magnetic order by taking advantage of optical anisotropies associated with specific tensor-based selection rules, enhanced and modified by the tip symmetry. One unique yet poorly understood class of correlated matter are materials that exhibit multiple ferroic order parameters simultaneously, associated with highly complex domain patterns and coupling between the ferroic orders. Here, the application of *s*-SNOM, in particular, in combination with nonlinear optical probing which can be sensitive to those coupled order parameters, could prove very powerful in determining the underlying microscopic processes responsible for the multiferroic behavior.

In a multiferroic material at least two types of ferroic order coexist in the same phase, such as FE, FM, or ferroelastic [241]. Of particular fundamental and technological interest are materials which display FE and some form of magnetic ordering simultaneously. These could possess large magnetoelectric coupling, so that a magnetic field can tune the electric polarization and an electric field the magnetic ordering [459,460]. Multiferroics have intensively been studied in recent years for their potential spintronics and storage applications [461,462]. However, intrinsic multiferroic materials are rare, due to the competition between the standard mechanisms for FE and FM ordering. Typically, magnetism occurs in metallic materials with unpaired, localized electrons, whereas conventional ferroelectricity preferentially arises in dielectrics from the displacement of cations with empty *d* shells, such as  $\text{Ti}^{4+}$  in  $\text{BaTiO}_3$  [463,464]. Despite this apparent tendency for these different order phenomena to exclude each other, multiferroicity is allowed in certain classes of materials, the most common of which are the hexagonal manganites, such as  $\text{YMnO}_3$  (discussed in Section 6.5.1), in addition to bismuth ferrite  $\text{BiFeO}_3$ .

As is the case in FEs, domains and domain walls are known to play a critical role in determining macroscopic properties in multiferroics, but their formation, density, and dynamics are poorly understood. In multiferroics, depending on the energy associated with coupled versus free domain walls, the coexistence of electric, elastic, and magnetic ordering can be complex. The ability to study domains with a technique simultaneously sensitive to several ferroic phases, in particular FE and magnetic ordering, is therefore highly desirable for the understanding of the driving mechanisms behind the coupled order parameter in multiferroics.

In the following sections, we provide background on the hexagonal manganites and their microscopic properties, as a system where nonlinear *s*-SNOM has already demonstrated its power

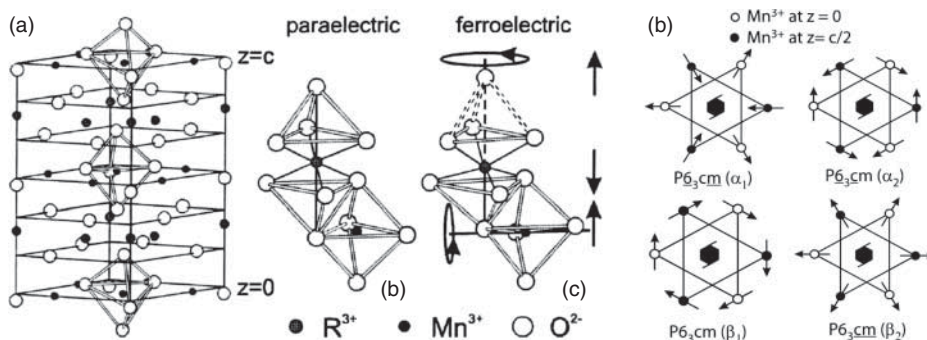


Figure 41. Lattice structure of YMnO<sub>3</sub> in the FE phase (a). The canting and rotation of the MnO<sub>5</sub> polyhedra in the center and the associated displacement in Y breaks the inversion symmetry and produces the FE phase. Possible spin configurations for a-FM ordering (b), and their associated space groups. (Adapted from M. Fiebig *et al.*, J. Opt. Soc. Am. B 22 (2005) pp. 96–118 [51]. Copyright 2005 Optical Society of America.)

for imaging complex nanometer scale domain structure, and can provide further information that is difficult to access with conventional microscopy techniques.

#### 6.5.1. Hexagonal manganites

The hexagonal manganites are a subclass of the RMnO<sub>3</sub> system, where R is a large lanthanide or alkaline earth metal. For R atoms with radius smaller than Ho (R = Sc, Y, Ho, Er, Tm, Yb, Lu, Dy), the structure is non-centrosymmetric hexagonal, with space group P6<sub>3</sub>cm (point group 6mm). These materials have attracted interest as one of the few known systems where electric and magnetic ordering are intrinsically not contradictory.

The FE ordering ( $T_C \sim 570$ – $990$  K) is of an unconventional, geometric nature, arising from the distortion and trimerization of Mn<sup>3+</sup>O<sub>5</sub> polyhedra. The associated corrugation in the rare earth R<sup>3+</sup> ions lowers the symmetry and induces a spontaneous polarization along the hexagonal  $c$ -axis  $\mathbf{P}_s = (0, 0, P_z)$  [284,465] (Figure 41(a)). The value of the spontaneous polarization in YMnO<sub>3</sub> was measured at  $5.5 \mu\text{C}/\text{cm}^2$  [466] for an epitaxially grown film, and a value of  $6.2 \mu\text{C}/\text{cm}^2$  was theoretically derived [467]. For comparison conventional perovskite FEs have values nearer to  $25 \mu\text{C}/\text{cm}^2$ , the value for BaTiO<sub>3</sub>.

At a Néel temperature of 60–130 K, the Mn<sup>3+</sup> ions, in a high spin  $s = 2$  state, become antiferromagnetically ordered in the  $xy$  plane, with four possible triangular magnetic symmetries (denoted  $\alpha_1$ ,  $\alpha_2$ ,  $\beta_1$ , and  $\beta_2$ ), shown in Figure 41(b), and another four “transitional” structures [468]. Only the  $\alpha$  symmetry has been observed in RMnO<sub>3</sub> systems using far-field SHG [198,468], with magnetic space groups  $P\bar{6}_3cm$  and  $P6_3c1m$ . These two  $\alpha$  structures differ only in the orientation of the spins with respect to the crystal  $x$ -axis, which can be probed using SHG through the choice of polarization, but cannot be easily distinguished using standard diffraction techniques [469].

#### 6.5.2. Domain coupling in hexagonal manganites

As discussed in Section 3.2, SHG is unique in its sensitivity to both FE and a-FM order parameters. The use of far-field SHG in the study of the hexagonal manganites demonstrated the importance of domain walls to magnetoelectric coupling in these materials [51,198]. As shown in Figure 11, in poled YMnO<sub>3</sub> crystals the walls of macroscopic FE domains coincide with a-FM domain walls, with additional free a-FM domains. This means that any reversal of the FE order parameter is correlated with a reversal of the a-FM order parameter, but the mechanism for this coupling is

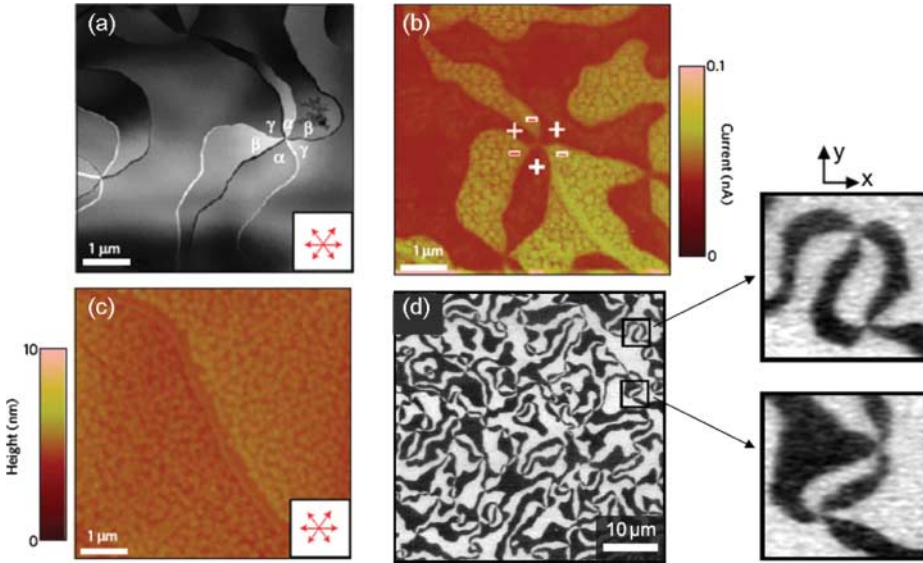


Figure 42. TEM (a), conductive-AFM (b), topographic (c), and PFM (d) scans showing the cloverleaf domain structure associated with coupling of structural and FE domain walls. The vortex patterns arise from the meeting of six domains, with three structural domains combining with the two FE polarizations. (a), (b), and (c) reprinted by permission from Macmillan Publishers Ltd: T. Choi *et al.*, *Nat. Mater.* 9 (2010), pp. 253–258 [69], copyright 2010, (d) adapted from T. Jungk *et al.*, *Appl. Phys. Lett.* 97 (2010), p. 012904 [101], copyright 2010 American Institute of Physics.

not well understood. A domain wall-mediated interaction has been proposed as a mechanism for coupling, but it is not clear how the interaction is affected by the different standard sizes of FE and a-FM domain walls ( $\sim 10$  unit cells versus  $\sim 1000$  unit cells).

In  $\text{YMnO}_3$ , recent studies of the FE domain structure have found intriguing structural details of the domain order on short length scales. Complex topological and FE interactions lead to persistent vortex-like nanoscale domain structures, shown from conductive AFM and TEM [470] and piezoresponse force microscopy (PFM) [101] in Figure 42. The domain features are stable topological defects that cannot be readily removed by poling, and represent a fundamentally different texture compared to conventional FE domains [471], demonstrating that the microscopic basis for the macroscopic domain wall pinning observed in Figure 11 is not trivial.

These studies highlight the importance of spatially resolved investigation of both FE and a-FM properties on the single-domain level and especially at domain walls, in order to investigate conduction, magnetoelectric coupling, and the impact of domain wall movement and hysteresis on the macroscopic properties.

### 6.5.3. SHG *s*-SNOM imaging

The combination of SHG with tip-enhanced *s*-SNOM can provide information about multiple intrinsic ferroic parameters simultaneously, with high spatial resolution, and is therefore ideal for the investigation of multiferroic materials. The high ferroic contrast and spatial resolution has been demonstrated in SHG *s*-SNOM by performing FE domain imaging in single crystal  $\text{YMnO}_3$  [14].

The hexagonal 6 mm crystal class has non-zero second-order susceptibility components  $\chi_{xx}^{(i)} = \chi_{yy}^{(i)}$ ,  $\chi_{xz}^{(i)} = \chi_{yz}^{(i)}$ ,  $\chi_{yyz}^{(i)}$ ,  $\chi_{zxx}^{(i)} = \chi_{zyy}^{(i)}$ , and  $\chi_{zzz}^{(i)}$ . Therefore, the second-order polarizability induced within

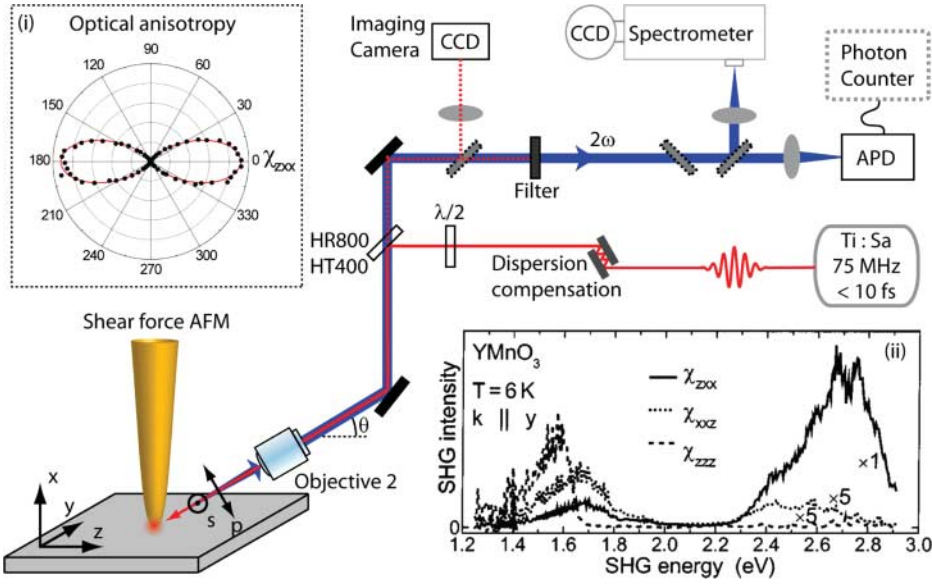


Figure 43. Experimental setup for the SHG near-field imaging of YMnO<sub>3</sub>. The fundamental incident light, with dispersion compensation, is focused onto the tip-sample gap, and the backscattered SHG is filtered and spectrally analyzed using an imaging spectrometer or integrated by means of an avalanche photodiode and detected with a photon counter. A far-field SHG polarization anisotropy (i) shows two-fold symmetry, dominated by susceptibility component  $\chi_{zxx}$ . This is consistent with the spectral dependence of the YMnO<sub>3</sub> susceptibility components (ii)[51], where  $\chi_{zxx}$  is approximately 10× the magnitude of  $\chi_{zzz}$  and  $\chi_{xxx}$  at the Ti:S energy of ~3 eV.

the crystal takes the form

$$P_x[2\omega] = 2\epsilon_0 \chi_{xxz} E_x[\omega] E_z[\omega], \tag{67}$$

$$P_y[2\omega] = 2\epsilon_0 \chi_{xxz} E_y[\omega] E_z[\omega], \tag{68}$$

$$P_z[2\omega] = 2\epsilon_0 \chi_{zxx} (E_x^2[\omega] + E_y^2[\omega]) + \chi_{zzz} E_z^2[\omega]. \tag{69}$$

Here  $E_i(\omega)$  ( $i = x, y, z$ ) are the components of the optical electric field of the fundamental light.

Figure 43(ii) shows the spectral dependence of the  $\chi_{xxz}$ ,  $\chi_{zxx}$ , and  $\chi_{zzz}$  components, demonstrating that for the 1.5 eV fundamental beam utilized in this experiment, the  $\chi_{zxx}$  term dominates and is therefore the best component for the near-field domain imaging. The spectral dependence of the different susceptibility components arises from the allowed electric dipole transitions [198].

The geometry of the experiment is shown in Figure 43, with an  $x$ -cut crystal orientation. As discussed earlier, the polarization directions of both fundamental and detected SH beams are defined with respect to the plane spanned by the tip axis (here also the  $x$ -axis of the YMnO<sub>3</sub> sample):  $p$ -polarized when contained in the plane of the tip axis and incident  $k$ -vector, and  $s$ -polarized when orthogonal to this plane. The sample is aligned such that  $p$ -polarized input light has components in the  $x$ - and  $y$ -crystallographic directions  $\mathbf{E} = (E \sin(70^\circ), E \cos(70^\circ), 0)$ . This orientation selects for the  $\chi_{zxx}$  and  $\chi_{zyy}$  tensor components. Though these have the same magnitude, the  $\chi_{zxx}$  term will dominate because of the larger magnitude of  $E_x$  and since the tip predominantly enhances the field component oriented along its axis.

In this configuration, the tip and sample SH contributions can be readily distinguished through polarization analysis. For unpolarized detection (Figure 44, left panel), the highest SH intensity

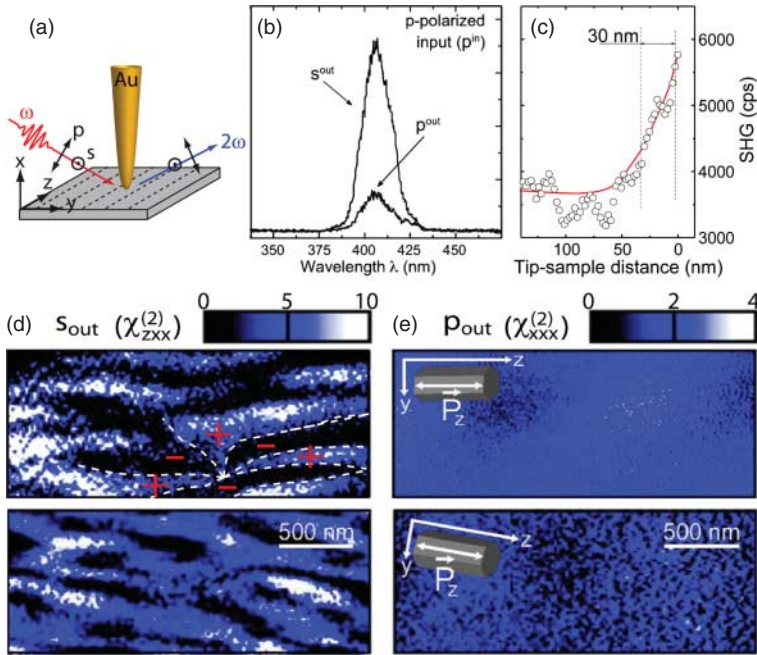


Figure 44. Orientation of tip, sample, and incident and SHG polarizations (a). SHG signal for  $p$ -polarized input (b), necessary for efficient excitation of the noble metal tip.  $s$ -polarized output allows probing of the  $\chi_{zxx}^{(i)}$  susceptibility component, while  $p$ -polarized output is a purely tip response for  $\text{YMnO}_3$  at room temperature. Increase in SHG signal on approaching the  $\text{YMnO}_3$  sample (c), showing the near-field response for  $<30$  nm. Domain maps showing the contrast obtained from the change in phase associated with the direction of spontaneous polarization.  $s$ -polarized output (d) selecting  $\chi_{zxx}^{(i)}$ , and  $p$ -polarized with only the tip response and no domain contrast (e). The lower panels show a scan with the sample slightly tilted with respect to the incident axis, demonstrating that the domains do not arise from an imaging artifact. (Adapted from C.C. Neacsu *et al.*, Phys. Rev. B 79 (2009), p. 100107 [14], copyright 2009 by the American Physical Society and C.C. Neacsu, Tip-Enhanced Near-Field Microscopy: from Symmetry Selectivity to Single Molecule Sensitivity, Humboldt Universitat, Berlin, 2008 [473].)

is observed when the fundamental light is  $p$ -polarized. The SHG from the tip itself is observed for both fundamental and detected SH beams polarized along the tip axis ( $p_{\text{in}} - p_{\text{out}}$ ). On the sample, this would probe the  $\chi_{xxx}$  tensor component, which is zero for room temperature  $\text{YMnO}_3$ . This shows that the crystal is in the PM phase at room temperature, as expected. Low-temperature measurements would allow for probing of the a-FM order, as discussed below.

The  $s$ -polarized tip-scattered SH signal displays a large FE imaging contrast as shown in Figure 44. The spatial variation of the SH response has periodicity approximately hundreds of nm. This variation is attributed to the presence of the  $180^\circ$  FE domains in  $\text{YMnO}_3$ , where the spontaneous polarization has the same magnitude and only changes sign. In this case, the image contrast arises from a local interference between the far-field reference SH signal and the near-field SHG,

$$I[2\omega] \propto |P_{\text{FF}}[2\omega] \pm P_{\text{loc}}[2\omega]|^2, \quad (70)$$

where the  $\pm$  arises from the change in spontaneous polarization direction in adjacent domains. A scan of the same region with  $p_{\text{in}} - p_{\text{out}}$  polarization shows no contrast, as expected. Also shown in Figure 44 is a scan with the sample rotated so that its  $z$ -axis makes an angle of approximately  $10^\circ$  with the scanning direction (horizontal in the images). The observed optical features maintain

their alignment along the FE axis of the crystal, demonstrating their sample intrinsic nature and ruling out any artifact arising from possible far-field interference effects [472].

The same experimental design can be extended to probe a-FM order in  $\text{YMnO}_3$  below the Néel temperature of 76 K. So far, only the  $\alpha$  spin-order symmetry, shown in Figure 41 has been observed in  $\text{YMnO}_3$  [468]. The non-zero  $\chi^{(c)}$  tensor components associated with the  $\alpha_1$  spin symmetry are  $\chi_{xyy} = -\chi_{xxx} = -\chi_{xyx} = -\chi_{yyx}$ . Therefore, it would be possible to probe the a-FM order also in this geometry, for example, by selecting  $\chi_{xxx}$  with the  $p_{\text{in}} - p_{\text{out}}$  polarization configuration. In this way, the domain behavior of both FE and a-FM orders and their relationship can be studied, providing an important technique for elucidating the nature of domain wall magneto-electric coupling within these materials. Additionally, while FE domain walls are typically too small to be resolved with  $s$ -SNOM, this is not true for a-FM domains, and in the case of multiferroics and coupled domain walls  $s$ -SNOM may provide not only single-domain information but also the ability to probe the localized properties of domain walls.

## 7. Perspective for $s$ -SNOM for nanoscale materials science

In the previous sections, we have discussed a range of possible applications of  $s$ -SNOM, with a focus on the investigation of nano-scale phenomena in correlated and other complex matter. The general compatibility of the technique with essentially any form of coherent and incoherent spectroscopy allows the choice of an optical process which couples selectively to specific electronic, spin, or structural material properties. Despite this unique potential and many successful demonstrations of  $s$ -SNOM, the technique is in several ways still in its infancy and has not yet reached its potential in terms of selectivity, specificity, and sensitivity.

In this section, we discuss future prospects and outstanding challenges in the application of  $s$ -SNOM. This includes the possible extension of  $s$ -SNOM into the ultrafast regime, the combination with low temperature and external electric and magnetic fields, optical antenna engineering of tips, and enhanced near-field selectivity and contrast.

### 7.1. Ultrafast $s$ -SNOM

Characterizing the coupled electron, nuclear, and spin dynamics in correlated matter is the goal of ultrafast spectroscopy. The time scales of these dynamics range from a few femtoseconds (electronic dephasing) to nanoseconds (spin dynamics). The ability to perturbatively excite the material on time scales shorter than the underlying correlation dynamics and monitor its subsequent temporal evolution provides a means to disentangle interactions through the different time scales associated with electron, phonon, and spin coupling [474–481]. Many coherent and incoherent, linear and nonlinear, wavemixing and pump–probe techniques have been developed over a wide range of wavelengths from the THz to the XUV, addressing dynamical processes in matter with time scales down to the attosecond regime. With  $s$ -SNOM, many of these techniques could be extended into the nano-scale, allowing the study of the elementary excitations not only on their characteristic time but also on the length scales given by spatial and temporal electron, spin, and lattice correlations. In particular, the nanoscale PS and domain order in correlated materials makes it desirable to perform ultrafast investigations within a homogeneous phase or domain region, with nanometer spatial resolution.

However, compared to ultrafast X-ray, electron diffraction, or photoemission electron microscopy, which have already demonstrated their potential for addressing ultrafast dynamics on the nano-scale, ultrafast  $s$ -SNOM is still relatively underdeveloped. In this section, we discuss the possible extension of ultrahigh spatial resolution optical near-field microscopy to ultrafast spectroscopy for spatio-temporal imaging. The broad spectral range of  $s$ -SNOM enables direct

probing of electronic and lattice excitations and their dynamics in the meV to eV range, where the information gained can complement the alternative X-ray/XUV or electron-based ultrafast nano-spectroscopy and -imaging techniques.

Electron spectroscopies are at an advantage compared to optical imaging with regard to sensitivity and spatial resolution, since the short de Broglie wavelength provides intrinsic high spatial resolution. In addition, both electron scattering and electron tunneling are governed by a strong Coulomb potential interaction and are readily detectable, with higher sensitivity on the single particle level compared to optical signal detection. Ultrafast electron diffraction and imaging can directly monitor the lattice structural evolution after an ultrashort perturbation of the system. It has the potential to probe the dynamics in space and time with the desired high spatial and temporal resolution [482–486]. The combination of femtosecond excitation with the high spatial resolution of photoemission electron microscopy (PEEM) is developing rapidly [487–491].

Similarly, X-ray diffraction and imaging benefit from high intrinsic spatial resolution and high photon energy, albeit a weaker interaction strength than electron methods. The emergent techniques of ultrafast electron diffraction, ultrafast STM, ultrafast photoemission, and ultrafast X-ray imaging thus have very high promise for the study of correlated matter. Significant progress has also been made recently in time resolved X-ray diffraction and imaging [492–501].

The desire to combine short pulse spectroscopy with STM, providing the ability to probe and manipulate matter on the atomic level, led to several proposed schemes for ultrafast scanning probe microscopy [502–504]. Concepts based on measuring the potential transient in the STM tunneling junction, i.e., a laser-induced tunneling current modification [505,506] suffer from the convolution with a transient thermal expansion of the tip due to the short tip-sample interaction range in tunneling. Recent and more refined approaches [104,507–509] show more promise and also reach the desired sub-picosecond regime.

The main experimental challenge for all optical spatio-temporal imaging as enabled by *s*-SNOM is that in any form of microscopy an increase in spatial resolution is associated with a decrease in probe volume (image pixel) and therefore signal. The implementation of spectroscopic imaging to also obtain spectral information requires additional dispersion of the signal, either spatially or in phase for direct or interferometric spectral information, thus increasing the measurement time. In the extension into the time domain, the signal is spread into a parameter space of time, spectral, and spatial dimensions, and is further reduced by the fact that the driven population or coherence excitation only encompasses a subensemble (depending on pump intensity) of the sample. This highlights the need for improved *s*-SNOM sensitivity, discrimination of background, and choice of laser source with optimized irradiance (power/bandwidth) and repetition rate matching the desired resonant sample- or structure-specific excitation and its dynamics.

Conventional aperture-based near-field microscopy using tapered optical fibers has successfully been combined with femtosecond spectroscopy to probe exciton dynamics in low-dimensional semiconductors [510]. Facilitated by the large transition dipole moment of the exciton, carrier diffusion [511], exciton spin dynamics [512], and coherent exciton dynamics could be observed [513]. However, the requirement to pass the laser pulse through an optical fiber makes this approach difficult. The higher-order dispersion of optical fibers is difficult to compensate, even with the latest laser pulse-shaping techniques. Together with the narrow spectral bandwidth and the low sensitivity of aperture probes it proved difficult to exceed 150 fs temporal and 150 nm spatial resolution [514]. While new aperture designs integrated into cantilever AFM tips would make the application to a broader range of materials and implementation of different time resolved spectroscopies feasible, low sensitivity, bandwidth, and polarization control ultimately limit the potential of NSOM [515].

As discussed above, the linear and nonlinear near-field light-matter interaction in *s*-SNOM provides nanometer spatially resolved imaging with sensitivity to multiple order parameters

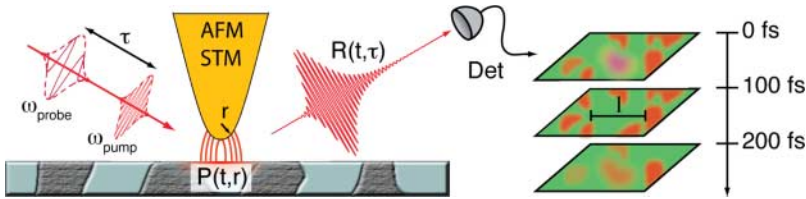


Figure 45. Concept of spatio-temporal *s*-SNOM implementing femtosecond pump–probe schemes for ultrafast spectroscopic nano-imaging. The local read out of the induced spatio-temporal optical polarization distribution  $P(t, r)$  via the radiating polarization response  $R(t, \tau)$  provides insight into the ultrafast relaxation at each scan point.

simultaneously. Two effects are particularly favorable in *s*-SNOM for achieving the required sensitivity to allow combination with ultrafast techniques. The local field enhancement associated with plasmonic modes of the tip provides for a strongly enhanced local near-field tip–sample polarization. Related to this mechanism is the enhanced coupling of the antenna mode of the tip mediating the enhanced radiative emission between the nanoscale quantum excitation and the far-field density of states [516]. This enhanced coupling gives rise to a sensitivity much higher than conventional far-field microscopy when normalized to the number of excitations probed per surface area, as exemplified by, e.g. single molecule sensitivity in TERS.

All favorable attributes of continuous wave and static *s*-SNOM are preserved in extending to ultrafast excitations, including discrimination of competing order parameters and coexisting phases, even under high magnetic and electric field stimuli. *s*-SNOM and tip-enhanced spectroscopies are fully compatible with essentially all forms of coherent and incoherent ultrafast wave-mixing and pump–probe techniques. As shown conceptually in Figure 45, a single pump pulse or combination of several pulses drives a nonequilibrium excitation in the sample, as expressed via an induced optical polarization density distribution  $P(t, r)$ . Its evolution in space and time is detected by the tip-scattering of the probe pulse, providing an optical signal that carries a signature of the localized response function  $R(t, \tau)$  for each sample position. The response function can be reconstructed by varying the probe pulse time delay, with a combination of suitable heterodyne or homodyne signal detection methods. Some of these features have already been demonstrated conceptually in first applications [273,342,517].

Significant outstanding challenges involve the synchronization and time gating of the ultrafast laser pulses with the mechanical cantilever motion in dynamic force microscopy. Several modulation schemes between laser and cantilever already developed for continuous wave spectroscopy can be refined and enable more specific extraction of the near-field optical response [518]. Aspects of duty cycle, an upper fluence limit for the diffraction limited focused pump pulse at the tip, and recovery time of the non-equilibrium excitation call for an optimized laser repetition rate (preferably in the 10 kHz to few MHz range). However, rapid progress in laser source and scanning probe microscopy developments help in the development of femtosecond *s*-SNOM as a universal technique.

## 7.2. Tip-sample coupling and spectroscopic *s*-SNOM signal interpretation

Extracting specific nano-scale spectroscopic information about electronic and lattice excitations and their polarons requires an optical signature that directly reflects the underlying transition frequencies and intrinsic lineshapes. However, the mutual optical polarization induced between the tip and the sample can distort this lineshape in several ways and make signal interpretation difficult. In particular for coherent spectroscopies in *s*-SNOM, just like any other experimental configuration that involves reflection and diffuse scattering [270], the signal response includes a superposition

of the *intrinsic* material dielectric function with both resonant absorption and dispersion as well as non-resonant terms and *extrinsic* tip size and geometry effects. The combination of these gives rise to dispersive lineshapes of the scattered light from the induced coupled tip-sample polarization, which do not allow for the direct mode and linewidth assignment from the measured spectral characteristics. For the correct mode assignment and comparison with far-field measurements of the near-field spectroscopic Drude response, localized molecular vibrations, optical phonons, or polaritons (excitons, phonon-polaritons, magnons, etc.), it is critical to deconvolute the tip- and substrate response and their coupling. This can be challenging as it requires details of tip geometry, focus conditions, and scattered light collection.

Several increasingly refined models have successfully been applied to describe the tip-sample coupling [264,269,271]. From the combination of phase and amplitude measurements of the *s*-SNOM response the near-field spectra could be traced to the underlying, e.g., IR phonon polariton resonance with increasing precision. For weakly dispersive vibrational resonances, it could be shown that the spectral phase is reminiscent of the phonon absorption spectrum [272]. This spectral phase approximation is particularly valid for molecular resonances over a wide parameter range and the near-field phase spectra directly reflect vibrational energy and intrinsic line width [273]. The combination of broadband femtosecond mid-IR excitation with interferometric heterodyne detection thus provides for a compellingly simple way for the direct comparison of IR vibrational *s*-SNOM spectra with IR absorption or ellipsometry spectra ( $\text{Im}[\epsilon(\omega)]$ ).

The extension of this femtosecond IR approach to other coherent *s*-SNOM techniques should be possible. However, a concerted effort for the combination of precise *s*-SNOM spectroscopic measurements, appropriate numerical and analytical models describing the tip-sample coupling, and exploration of alternative *s*-SNOM illumination and detection schemes might be needed.

Other effects related to the near-field tip-sample interaction that would need consideration (depending on the specific optical process) include perturbations of the intrinsic resonance properties (e.g., AC Stark effect) in the presence of large continuous wave or transient (short pulse excitations) field enhancements. This is, in particular, true in the case of large laser fields when driving higher-order nonlinear excitations beyond the perturbative regime.

Similarly, yet little understood, are possible effects as a result of large spatial gradients in the optical near-field. Field gradients in the regime of the spatial extent of the vibrational or electronic mode may lead to changes in the selection rules for quantum state transitions (IR and Raman selection rules, excitons) and multipole excitations beyond the dipole approximation.

The metallic and antenna properties of the tip can critically affect the spectral line width and its underlying dephasing time measured in *s*-SNOM. In the case of efficient coupling of the driven material's excitation to the polarizability of the tip, enhanced energy transfer and non-radiative damping and ohmic loss into the metal can lead to a decrease in excitation lifetime, and a decrease in radiative emission [519,520]. Similarly, there is the possibility of enhanced radiative decay mediated by the optical antenna properties of the tip, in particular, in the infrared [273,516]. This would lead to an increase in emission intensity with a decrease in dephasing time. These effects pose challenges for ultrafast *s*-SNOM where the presence of the tip alters the branching ratios of different decay channels, and possibly even the intrinsic dynamics, which would need careful calibration and control experiments.

### 7.3. Increased sensitivity and contrast

Pushing the sensitivity of spectroscopy and imaging techniques to the single molecule, single defect, trace element/doping, or single nanostructure has been the goal in many of the microscopy technique developments. Single molecule [521] and even intramolecular [522] spatially resolved vibrational spectroscopy was accomplished more than a decade ago by inelastic electron tunneling

spectroscopy. However, this approach requires ultra-high vacuum, conducting samples, and cryogenic temperatures. Single molecule IR *s*-SNOM can provide the optical analog, for molecular and optical phonon spectroscopy. While TERS has reached the monolayer and single molecule limit [237,253,300], the sensitivity of IR *s*-SNOM has been limited to molecular sample volumes of tens of nanometers in size [523–525] despite orders of magnitude larger cross sections ( $\sim 10^{-18}$  cm<sup>2</sup>/molecule for IR versus  $\sim 10^{-30}$  cm<sup>2</sup>/molecule/sr for Raman), in part due to low IR detection sensitivity, lack of suitable IR laser sources, and interfering background signal.

Improving sensitivity, contrast, spectral information, and spatial resolution of IR vibrational spectroscopy and microscopy has been a long standing desire and challenge. Combining broadband laser excitation with optimized spectral irradiance (power/area/bandwidth) and both tip- and substrate enhancement, many opportunities exist for pushing the sensitivity beyond the state of the art, and possibly into the single-molecule regime for the case of IR and nonlinear optical techniques (with stimulated Raman scattering a strong candidate).

Sensitivity in any spectroscopy is ultimately linked to signal contrast. With conventional far-field excitation of the tip-apex region in *s*-SNOM, the discrimination of far-field background from an extended sample area orders of magnitude larger than the nano-confined region at the tip apex has been a challenge in general. In particular, in elastic light scattering *s*-SNOM, near-field extraction is difficult and requires different modulation schemes, typically with a homo- or heterodyne reference field (as discussed in Section 5). Separating the near-field signal from a resonant and non-resonant background in the time or frequency domain is possible in some cases. While large field enhancements improve the contrast in particular in tip-enhanced Raman and especially nonlinear optical probing, it would be ideal for improved contrast to limit the optical excitation *a priori* to the region of the tip apex.

Progress towards this goal has been made by the implementation of adiabatic SPP nanofocusing on a tip to achieve a non-local and spatially confined excitation at the apex. In plasmonic nanofocusing a conical noble metal waveguide is used to concentrate a propagating surface-confined SPP into the apex of the structure, generating a spatially localized excitation with intrinsic nanometer confinement [526,527]. The propagating surface waves provide the spatial separation of the illumination source and the apex-confined excitation and thus eliminate or reduce the far-field background as shown in Figure 46(a) and (b) [231,528]. High nanofocusing efficiencies are possible, with energy delivery to the tip apex up to 20 times more efficient than under otherwise identical direct illumination conditions.

The nanofocusing approach discussed above would also lend itself to the application of ultrafast *s*-SNOM. The nanofocusing mechanism on the tip has an intrinsically broad bandwidth, with only a weak wavelength dependence, and is independent of spectral phase [517]. This stands in contrast to alternative spatio-temporal control techniques that require shaped pulses for spatial localization to occur [529–531]. Furthermore, the waveform, phase, and spectral distortions of the incident pulse during coupling, SPP propagation, and focusing can largely be compensated for by optical pulse shaping. Plasmonic nanofocusing on a tip in combination with frequency-domain pulse shaping allows for the generation of few-femtosecond pulses at the tip apex, as illustrated in Figure 46(c). The high nanofocusing efficiency gives rise to tip-enhanced SHG due to the broken symmetry at the apex in the tip axial direction. As a coherent nonlinear optical process this SHG allows for the measurement of amplitude and spectral phase and thus for the full waveform reconstruction of the optical pulse using interferometric frequency resolved optical gating (FROG). This information then serves as a feedback mechanism for the pulse shaping allowing for either minimizing the pulse duration or even the complete *deterministic* control and generation of an arbitrary optical waveform with femtosecond precision.

As an example, Figure 46(c) shows a nanofocused transform limited femtosecond pulse of  $\sim 16$  fs duration, after optimization using a multi-photon intrapulse interference phase scan (MIIPS)

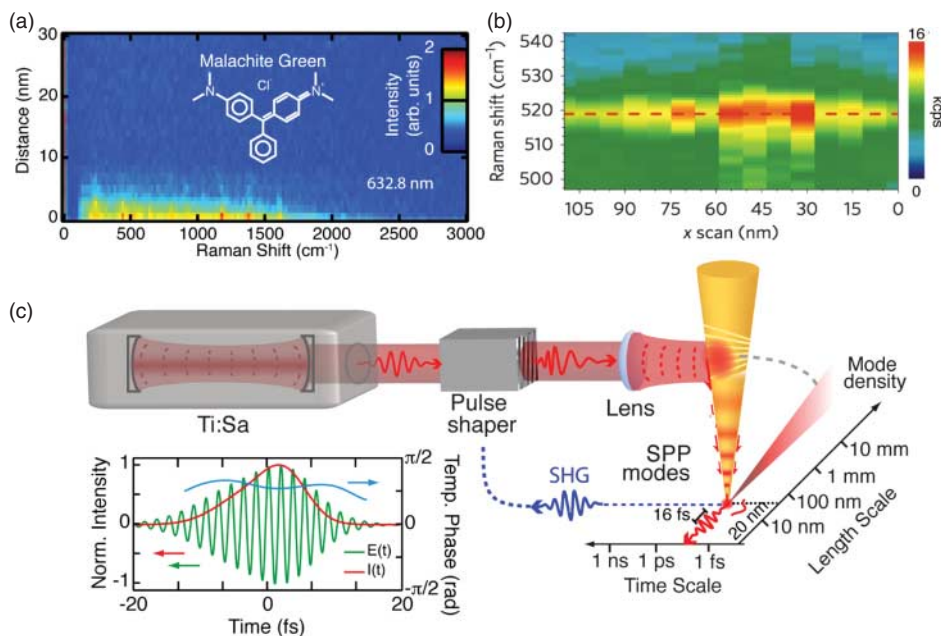


Figure 46. Grating coupled nanofocusing Raman scattering from the dye malachite green (a). Full suppression of the far-field background is observed using grating coupling (adapted from S. Berweger *et al.*, *J. Phys. Chem. Lett.* 1 (2010), p. 3427 [528], copyright 2010 American Chemical Society). Nanofocusing Raman scan from a Si step (b) using a photonic crystal coupled to a nanofocusing tip (reprinted by permission of Macmillan Publishers Ltd: F. De Angelis *et al.*, *Nat. Nanotechnol.* 5 (2010), p. 67, copyright 2010 [231]). Nanofocusing of broadband ultrafast pulses in combination with pulse shaping can be used to generate nanometer–femtosecond confined pulses with full optical waveform control (c). Inset: ultrafast optical transient measured at the tip apex after nanofocusing, with a transform-limited duration of  $\sim 16$  fs (adapted from S. Berweger, J.M. Atkin, X.G. Xu, R.L. Olmon, and M.B. Raschke, *Nano Lett.* 11 (2011), p. 4309 [517], copyright 2011 American Chemical Society).

technique, in terms of intensity (red) and phase (blue). The generation of arbitrary optical waveforms at the apex including multiple pulse replicas of different waveform and variable time delay through deterministic pulse shaping is possible, and only limited by the available spectral bandwidth of the driving laser pulse.

This approach is compatible with different ultrafast techniques, including extension to multi-dimensional spectroscopies, and is thus expected to greatly enhance the capabilities of ultrafast *s*-SNOM for the background-free nano-spectroscopic imaging of complex solids on nanometer length and femtosecond time scales simultaneously. Furthermore, the high transient field intensities that can be generated at the apex should be sufficient for electron emission via multiphoton or optical tunneling processes and higher harmonic generation (HHG). Thus, local probe electron, XUV, and X-ray spectroscopy on the nano-scale with femtosecond resolution can be envisioned.

## 7.4. Instrument development

### 7.4.1. Optical antenna engineered tips for *s*-SNOM

One key function of the tip in *s*-SNOM is to act as an optical antenna. In analogy to a conventional antenna which collects radiofrequency electromagnetic radiation, an optical antenna mediates the transformation of incident far-field radiation into a localized near-field excitation [532–535].

However, the standard *s*-SNOM excitation approach, i.e. direct illumination of the tip–sample apex region, results in poor far-to-near-field transfer efficiency, and thus poor antenna performance. In addition, although one of the primary features of an antenna is frequency selectivity, with *s*-SNOM tips a specific antenna resonance is typically unavailable except in the case of certain tip-enhanced applications using noble metal tips. Thus, utilizing the optical antenna functionality of the tip is currently in the rudimentary stages.

The ideal tip would perform three fundamental functions: it would receive and collect far-field radiation, transform the collected energy into an arbitrarily small volume, and make the confined energy available via evanescent transfer to a quantum system [536]. The transduction properties of the tip should maximize capture efficiency while minimizing propagation and transfer loss. This functionality can be implemented in a monolithic geometry (for example, the grating coupled tip discussed above), or in a set of discrete elements, such as linear rods, bowtie plasmonic particles, or tapered waveguides [537–540]. The tip antenna should be frequency selective through application of engineering design rules, allowing for either broadband or resonance-tuned operation. Precise control over the resonance bandwidth would enable selective enhancement of a targeted signal wavelength while suppressing tip interaction with undesired background signal wavelengths. Ideally the capture and concentration process would not introduce significant spectral dispersion, allowing the tip antenna to be used with light pulses of arbitrary duration for time-domain or nonlinear studies.

The probe tip is also responsible for scattering the local near-field signal to a detector using far-field optics. As a local probe, the ideal tip antenna should be sensitive to the electric-field vector orientation for complete mapping of the electromagnetic environment of the sample [232, 311,541,542]. Different types of tip antennas could be engineered to respond primarily to either the electric- or magnetic-field [543].

#### 7.4.2. *Integrated design and parallelization*

As a serial technique, SPM imaging is inherently slow compared to parallel or multiplexed imaging. While video rate AFM/STM imaging has been developed, increasing *s*-SNOM imaging speed is limited by the signal/noise for optical data collection per image pixel.

Schemes for arrays of probe tips, allowing parallel read/write/erase storage operations, have been developed [544,545]. With multi-focal laser excitation and focal plane array detection those techniques could in principle be combined with *s*-SNOM. With advances in micro- and nano-fabrication [546], the ideal solution would be to engineer both the light source and detection into the tip itself, in order to excite and detect in the near-field of the sample. While some progress has been made on local excitation, as discussed above, a near-field optical detection scheme has not yet been developed.

#### 7.4.3. *Environmental conditions*

The optical response that *s*-SNOM is based on is largely unperturbed by large magnetic fields, electric fields, current, temperature, gas pressure, etc. The investigation of many complex PS and domain formation phenomena on the nano-scale of correlated materials calls for cryogenic temperatures. As discussed above, the needed combination of AFM/STM with a cryostat and optical access has been realized. More challenging is the simultaneous use of strong magnetic field as this in general conflicts with large numerical aperture optics and beam delivery. For the application to other materials elevated temperatures would be desired, with the upper limit likely being determined by the limit of stable AFM operation. Variable and high gas pressure as desired for environmental science and catalysis applications could readily be accomplished. For many soft

matter and biological applications [547], operation in a liquid environment is feasible as long as compatibility with AFM or STM mode is maintained, and depending on the optical transmission characteristics of the liquid.

### 7.5. Outlook

The experimental technique of *s*-SNOM in combination with linear, nonlinear, and ultrafast spectroscopy provides spectroscopic access to electronic and vibrational resonances, spin, structural symmetry, and femtosecond dynamics with nanometer spatial resolution. The sensitivity, specificity, and selectivity of the optical interaction allows for the systematic real space probing of multiple order parameters and phases of complex materials simultaneously. Together with its general applicability, including under strong magnetic and electric fields, and over a wide range of temperatures, *s*-SNOM has the potential to provide new microscopic insight into the underlying mechanisms of the rich phase transition behavior of MITs, high- $T_C$  superconductors, CMR, magnetoelectric multiferroics, graphene, topological insulators and other correlated electron materials and phenomena. While we have limited the review to selected examples, the technique is equally applicable to a range of materials with similar physical phenomena, including organic conductors and semiconductors which also exhibit electron correlation, charge order, and superconducting gaps. Similarly, many materials gain their functionality as a result of nanoscale interactions including biomembranes, organic photovoltaics, and semiconductor heterostructures, and *s*-SNOM has already proved its applicability to several of these areas.

*s*-SNOM opens the door for the systematic characterization of electronic, structural, and magnetic domain texture, spatial and temporal organization, and topology that arise from and thus reflect the microscopic interactions in these systems. It could emerge as a transformative tool helping to gain insight into the underlying mechanisms of correlated matter which in turn can form the much needed basis for macroscopic control and ultimately targeted design of materials for technological applications.

### Acknowledgements

We would like to thank our collaborators on correlated matter, in particular, Manfred Fiebig, Stanislaus Wong, David Cobden, Weida Wu, Dan Dessau, Sang-Wook Cheong, and Junqiao Wu. Several present and former group members were instrumental in the success of many of the experiments, foremost Catalin Neacsu, Honghua Yang, Erik Josberger, Erik Hebestreit, Emily Chavez, Robert Olmon, Molly May, Ben Pollard, and Greg Andreev. We are indebted to many colleagues over the years, too numerous to list individually, but hopefully cited as completely as possible, who have helped us along the way with inspiring discussions and invaluable advice. This work was supported by funding from the Department of Energy Division of Materials Sciences and Engineering (Grant No. DE-SC0002197), and the National Science Foundation (NSF CAREER Grant CHE 0748226).

### Notes

1. A plethora of acronyms developed in the early phases of tip-based scanning probe optical microscopies. Different adjectives were chosen in reference to what seemed the most relevant attribute of a certain application. “Tip-enhanced” (e.g. tip-enhanced Raman scattering (TERS)) has been used where the local field enhancement of the tip seemed most relevant. “Apertureless”, (e.g., apertureless (*a*-SNOM) or apertureless *a*-NSOM) were used in reference to the distinction from the conventional use of optical fiber tips with illumination or collection of light via the aperture at the fiber terminal. “Scattering”

(e.g., in scattering (*s*-SNOM)), in reference to the function of the tip apex to scatter the evanescent tip-localized near-field into propagating and detectable far-field radiation, is also used interchangeably with “apertureless”. However, despite differences in terminology, the underlying physical mechanisms between all these techniques is very similar, if not identical. Most current descriptions of the imaging mechanism, in fact, overemphasize field-enhancement or near-field scattering, yet neglect the at least equally important function of the tip as an optical antenna defined by its capture cross section, antenna resonant properties, and its efficiency for the far- to near- to far-field transformation in and out of the localized sample excitation (parameters which are highly variable and as of yet poorly characterized or understood). We choose, unless otherwise specified, the term *s*-SNOM as a unified term.

2. Following initial demonstrations of NSOM, a debate ensued on the extent to which the observed optical contrast and resolution arose from a true optical near-field response, rather than topographic or related imaging artifacts. For further discussion see, for example, Ref. [210].
3. Much of the difficulty in estimating SERS enhancement factors arises from uncertainty in the volume of the “hot spot” and the number of molecules probed. Planar sample geometries and known surface coverages in TERS make the precise determination of the enhancement factor more readily possible.

## References

- [1] A. Lewis, M. Isaacson, A. Harootunian, and A. Murray, *Ultramicroscopy* 13 (1984), p. 227.
- [2] D.W. Pohl, W. Denk, and M. Lanz, *Appl. Phys. Lett.* 44 (1984), pp. 651–653.
- [3] E. Betzig, J.K. Trautman, T.D. Harris, J.S. Weiner, and R.L. Kostelak, *Science* 251 (1991), pp. 1468–1470.
- [4] E. Betzig, G.H. Patterson, R. Sougat, O.W. Lindwasser, S. Olenych, J.S. Bonifacio, M.W. Davidson, J. Lippencott-Schwartz, and H.F. Hess, *Science* 313 (2006), p. 1642.
- [5] S.W. Hell and J. Wichmann, *Opt. Lett.* 19 (1994), p. 780.
- [6] E. Rittweger, K.Y. Han, S.E. Irvine, C. Eggeling, and S.W. Hell, *Nat. Photon.* 3 (2009), p. 144.
- [7] D. Courjon, J.M. Vigoureux, M. Spajer, K. Sarayedine, and S. Leblanc, *Appl. Opt.* 29 (1990), pp. 3734–3740.
- [8] E. Betzig, P.L. Finn, and J.S. Weiner, *Appl. Phys. Lett.* 60 (1992), pp. 2484–2486.
- [9] M. Specht, J.D. Pedarnig, W.M. Heckl, and T.W. Hänsch, *Phys. Rev. Lett.* 68 (1992), p. 476.
- [10] R.B.G. de Hollander, N.F. van Hulst, and R.P.H. Kooyman, *Ultramicroscopy* 57 (1995), pp. 263–269.
- [11] Y. Inouye and S. Kawata, *Opt. Lett.* 19 (1994), pp. 159–161.
- [12] F. Zenhausern, Y. Martin, and H.K. Wickramasinghe, *Science* 269 (1995), pp. 1083–1085.
- [13] A. Bek, R. Vogelgesang, and K. Kern, *Rev. Sci. Instrum.* 77 (2006), p. 11.
- [14] C.C. Neacsu, B.B. Akenan, M. Fiebig, and M.B. Raschke, *Phys. Rev. B* 79 (2009), p. 100107.
- [15] A. Hartschuh, E.J. Sanchez, X.S. Xie, and L. Novotny, *Phys. Rev. Lett.* 90 (2003), p. 095503.
- [16] R. Hillenbrand, T. Taubner, and F. Keilmann, *Nature* 418 (2002), p. 159.
- [17] C. Hubert and J. Levy, *Appl. Phys. Lett.* 73 (1998), pp. 3229–3231.
- [18] B. Pettinger, B. Ren, G. Picardi, R. Schuster, and G. Ertl, *Phys. Rev. Lett.* 92 (2004), p. 096101.
- [19] N. Ocelic, A. Huber, and R. Hillenbrand, *Appl. Phys. Lett.* 89 (2006), p. 101124.
- [20] K.F. Domke and B. Pettinger, *Chem. Phys. Chem.* 11 (2010), p. 1365.
- [21] B.S. Yeo, J. Stadler, T. Schmid, R. Zenobi, and W. Zhang, *Chem. Phys. Lett.* 472 (2009), p. 1.
- [22] A. Hartschuh, H. Qian, C. Georgi, M. Böhmmler, and L. Novotny, *Anal. Bioanal. Chem.* 394 (2009), p. 7.
- [23] A. Hartschuh, *Angew. Chem. Int. Ed.* 47 (2008), p. 8178.
- [24] E. Bailo and V. Deckert, *Chem. Soc. Rev.* 37 (2008), p. 921.
- [25] F. Keilmann and R. Hillenbrand, *Phil. Trans. Roy. Soc. Lond. A* 362 (2004), pp. 787–805.
- [26] D. Schmidt, I. Kopf, and E. Bründermann, *Laser Photon. Rev.* 6 (2012), pp. 296–332.
- [27] A. Hartschuh, M. Beversluis, A. Bouhelier, and L. Novotny, *Phil. Trans. R. Soc. Lond. A* 362 (2004), p. 807.
- [28] L. Novotny and B. Hecht, *Principles of Nano-Optics*, Cambridge University Press, Cambridge, UK, 2006.
- [29] L. Novotny and S. Stranick, *Annu. Rev. Phys. Chem.* 57 (2006), pp. 303–331.

- [30] E. Dagotto, *Science* 309 (2005), pp. 257–262.
- [31] N. Mathur and P. Littlewood, *Solid State Commun.* 119 (2001), pp. 271–280.
- [32] S. Dordevic and D. Basov, *Ann. Phys (Leipzig)* 15 (2006), pp. 545–570.
- [33] D.N. Basov, R.D. Averitt, D. Marelvan der, M. Dressel, and K. Haule, *Rev. Mod. Phys.* 83 (2011), pp. 471–541.
- [34] F. Gebhard, *The Mott Metal–Insulator Transition: Models and Methods*, Springer, Berlin, 1997.
- [35] H. Bethe, *Ann. Phys.* 87 (1928), p. 55.
- [36] A. Sommerfeld, *Z. Physik A* 47 (1928), pp. 1–32.
- [37] F. Bloch, *Z. Phys. A* 57 (1929), pp. 545–555.
- [38] A.H. Wilson, *Proc. R. Soc. Lond. Ser. A* 133 (1931), pp. 458–491.
- [39] A.H. Wilson, *Proc. R. Soc. Lond. Ser. A* 134 (1931), pp. 277–287.
- [40] E. Wigner, *Phys. Rev.* 46 (1934), pp. 1002–1011.
- [41] J.H. de Boer and E.J.W. Verwey, *Proc. Phys.* 49 (1937), p. 59.
- [42] N.F. Mott and R. Peierls, *Proc. Phys. Soc.* 49 (1937), p. 72.
- [43] N.F. Mott, *Proc. Phys. Soc. Sec. A* 62 (1949), p. 416.
- [44] J.C. Slater, *Phys. Rev.* 82 (1951), pp. 538–541.
- [45] N. Mott, *The Beginnings of solid state physics: A symposium held 30 April–2 May 1979, organized by Sir Nevill Mott*, Royal Society, London, 1980.
- [46] N.F. Mott, *Phil. Mag.* 6 (1961), pp. 287–309.
- [47] S. Jin, T.H. Tiefel, M. McCormack, R.A. Fastnacht, R. Ramesh, and L.H. Chen, *Science* 264 (1994), pp. 413–415.
- [48] Y. Tokura (ed.), *Colossal Magnetoresistive Oxides*, *Advances in Condensed Matter Science Vol. 2*, Gordon and Breach, Amsterdam, 2000.
- [49] T. Chatterji, *Colossal Magnetoresistive Manganites*, Kluwer Academic Publishers, Dordrecht, the Netherlands, 2004.
- [50] M. Imada, A. Fujimori, and Y. Tokura, *Rev. Mod. Phys.* 70 (1998), pp. 1039–1263.
- [51] M. Fiebig, V.V. Pavlov, and R.V. Pisarev, *Opt. Soc. Am. B* 22 (2005), pp. 96–118.
- [52] J.G. Bednorz and K.A. Mueller, *Z. Phys. B* 64 (1986), pp. 189–193.
- [53] K.M. Shen and J.S. Davis, *Mat. Today* 11 (2008), pp. 14–21.
- [54] A.K. Geim and K.S. Novoselov, *Nat. Mater.* 6 (2007), pp. 183–191.
- [55] A.H. Castro Neto, F. Guinea, N.M.R. Peres, K.S. Novoselov, and A.K. Geim, *Rev. Mod. Phys.* 81 (2009), pp. 109–162.
- [56] Y. Zhang, V.W. Brar, C. Girit, A. Zettl, and M.F. Crommie, *Nat. Phys.* 5 (2009), pp. 722–726.
- [57] F. Bonaccorso, Z. Sun, T. Hasan, and A.C. Ferrari, *Nat. Photon.* 4 (2010), pp. 611–622.
- [58] F.H.L. Koppens, D.E. Chang, and F.J. García de Abajo, *Nano Lett.* 11 (2011), pp. 3370–3377.
- [59] Z. Fei, G.O. Andreev, W.Z. Bao, L.F.M. Zhang, A.S. McLeod, C. Wang, M.K. Stewart, Z. Zhao, G. Dominguez, M. Thiemens, M.M. Fogler, M.J. Tauber, A.H. Castro-Neto, C.N. Lau, F. Keilmann, and D.N. Basov, *Nano Lett.* 11 (2011), pp. 4701–4705.
- [60] J.E. Moore, *Nature* 464 (2010), p. 194.
- [61] B.A. Bernevig, T.L. Hughes, and S.C. Zhang, *Science* 314 (2006), pp. 1757–1761.
- [62] M. König, S. Wiedmann, C. Brüne, A. Roth, H. Buhmann, L.W. Molenkamp, X.L. Qi, and S.C. Zhang, *Science* 318 (2007), pp. 766–770.
- [63] D. Hsieh, D. Qian, L. Wray, Y. Xia, Y.S. Hor, R.J. Cava, and M.Z. Hasan, *Nature* 452 (2008), pp. 970–974.
- [64] Y. Xia, D. Qian, D. Hsieh, L. Wray, A. Pal, H. Lin, A. Bansil, D. Grauer, Y.S. Hor, R.J. Cava, and M.Z. Hasan, *Nat. Phys.* 5 (2009), pp. 398–402.
- [65] Y.L. Chen, J.G. Analytis, J.-H. Chu, Z.K. Liu, S.-K. Mo, X.L. Qi, H.J. Zhang, D.H. Lu, X. Dai, Z. Fang, S.C. Zhang, I.R. Fisher, Z. Hussain, and Z.-X. Shen, *Science* 325 (2009), pp. 178–181.
- [66] A. Moreo, S. Yunoki, and E. Dagotto, *Science* 283 (1999), pp. 2034–2040.
- [67] E. Dagotto, T. Hotta, and A. Moreo, *Phys. Rep.* 344 (2001), pp. 1–153.
- [68] M. Fiebig, T. Lottermoser, D. Fröhlich, A.V. Goltsev, and R.V. Pisarev, *Nature* 419 (2002), p. 818.
- [69] T. Choi, Y. Horibe, H.T. Yi, Y.J. Choi, W. Wu, and S.W. Cheong, *Nat. Mater.* 9 (2010), pp. 253–258.

- [70] V.B. Shenoy, D.D. Sarma, and C.N.R. Rao, *Chem. Phys. Chem.* 7 (2006), pp. 2053–2059.
- [71] V.B. Shenoy and C. Rao, *Phil. Trans. R. Soc. A* 366 (2008), pp. 63–82.
- [72] A. Moreo, M. Mayr, A. Feiguin, S. Yunoki, and E. Dagotto, *Phys. Rev. Lett.* 84 (2000), pp. 5568–5571.
- [73] Y. Tokunaga, M. Tokunaga, and T. Tamegai, *Phys. Rev. B* 71 (2005), p. 012408.
- [74] T.Z. Ward, Z. Gai, H.W. Guo, L.F. Yin, and J. Shen, *Phys. Rev. B* 83 (2011), p. 125125.
- [75] P.M. Woodward, D.E. Cox, T. Vogt, C.N.R. Rao, and A.K. Cheetham, *Chem. Mater.* 11 (1999), pp. 3528–3538.
- [76] C. Ritter, R. Mahendiran, M.R. Ibarra, L. Morellon, A. Maignan, B. Raveau, and C.N.R. Rao, *Phys. Rev. B* 61 (2000), pp. R9229–R9232.
- [77] Z. Sun, J.F. Douglas, A.V. Fedorov, Y.D. Chuang, H. Zheng, J.F. Mitchell, and D.S. Dessau, *Nat. Phys.* 3 (2007), pp. 248–252.
- [78] F.J. García de Abajo, *Rev. Mod. Phys.* 82 (2010), pp. 209–275.
- [79] R. Egerton, *Physical Properties of Electron Microscopy*, Springer, Berlin, 2005.
- [80] D. Williams and C. Carter, *Transmission Electron Microscopy*, Springer, Berlin, 2009.
- [81] M. Uehara, S. Mori, C.H. Chen, and S.W. Cheong, *Nature* 399 (1999), pp. 560–563.
- [82] J. Xu, Y. Matsui, T. Kimura, and Y. Tokura, *Physica C* 357–360 (2001), pp. 401–405.
- [83] T. Asaka, S. Yamada, S. Tsutsumi, C. Tsuruta, K. Kimoto, T. Arima, and Y. Matsui, *Phys. Rev. Lett.* 88 (2002), p. 097201.
- [84] J.C. Loudon, N.D. Mathur, and P.A. Midgley, *Nature* 420 (2002), pp. 797–800.
- [85] T. Taniuchi, H. Kumigashira, M. Oshima, T. Wakita, T. Yokoya, M. Kubota, K. Ono, H. Akinaga, M. Lippmaa, M. Kawasaki, and H. Koinuma, *Appl. Phys. Lett.* 89 (2006), p. 112505.
- [86] J. Tao, D. Niebieskikwiat, M. Varela, W. Luo, M.A. Schofield, Y. Zhu, M.B. Salamon, J.M. Zuo, S.T. Pantelides, and S.J. Pennycook, *Phys. Rev. Lett.* 103 (2009), p. 097202.
- [87] Q. He, E. Arenholz, A. Scholl, Y.H. Chu, and R. Ramesh, *Curr. Opin. Solid State Mater.* 16 (2012), pp. 216–226.
- [88] R. Falcone, C. Jacobsen, J. Kirz, S. Marchesini, D. Shapiro, and J. Spence, *Contemp. Phys.* 52 (2011), pp. 293–318.
- [89] T. Popmintchev, M.C. Chen, P. Arpin, M.M. Murnane, and H.C. Kapteyn, *Nat. Photon.* 4 (2010), pp. 822–832.
- [90] M.C. Chen, P. Arpin, T. Popmintchev, M. Gerrity, B. Zhang, M. Seaberg, D. Popmintchev, M.M. Murnane, and H.C. Kapteyn, *Phys. Rev. Lett.* 105 (2010), p. 173901.
- [91] G. Binnig, H. Rohrer, C. Gerber, and E. Weibel, *Phys. Rev. Lett.* 50 (1983), p. 120.
- [92] G. Binnig and H. Rohrer, *Rev. Mod. Phys.* 59 (1987), pp. 615–625.
- [93] R.J. Hamers and D.F. Padowitz, *Scanning Probe Microscopy and Spectroscopy: Theory, Techniques, and Applications*, Wiley, New York, 2001.
- [94] S.H. Pan, J.P. O’Neal, R.L. Badzey, C. Chamon, H. Ding, J.R. Engelbrecht, Z. Wang, H. Eisaki, S. Uchida, A.K. Gupta, K.W. Ng, E.W. Hudson, K.M. Lang, and J.C. Davis, *Nature* 413 (2001), pp. 282–285.
- [95] T. Hanaguri, C. Lupien, Y. Kohsaka, D.H. Lee, M. Azuma, M. Takano, H. Takagi, and J.C. Davis, *Nature* 430 (2004), pp. 1001–1005.
- [96] K. McElroy, J. Lee, J.A. Slezak, D.H. Lee, H. Eisaki, S. Uchida, and J.C. Davis, *Science* 309 (2005), pp. 1048–1052.
- [97] J. Lee, K. Fujita, K. McElroy, J.A. Slezak, M. Wang, Y. Aiura, H. Bando, M. Ishikado, T. Masui, J.X. Zhu, A.V. Balatsky, H. Eisaki, S. Uchida, and J.C. Davis, *Nature* 442 (2006), pp. 546–550.
- [98] M. Fäth, S. Freisem, A.A. Menovsky, Y. Tomioka, J. Aarts, and J.A. Mydosh, *Science* 285 (1999), pp. 1540–1542.
- [99] G. Binnig, C.F. Quate, and C. Gerber, *Phys. Rev. Lett.* 56 (1986), p. 930.
- [100] G. Binnig, C. Gerber, E. Stoll, T.R. Albrecht, and C.F. Quate, *Europhys. Lett.* 3 (1987), p. 1281.
- [101] T. Jungk, A. Hoffmann, M. Fiebig, and E. Soergel, *Appl. Phys. Lett.* 97 (2010), p. 012904.
- [102] E.B. Lochocki, S. Park, N. Lee, S.W. Cheong, and W. Wu, *Appl. Phys. Lett.* 99 (2011), pp. 232901–232903.
- [103] L. Zhang, C. Israel, A. Biswas, R.L. Greene, and A. Lozannede, *Science* 298 (2002), pp. 805–807.
- [104] W. Wu, C. Israel, N. Hur, S. Park, S.W. Cheong, and A. Lozannede, *Nat Mater* 5 (2006), pp. 881–886.

- [105] J.H. Lee, L. Fang, E. Vlahos, X. Ke, Y.W. Jung, L.F. Kourkoutis, J.-W. Kim, P.J. Ryan, T. Heeg, M. Roeckerath, V. Goian, M. Bernhagen, R. Uecker, P.C. Hammel, K.M. Rabe, S. Kamba, J. Schubert, J.W. Freeland, D.A. Muller, C.J. Fennie, P. Schiffer, V. Gopalan, E. Johnston-Halperin, and D.G. Schlom, *Nature* 466 (2010), pp. 954–958.
- [106] G. Sole, L.E. Bausa, and D. Jaque, *An introduction to the optical spectroscopy of inorganic solids*, Wiley, London, 2005.
- [107] H. Kuzmany, *Solid State Spectroscopy*, Springer, Berlin, 1998.
- [108] C.F. Klingshirn, *Semiconductor Optics*, Springer, Berlin, 2007.
- [109] R. Boyd, *Nonlinear Optics*, Academic Press, New York, 2003.
- [110] Y.R. Shen, *The Principles of Nonlinear Optics*, Wiley, New York, 1984.
- [111] N. Bloembergen, *Nonlinear Optics*, Benjamin, New York, 1977.
- [112] P.N. Butcher and D. Cotter, *The Elements of Nonlinear Optics*, Cambridge University Press, Cambridge, 1990.
- [113] S. Mukamel, *Principles of Nonlinear Optical Spectroscopy*, Oxford University Press, Oxford, 1995.
- [114] F. Krausz and M. Ivanov, *Rev. Mod. Phys.* 81 (2009), p. 163.
- [115] J.C. Diels and W. Rudolph, *Ultrashort Laser Pulse Phenomena*, Academic Press, San Diego, 1996.
- [116] J. Shah, *Ultrafast spectroscopy of semiconductors and semiconductor nanostructures*, 2nd ed., Springer, Berlin, 1999.
- [117] A.M. Weiner, *Ultrafast Optics*, Wiley, New York, 2009.
- [118] W.L. Chan, J. Deibel, and D.M. Mittleman, *Rep. Prog. Phys.* 70 (2007), p. 1325.
- [119] S.L. Dexheimer (ed.), *Terahertz Spectroscopy: Principles and Applications*, CRC Press, Boca Raton, FL, 2008.
- [120] T. Brabec and F. Krausz, *Rev. Mod. Phys.* 72 (2000), p. 545.
- [121] H. Kapteyn, O. Cohen, I. Christov, and M. Murnane, *Science* 317 (2007), p. 775.
- [122] A.M. Weiner, *Rev. Sci. Instrum.* 71 (2000), p. 1929.
- [123] J.D. Jackson, *Classical Electrodynamics*, 3rd ed., Wiley, New York, 1998.
- [124] W. Hayes and R. Loudon, *Scattering of Light by Crystals*, Dover, New York, 1978.
- [125] J.F. McGilp, *J. Phys. D: Appl. Phys.* 29 (1996), p. 1812–1821.
- [126] M.B. Raschke, P. Bratu, and U. Hofer, *Surf. Sci.* 410 (1998), pp. 351–361.
- [127] P. Guyot-Sionnest, A. Tadjedine, and A. Liebsch, *Phys. Rev. Lett.* 64 (1990), pp. 1678–1681.
- [128] A. Liebsch, *Phys. Rev. Lett.* 61 (1988), pp. 1233–1236.
- [129] J.E. Sipe, V. Mizrahi, and G.I. Stegeman, *Phys. Rev. B* 35 (1987), p. 9091.
- [130] T.F. Heinz, *Second-order nonlinear optical effects at surfaces and interfaces*, in *Nonlinear Surface Electromagnetic Phenomena*, G.I. Stegeman and H.-E. Ponath, eds., North-Holland, Amsterdam, 1991, p. 353.
- [131] P.S. Pershan, *Phys. Rev.* 130 (1963), p. 919.
- [132] E. Adler, *Phys. Rev.* 134 (1964), pp. A728–A733.
- [133] J. Reif, J.C. Zink, C.M. Schneider, and J. Kirschner, *Phys. Rev.* 67 (1991), p. 2878.
- [134] R.V. Pisarev, M. Fiebig, and D. Fröhlich, *Ferroelectrics* 204 (1997), pp. 1–21.
- [135] V.V. Pavlov, R.V. Pisarev, M. Fiebig, D. Fröhlich, and T. Lottermoser, *Ferroelectrics* 279 (2002), pp. 93–109.
- [136] R.R. Birss, *Symmetry and Magnetism*, North-Holland, Amsterdam, 1964.
- [137] A. Kirilyuk, *J. Phys. D* 35 (2002), p. 189.
- [138] H.A. Wierenga, M.W.J. Prins, D.L. Abraham, and T. Rasing, *Phys. Rev. B* 50 (1994), pp. 1282–1285.
- [139] V. Kirilyuk, A. Kirilyuk, and T. Rasing, *Appl. Phys. Lett.* 70 (1997), pp. 2306–2308.
- [140] M. Trzeciecki and W. Hu, *Phys. Rev. B* 62 (2000), p. 13888.
- [141] R.P. Pan, H.D. Wei, and Y.R. Shen, *Phys. Rev. B* 39 (1989), pp. 1229–1234.
- [142] G.L. Richmond, *Chem. Rev.* 102(8) (2002), pp. 2693–2724.
- [143] Y. Shen, *Nature* 337 (1989), pp. 519–525.
- [144] M. Fiebig, K. Miyano, Y. Tomioka, H. Kuwahara, Y. Tokura, and K. Reimann, *J. Appl. Phys.* 91 (2002), p. 7505.
- [145] M. Fiebig, K. Miyano, Y. Tomioka, H. Kuwahara, Y. Tokura, and K. Reimann, *Phys. Rev. Lett.* 86 (2001), pp. 6002–6005.

- [146] T. Satoh, T. Lottermoser, M. Fiebig, Y. Ogimoto, H. Tamaru, M. Izumi, and K. Miyano, *J. Appl. Phys.* 97 (2005), p. 10A914.
- [147] M.B. Raschke, M. Hayashi, S.H. Lin, and Y.R. Shen, *Chem. Phys. Lett.* 359 (2002), p. 367.
- [148] J. Schmalian and W. Hübner, *Phys. Rev. B* 53 (1996), pp. 11860–11867.
- [149] A.B. Schumacher, J.S. Dodge, M.A. Carnahan, R.A. Kaindl, D.S. Chemla, and L.L. Miller, *Phys. Rev. Lett.* 87 (2001), p. 127006.
- [150] G. Zhang, *Phys. Rev. Lett.* 86 (2001), pp. 2086–2089.
- [151] J.X. Chen and X.S. Xie, *J. Phys. Chem B* 108 (2004), p. 827.
- [152] S. Mukamel, *Annu. Rev. Phys. Chem.* 51 (2000), p. 691.
- [153] M.H. Cho, *Chem. Rev.* 108 (2008), p. 1331.
- [154] N.H. Hartshorne and A. Stuart, *Crystals and the Polarising Microscope*, Arnold, London, 2011.
- [155] J. Ferre and G.A. Gehring, *Rep. Prog. Phys.* 47 (1984), p. 513.
- [156] V. Podzorov, B.G. Kim, V. Kiryukhin, M.E. Gershenson, and S.W. Cheong, *Phys. Rev. B* 64 (2001), p. 140406.
- [157] P.W. Kolb, D.B. Romero, H.D. Drew, Y. Moritomo, A.B. Souchkov, and S.B. Ogale, *Phys. Rev. B* 70 (2004), p. 224415.
- [158] Z. Nishiyama, M. Fine, and C. Wayman, *Martensitic Transformation*, Materials Science and Technology Academic Press, New York, 1978.
- [159] C. Perry and D. Hall, *Phys. Rev. Lett.* 15 (1965), p. 700.
- [160] T.C. Damen, S.P.S. Porto, and B. Tell, *Phys. Rev.* 142 (1966), pp. 570–574.
- [161] A. Mooradian and G. Wright, *Solid State Commun.* 4 (1966), p. 431.
- [162] C.A. Arguello, D.L. Rousseau, and S.P.S. Porto, *Phys. Rev.* 181 (1969), p. 1351.
- [163] R. Loudon, *Adv. Phys.* 13 (1964), p. 423.
- [164] M. DiDomenico, S.H. Wemple, and S.P.S. Porto, *Phys. Rev.* 174 (1968), pp. 522–530.
- [165] E. Anastassakis, A. Pinczuk, E.B. F.H. Pollackad, and M. Cardona, *Solid State Commun.* 8 (1970), p. 133.
- [166] Y.D. Harker, C.Y. She, and D.F. Edwards, *Appl. Phys. Lett.* 15 (1969), pp. 272–275.
- [167] F. Cerdeira, C. Buchenauer, F. Pollak, and M. Cardona, *Phys. Rev. B* 5 (1972), p. 580.
- [168] R. Srivastava and L.L. Chase, *Phys. Rev. Lett.* 27 (1971), pp. 727–730.
- [169] M. Lines and A. Glass, *Principles and Applications of Ferroelectric and Related Materials*, Oxford University Press, 2001.
- [170] C.V. Raman and T.M.K. Nedungadi, *Nature* 145 (1940), p. 147.
- [171] M.P. Fontanta and L. Lambert, *Solid State Commun.* 10 (1972), p. 1.
- [172] P. Fleury and J. Worlock, *Phys. Rev.* 174 (1968), p. 613.
- [173] S. Berweger and M.B. Raschke, *Anal. Bioanal. Chem.* 396 (2009), pp. 115–23.
- [174] T. Dieing, O. Hollricher, and J. Toporski (eds.), *Confocal Raman Microscopy*, Springer, Berlin, 2011.
- [175] M.S. Dresselhaus, A. Jorio, M. Hofmann, G. Dresselhaus, and R. Saito, *Nano Lett.* 10 (2010), pp. 751–758.
- [176] C.T. Chien, M.C. Wu, C.W. Wei, H.H. Yang, J.J. Wu, W.F. Su, C.S. Lin, and Y.F. Chen, *Appl. Phys. Lett.* 92 (2008), p. 223102.
- [177] H.M. Fan, X.F. Fan, Z.H. Ni, Z.X. Shen, Y.P. Feng, and B.S. Zou, *J. Phys. Chem. C* 112 (2008), p. 1865.
- [178] M.B. Smith, K. Page, T. Siegrist, P.L. Redmond, E.C. Walter, R. Seshadri, L.E. Brus, and M.L. Steigerwald, *J. Am. Chem. Soc.* 130 (2008), p. 6955.
- [179] J.M. Atkin, S. Berweger, E.E. Chavez, M.B. Raschke, J. Cao, W. Fan, and J. Wu, *Phys. Rev. B* 85 (2011), p. 020101.
- [180] A.K. Arora, M. Rajalakshimi, T.R. Ravindran, and V. Sivasubramanian, *J. Raman Spectr.* 38 (2007), p. 604.
- [181] H. Richter, Z.P. Wang, and L. Ley, *Solid State Commun.* 39 (1981), p. 625.
- [182] P. Lagos, R. Hermans, N. Velasco, G. Tarrach, F. Schlaphor, C. Loppacher, and L. Eng, *Surf. Sci.* 532 (2003), p. 493.
- [183] R. Haumont, J. Kreisel, and P. Bouvier, *Phase Transit.* 79 (2006), p. 1043.

- [184] J.I. Takahashi, K. Hagita, K. Kohn, Y. Tanabe, and E. Hanamura, *Phys. Rev. Lett.* 89 (2002), p. 076404.
- [185] H. Harutyunyan, S. Palomba, J. Renger, R. Quidant, and L. Novotny, *Nano Lett.* 10 (2010), pp. 5076–5079.
- [186] A.V. Petukhov, I. Lyubchanskii, and T. Rasing, *Phys. Rev. B* 56 (1997), pp. 2680–2687.
- [187] G. Dolino, *Phys. Rev. B* 6 (1972), pp. 4025–4035.
- [188] S. Leute, T. Lottermoser, and D. Fröhlich, *Opt. Lett.* 24 (1999), pp. 1520–1522.
- [189] M. Fiebig, T. Lottermoser, D. Fröhlich, and S. Kallenbach, *Opt. Lett.* 29 (2004), pp. 41–43.
- [190] Y. Kurimura and S. Uesu, *J. Appl. Phys.* 81 (1997), p. 369.
- [191] E.D. Mishina, N.E. Sherstyuk, E.P. Pevtsov, K.A. Vorotilov, A.S. Sigov, M.P. Moret, S.A. Rossinger, P.K. Larsen, and T. Rasing, *Appl. Phys. Lett.* 78 (2001), pp. 796–798.
- [192] S.I. Bozhevolnyi, *Opt. Comm.* 152 (1998), pp. 221–224.
- [193] M. Flörsheimer, R. Paschotta, U. Kubitscheck, C. Brillert, D. Hofmann, L. Heuer, G. Schreiber, C. Verbeek, W. Sohler, and H. Fuchs, *Appl. Phys. B* 67 (1998), pp. 593–599.
- [194] A. Rosenfeldt and M. Flörsheimer, *Appl. Phys. B* 73 (2001), pp. 523–529.
- [195] M. Flörsheimer, M. Bösch, C. Brillert, M. Wierschem, and H. Fuchs, *Thin Solid Films* 327–329 (1998), pp. 241–246.
- [196] Y. Uesu, S. Kurimura, and Y. Yamamoto, *Appl. Phys. Lett.* 66 (1995), pp. 2165–2167.
- [197] A. Kirilyuk and T. Rasing, 2007, *Handbook of Magnetism and Advanced Magnetic Materials, Magnetization-induced Second Harmonic Generation*, in *Handbook of Magnetism and Advanced Magnetic Materials*, H. Kronmüller and S. Parkin, eds., Wiley, New York, pp. 1542–1565.
- [198] M. Fiebig, T. Lottermoser, and R.V. Pisarev, *J. Appl. Phys.* 93 (2003), p. 8194.
- [199] M. Fiebig, D. Fröhlich, and H.-J. Thiele, *Phys. Rev. B* 54 (1998), p. 681.
- [200] E. Abbe, *Proc. Bristol Naturalists' Soc.* 1 (1874), pp. 200–261.
- [201] L. Rayleigh, *Phil. Mag.* 5 (1896), pp. 167–195.
- [202] J.A. Reffner, P.A. Martoglio, and G.P. Williams, *Rev. Sci. Instrum.* 66 (1995), pp. 1298–1302.
- [203] L.H. Kidder, A.S. Haka, and E.N. Lewis, *Handbook of Vibrational Spectroscopy: Instrumentation for FT-IR Imaging*, Wiley, New York, 2002.
- [204] A.J. Sommer, *Handbook of Vibrational Spectroscopy: Mid-Infrared Transmission Microspectroscopy*, Wiley, New York, 2002.
- [205] E.H. Synge, *Phil. Mag* 6 (1928), p. 1.
- [206] E. Synge, *Phil. Mag.* 13 (1932), p. 297.
- [207] E.A. Ash and G. Nicholls, *Nature* 237 (1972), pp. 510–512.
- [208] R.C. Reddick, R.J. Warmack, and T.L. Ferrell, *Phys. Rev. B* 39 (1989), pp. 767–770.
- [209] H.A. Bethe, *Phys. Rev.* 66 (1944), p. 163.
- [210] B. Hecht, H. Bielefeldt, Y. Inouye, D.W. Pohl, and L. Novotny, *J. Appl. Phys.* 81 (1997), pp. 2492–2498.
- [211] M.B. Raschke and C. Lienau, *Appl. Phys. Lett.* 83 (2003), pp. 5089–5091.
- [212] R. Ruppin, *Surf. Sci.* 58 (1976), p. 550.
- [213] C.K. Chen, T.F. Heinz, D. Ricard, and Y.R. Shen, *Phys. Rev. B* 27 (1983), p. 1965.
- [214] M. Moskovits, *Rev. Mod. Phys.* 57 (1985), pp. 783–826.
- [215] C.C. Neacsu, G.A. Steudle, and M.B. Raschke, *Appl. Phys. B* 80 (2005), pp. 295–300.
- [216] C.F. Bohren and D.R. Huffman, *Absorption and Scattering of Light by Small Particles*, Wiley, New York, 1998.
- [217] C. Sönnichsen, T. Franzl, T. Wilk, G. Plessenvon, J. Feldmann, O. Wilson, and P. Mulvaney, *Phys. Rev. Lett.* 88 (2002), p. 077402.
- [218] A.L. Demming, F. Festy, and D. Richards, *J. Chem. Phys.* 122 (2005), p. 184716.
- [219] R.M. Roth, N.C. Panoiu, M.M. Adams, R.M. Osgood, C.C. Neacsu, and M.B. Raschke, *Opt. Express* 14 (2006), p. 2921.
- [220] M. Sukharev and T. Seideman, *J. Phys. Chem. A* 113 (2009), p. 7508.
- [221] L. Novotny, R.X. Bian, and X.S. Xie, *Phys. Rev. Lett.* 79 (1997), pp. 645–648.
- [222] N. Behr and M.B. Raschke, *J. Phys. Chem. C* 112 (2008), p. 3766.
- [223] E.D. Palik (ed.), *Handbook of Optical Constants of Solids*, Academic Press, San Diego, CA, 1985.

- [224] E. Le Ru, J. Grand, N. Felidj, J. Aubard, G. Levi, A. Hohenau, J. Krenn, E. Blackie, and P. Etchegoin, *J. Phys. Chem. C* 112 (2008), p. 8117.
- [225] D. Roy, J. Wang, and C. Williams, *J. Appl. Phys.* 105 (2009), p. 013530.
- [226] W. Denk and D.W. Pohl, *J. Vac. Sci. Technol. B* 9 (1991), pp. 510–513.
- [227] M. Micic, N. Klymyshyn, Y.D. Suh, and H.P. Lu, *J. Phys. Chem. B.* 107 (2003), p. 1574.
- [228] R. Hillenbrand, F. Keilmann, P. Hanarp, D.S. Sutherland, and J. Aizpurua, *Appl. Phys. Lett.* 83 (2003), p. 368.
- [229] T. Nakata and M. Watanabe, *J. Appl. Phys.* 109 (2011), p. 013110.
- [230] C.C. Neacsu, S. Berweger, and M.B. Raschke, *NanoBiotechnology* 3 (2009), pp. 172–196.
- [231] F. De Angelis, G. Das, P. Candeloro, M. Patrini, M. Galli, A. Bek, M. Lazzarino, I. Maksimov, C. Liberale, L.C. Andreani, and E. Di Fabrizio, *Nat. Nanotechnol.* 5 (2010), p. 67.
- [232] R. Olmon, M. Rang, P. Krenz, B. Lail, L. Saraf, G. Boreman, and M. Raschke, *Phys. Rev. Lett.* 105 (2010), p. 167403.
- [233] N. Hayazawa, Y. Inouye, Z. Sekkat, and S. Kawata, *Opt. Commun.* 183 (2000), p. 333.
- [234] R.M. Stockle, Y.D. Suh, V. Deckert, and R. Zenobi, *Chem. Phys.* 318 (2000), p. 131.
- [235] E. Bailo and V. Deckert, *Angew. Chem. Int. Ed.* 47 (2008), p. 1658.
- [236] B. Ren, G. Picardi, and B. Pettinger, *Rev. Sci. Instrum.* 75 (2004), p. 837.
- [237] W. Zhang, B.S. Yeo, T. Schmid, and R. Zenobi, *J. Phys. Chem. C* 111 (2007), p. 1733.
- [238] L. Eligal, F. Culfaz, V. McCaughan, N.I. Cade, and D. Richards, *Rev. Sci. Instrum.* 80 (2009), p. 033701.
- [239] N.C. Lindquist, P. Nagpal, A. Lesuffleur, D.J. Norris, and S.H. Oh, *Nano Lett.* 10 (2010), p. 1369.
- [240] C.A. Barrios, A.V. Malkovskiy, A.M. Kisliuk, A.P. Sokolov, and M.D. Foster, *J. Phys. Chem. C* 113 (2009), pp. 8158–8161.
- [241] T. Schmid, A. Messmer, B.S. Yeo, W. Zhang, and R. Zenobi, *Anal. Bioanal. Chem.* 391 (2008), p. 1907.
- [242] A. Melmed, *J. Vac. Sci. Technol. B* 9 (1990), p. 601.
- [243] K. Dickmann, F. Demming, and J. Jersch, *Rev. Sci. Instrum.* 67 (1996), p. 845.
- [244] P. Nagpal, N.C. Lindquist, S.H. Oh, and D.J. Norris, *Science* 325 (2009), p. 594.
- [245] Y. Ogawa, T. Toizumi, F. Minami, and A.V. Baranov, *Phys. Rev. B* 83 (2011), p. 081302(R).
- [246] M. Danckwerts and L. Novotny, *Phys. Rev. Lett.* 98 (2007), p. 026104.
- [247] A. Weber-Bargioni, A. Schwartzbert, M. Cornaglia, A. Ismach, J.J. Urban, Y. Pang, R. Gordon, J. Bokor, M.S. Salmeron, D.F. Ogletree, P. Ashby, S. Cabrini, and P.J. Schuck, *Nano Lett.* 11 (2011), pp. 1201–1207.
- [248] J.N. Farahani, D.W. Pohl, H.J. Eisler, and B. Hecht, *Phys. Rev. Lett.* 95 (2005), Article no. 017402.
- [249] T.a. Yano, Y. Inouye, and S. Kawata, *Nano Lett.* 6 (2006), pp. 1269–1273.
- [250] T. Yano, P. Verma, Y. Saito, T. Ichimura, and S. Kawata, *Nat. Photon.* 3 (2009), p. 473.
- [251] T. Ichimura, H. Watanabe, Y. Morita, P. Verma, S. Kawata, and Y. Inouye, *J. Phys. Chem. C* 111 (2007), pp. 9460–9464.
- [252] D. Cialla, T. Deckert-Gaudig, C. Budich, M. Laue, R. Möller, D. Naumann, V. Deckert, and J. Popp, *J. Raman Spectrosc.* 40 (2009), p. 240.
- [253] J. Steidtner and B. Pettinger, *Phys. Rev. Lett.* 100 (2008), p. 236101.
- [254] J. Stadler, T. Schmid, and R. Zenobi, *Nano Lett.* 10 (2010), p. 4514.
- [255] K.F. Domke and B. Pettinger, *J. Raman Spectrosc.* 40 (2009), p. 1427.
- [256] K. Karrai and R.D. Grober, *Ultramicroscopy* 61 (1995), pp. 197–205.
- [257] K. Karrai and I. Tiemann, *Phys. Rev. B* 62 (2000), p. 13174.
- [258] L. Novotny, E.J. Sanchez, and X.S. Xie, *Ultramicroscopy* 71 (1998), p. 21.
- [259] N. Hayazawa, Y. Saito, and S. Kawata, *Appl. Phys. Lett.* 85 (2004), p. 6239.
- [260] J. Steidtner and B. Pettinger, *Rev. Sci. Instrum.* 78 (2007), p. 103104.
- [261] J. Stadler, C. Stanciu, C. Stupperich, and A.J. Meixner, *Opt. Lett.* 33 (2008), p. 681.
- [262] F.J. Giessibl, *Rev. Mod. Phys.* 75 (2003), p. 949.
- [263] L. Gomez, R. Bachelot, A. Bouhelier, G.P. Wiederrecht, S. Chang, S.K. Gray, F. Hua, S. Jeon, J.A. Rogers, M.E. Casto, P. Royer, and G. Lerondel, *J. Opt. Soc. Am. B* 23 (2006), p. 823.
- [264] B. Deutsch, R. Hillenbrand, and L. Novotny, *Opt. Express* 16 (2008), pp. 494–501.
- [265] Z.H. Kim and S.R. Leone, *Opt. Express* 16 (2008), pp. 1733–1741.

- [266] R. Esteban, R. Vogelgesang, and K. Kern, *Phys. Rev. B* 75 (2007), p. 195410.
- [267] J. Renger, S. Grafström, L.M. Eng, and R. Hillenbrand, *Phys. Rev. B* 71 (2005), p. 075410.
- [268] R. Esteban, R. Vogelgesang, and K. Kern, *Nanotechnol.* 17 (2006), pp. 475–482.
- [269] A. Cvitkovic, N. Ocelic, and R. Hillenbrand, *Opt. Express* 15 (2007), pp. 8550–8565.
- [270] N.J. Everall, J.M. Chalmers, and P.R. Griffiths (eds.), *Vibrational Spectroscopy of Polymers: Principles and Practice*, Wiley, Chichester, 2007.
- [271] L.M. Zhang, G.O. Andreev, Z. Fei, A.S. McLeod, G. Dominguez, M. Thiemens, A.H. Castro-Neto, D.N. Basov, and M.M. Fogler, *Phys. Rev. B* 85 (2012), p. 075419.
- [272] J.M. Stiegler, Y. Abate, A. Cvitkovic, Y.E. Romanyuk, A.J. Huber, S.R. Leone, and R. Hillenbrand, *ACS Nano* 5 (2011), pp. 6494–6499.
- [273] X.G. Xu, M. Rang, I.M. Craig, and M.B. Raschke, *J. Phys. Chem. Lett.* 3 (2012), pp. 1836–1841.
- [274] T. Wei, X.D. Xiang, W.G. Wallace-Freedman, and P.G. Schultz, *Appl. Phys. Lett.* 68 (1996), pp. 3506–3508.
- [275] S. Anlage, V. Talanov, and A. Schwartz, *Scanning Probe Microscopy: Electrical and Electromechanical Phenomena at the Nanoscale*, Vol. 1, Springer, Berlin, 2007.
- [276] A. Tselev, S.M. Anlage, H.M. Christen, R.L. Moreland, V.V. Talanov, and A.R. Schwartz, *Rev. Sci. Instrum.* 74 (2003), pp. 3167–3170.
- [277] K. Lai, H. Peng, W. Kundhikanjana, D.T. Schoen, C. Xie, S. Meister, Y. Cui, M.A. Kelly, and Z.X. Shen, *Nano Lett.* 9 (2009), pp. 1265–1269.
- [278] I. Takeuchi, T. Wei, F. Duerwer, Y.K. Yoo, X.D. Xiang, V. Talyansky, S.P. Pai, G.J. Chen, and T. Venkatesan, *Appl. Phys. Lett.* 71 (1997), pp. 2026–2028.
- [279] A.S. Thanawalla, S.K. Dutta, C.P. Vlahacos, D.E. Steinhauer, B.J. Feenstra, S.M. Anlage, F.C. Wellstood, and R.B. Hammond, *Appl. Phys. Lett.* 73 (1998), pp. 2491–2493.
- [280] D.E. Steinhauer, C.P. Vlahacos, S.K. Dutta, B.J. Feenstra, F.C. Wellstood, and S.M. Anlage, *Appl. Phys. Lett.* 72 (1998), pp. 861–863.
- [281] S.M. Anlage, D.E. Steinhauer, C.P. Vlahacos, B.J. Feenstra, A.S. Thanawalla, W.S. Hu, S.K. Dutta, and F.C. Wellstood, *IEEE Trans. Appl. Supercond.* 9 (1999), pp. 4127–4132.
- [282] S. Hyun, J.H. Cho, A. Kim, J. Kim, T. Kim, and K. Char, *Appl. Phys. Lett.* 80 (2002), pp. 1574–1576.
- [283] W. Kundhikanjana, K. Lai, M.A. Kelly, and Z.X. Shen, *Rev. Sci. Instrum.* 82 (2011), p. 033705.
- [284] S. Lee, A. Pirogov, J. Han, J.G. Park, A. Hoshikawa, and T. Kamiyama, *Phys. Rev. B* 71 (2005), p. 180413.
- [285] K. Lai, M. Nakamura, W. Kundhikanjana, M. Kawasaki, Y. Tokura, M.A. Kelly, and Z.X. Shen, *Science* 329 (2010), pp. 190–193.
- [286] D.E. Steinhauer, C.P. Vlahacos, F.C. Wellstood, S.M. Anlage, C. Canedy, R. Ramesh, A. Stanishevsky, and J. Melngailis, *Appl. Phys. Lett.* 75 (1999), pp. 3180–3182.
- [287] D.E. Steinhauer and S.M. Anlage, *J. Appl. Phys.* 89 (2001), pp. 2314–2321.
- [288] K.A. Willets and R.P. Van Duyne, *Annu. Rev. Phys. Chem.* 58 (2007), p. 267.
- [289] F.W. King, R.P. Van Duyne, and G.C. Schatz, *J. Chem. Phys.* 69 (1978), p. 4472.
- [290] A. Champion and P. Kambhampati, *Chem. Soc. Rev.* 27 (1998), p. 241.
- [291] H. Kneipp, J. Kneipp, and K. Kneipp, *Chem. Soc. Rev.* 37 (2008), p. 1052.
- [292] J. Gersten and A. Nitzan, *J. Chem. Phys.* 75 (1981), p. 1139.
- [293] P.K. Aravind, R.W. Rendell, and H. Metiu, *Chem. Phys. Lett.* 85 (1982), p. 396.
- [294] K. Kneipp, Y. Wang, H. Kneipp, L.T. Perelman, I. Itzkan, R.R. Dasari, and M.S. Feld, *Phys. Rev. Lett.* 78 (1997), p. 1667.
- [295] S. Nie and S. Emory, *Science* 275 (1997), p. 1102.
- [296] J.P. Camden, J.A. Dieringer, Y. Wang, D.J. Masiello, L.D. Marks, G.C. Schatz, and R.P. Van Duyne, *J. Am. Chem. Soc.* 130 (2008), pp. 12616–12617.
- [297] L. Rodríguez-Lorenzo, R.A. Álvarez-Puebla, I. Pastoriza-Santos, S. Mazzucco, O. Stéphan, M. Kociak, L.M. Liz-Marzán, and F.J. García de Abajo, *J. Am. Chem. Soc.* 131 (2009), pp. 4616–4618.
- [298] Y. Fang, N.H. Seong, and D.D. Dlott, *Science* 321 (2008), p. 388.
- [299] E.J. Sanchez, L. Novotny, and X.S. Xie, *Phys. Rev. Lett.* 82 (1999), pp. 4014–4017.
- [300] C. Neacsu, J. Dreyer, N. Behr, and M. Raschke, *Phys. Rev. B* 73 (2006), p. 193406.

- [301] M.D. Sonntag, J.M. Klingsporn, L.K. Garibay, J.M. Roberts, J.A. Dieringer, T. Seideman, K.A. Scheidt, L. Jensen, G.C. Schatz, and R.P. Van Duyne, *J. Phys. Chem. C* 116 (2012), pp. 478–483.
- [302] B.R. Wood, E. Bailo, M.A. Khiavi, L. Tilley, S. Deed, T. Deckert-Gaudig, D. McNaughton, and V. Deckert, *Nano Lett.* 11 (2011), p. 1868.
- [303] D. Zhang, U. Heinemeyer, C. Stanciu, M. Sackrow, K. Braun, L.E. Hennemann, X. Wang, R. Scholz, F. Schreiber, and A.J. Meixner, *Phys. Rev. Lett.* 104 (2010), p. 056601.
- [304] B.S. Yeo, E. Amstad, T. Schmid, J. Stadler, and R. Zenobi, *Small* 5 (2009), p. 952.
- [305] T. Ichimura, N. Hayazawa, M. Hashimoto, Y. Inouye, and S. Kawata, *Phys. Rev. Lett.* 92 (2004), p. 220801.
- [306] T.T. Vladimir Poborchii and T. Kanayama, *Jap. J. Appl. Phys.* 44 (2005), pp. 202–204.
- [307] M. Motahashi, N. Hayazawa, A. Tarun, and S. Kawata, *J. Appl. Phys.* 103 (2008), p. 034309.
- [308] R. Ossikovski, Q. Nguyen, and G. Picardi, *Phys. Rev. B* 75 (2007), p. 045412.
- [309] P. Gucciardi, M. Lopes, R. Deturche, C. Julien, D. Barchiesi, and M.L. de la Chapelle, *Nanotechnol.* 19 (2008), p. 215702.
- [310] A. Merlen, J.C. Valmalette, P.G. Gucciardi, M. Lamy del la Chapelle, A. Frigout, and R. Ossikovski, *J. Raman. Spectrosc.* 40 (2009), p. 1361.
- [311] K.G. Lee, H.W. Kihm, J.E. Kihm, W.J. Choi, H. Kim, C. Ropers, D.J. Park, Y.C. Yoon, S.B. Choi, D.H. Woo, J. Kim, B. Lee, Q.H. Park, C. Lienau, and D.S. Kim, *Nat. Photon.* 1 (2007), pp. 53–56.
- [312] A. Tarun, N. Hayazawa, and S. Kawata, *Anal. Bioanal. Chem.* 394 (2009), p. 1775.
- [313] H. Hanafusa, N. Hirose, A. Kasamatsu, T. Mimura, T. Matsui, H.M.H. Chong, H. Mizuta, and Y. Suda, *Appl. Phys. Expr.* 4 (2011), p. 025701.
- [314] P. Hermann, M. Hecker, D. Chumakov, M. Weisheit, J. Rinderknecht, A. Shelaev, P. Dorozhkin, and L.M. Eng, *Ultramicroscopy* 111 (2011), pp. 1630–1635.
- [315] S. Berweger and M. Raschke, *J. Raman Spectrosc.* 40 (2009), pp. 1413–1419.
- [316] S. Berweger, C.C. Neacsu, Y. Mao, H. Zhou, S.S. Wong, and M.B. Raschke, *Nat. Nanotechnol.* 4 (2009), p. 496.
- [317] M. Böhmler, Z. Wang, A. Myalitsin, A. Mews, and A. Hartschuh, *Angew. Chem. Int. Ed.* 50 (2011), pp. 11536–11538.
- [318] Y. Ogawa, Y. Yuasa, F. Minami, and S. Oda, *Appl. Phys. Lett.* 99 (2011), p. 053112.
- [319] P. Hermann, H. Fabian, D. Naumann, and A. Hermelink, *J. Phys. Chem. C* 115 (2011), p. 24512.
- [320] J.I. Dadap, *Phys. Rev. B* 78 (2008), p. 205322.
- [321] A.G.F. Beerde, S. Roke, and J.I. Dadap, *J. Opt. Soc. Am. B* 28 (2011), pp. 1374–1384.
- [322] J.I. Dadap, J. Shan, and T.F. Heinz, *J. Opt. Soc. Am. B* 21 (2004), p. 1328.
- [323] C. Neacsu, G. Reider, and M. Raschke, *Phys. Rev. B* 71 (2005), Article no. 201402.
- [324] J.I. Dadap, J. Shan, K.B. Eisenthal, and T.F. Heinz, *Phys. Rev. Lett.* 83 (1999), p. 4045.
- [325] V.L. Brudny, B.S. Mendoza, and W.L. Mochán, *Phys. Rev. B* 62 (2000), p. 11152.
- [326] J. Nappa, I. Russier-Antoine, E. Benichou, C. Jonin, and P.F. Brevet, *J. Chem. Phys.* 125 (2006), p. 184712.
- [327] J. Shan, J.I. Dadap, I. Stiopkin, G.A. Reider, and T.F. Heinz, *Phys. Rev. A* 73 (2006), p. 023819.
- [328] Y. Pavlyukh and W. Hübner, *Phys. Rev. B* 70 (2004), p. 245434.
- [329] C.K. Chen, A.R.B. Castrode, and Y.R. Shen, *Phys. Rev. Lett.* 46 (1981), p. 145.
- [330] A. Wokaun, J.G. Bergman, J.P. Heritage, A.M. Glass, P.F. Liao, and D.H. Olson, *Phys. Rev. B* 24 (1981), pp. 849–856.
- [331] M.R. Beversluis, A. Bouhelier, and L. Novotny, *Phys. Rev. B* 68 (2003), p. 115433.
- [332] A. Slablab, L.L. Xuan, M. Zielinski, Y. Wildede, V. Jacques, D. Chauvat, and J.F. Roch, *Opt. Express* 20 (2012), pp. 220–227.
- [333] J. Renger, R. Quidant, N. van Hulst, S. Palomba, and L. Novotny, *Phys. Rev. Lett.* 103 (2009), p. 266802.
- [334] S. Roke, W.G. Roeterdink, J.E.G.J. Wijnhoven, A.V. Petukhov, A.W. Kleyn, and M. Bonn, *Phys. Rev. Lett.* 91 (2004), p. 258302.
- [335] Y. Nakayama, P.J. Pauzauskie, A. Radenovic, R.M. Onorato, R.J. Saykally, J. Liphardt, and P. Yang, *Nature* 447 (2007), p. 1098.
- [336] Y. Jia, H. Li, B. Zhang, X. Wei, Z. Zhang, Z. Liu, and Y. Xu, *J. Phys. Cond. Matt.* 22 (2010), p. 334218.

- [337] H. Li, P.S. Edwards, Z. Zhang, B. Zhang, Y. Xu, V. Gopalan, and Z. Liu, *J. Opt. Soc. Am. B* 28 (2011), pp. 2844–2847.
- [338] A.V. Zayats and I.I. Smolyaninov, *Phil. Trans. Ser. A* 362 (2004), pp. 843–60.
- [339] K.A. Meyer, K.C. Ng, Z. Gu, Z. Pan, W.B. Whitten, and R.W. Shaw, *Appl. Spectrosc.* 64 (2010), pp. 1–7.
- [340] S. Palomba and L. Novotny, *Nano Lett.* 9 (2009), p. 3801.
- [341] R. Trebino, *Frequency Resolved Optical Gating: The Measurement of Ultrashort Laser Pulses*, Kluwer, Dordrecht, the Netherlands, 2002.
- [342] A. Anderson, K.S. Deryckx, X.G. Xu, G. Steinmeyer, and M.B. Raschke, *Nano Lett.* 10 (2010), p. 2519.
- [343] B. Lamprecht, J.R. Krenn, A. Leitner, and F.R. Aussenegg, *Phys. Rev. Lett.* 83 (1999), pp. 4421–4424.
- [344] T. Hanke, G. Krauss, D. Trütlein, B. Wild, R. Bratschitsch, and A. Leitenstorfer, *Phys. Rev. Lett.* 103 (2009), p. 257404.
- [345] T. Hanke, J. Cesar, V. Knittel, A. Truegler, U. Hohenester, A. Leitenstorfer, and R. Bratschitsch, *Nano Lett.* 12 (2012), pp. 992–996.
- [346] T. Utikal, M.I. Stockman, A.P. Heberle, M. Lippitz, and H. Giessen, *Phys. Rev. Lett.* 104 (2010), p. 113903.
- [347] G. Behme, A. Richter, M. Suptitz, and C. Lienau, *Rev. Scient. Instrum.* 68 (1997), pp. 3458–3463.
- [348] Y. Durand, J.C. Woehl, B. Viellerobe, W. Gohde, and M. Orrit, *Rev. Scient. Instrum.* 70 (1999), pp. 1318–1325.
- [349] G. Eytan, Y. Yayon, I. Bar-Joseph, and M. Rappaport, *Ultramicroscopy* 83 (2000), pp. 25–31.
- [350] N. Fukutake, S. Takasaka, and T. Kobayashi, *J. Appl. Phys.* 91 (2002), pp. 849–855.
- [351] W. Gohde, J. Tittel, T. Basche, C. Brauchle, U.C. Fischer, and H. Fuchs, *Rev. Sci. Instrum.* 68 (1997), pp. 2466–2474.
- [352] R.D. Grober, T.D. Harris, J.K. Trautman, and E. Betzig, *Rev. Sci. Instrum.* 65 (1994), pp. 626–631.
- [353] A. Kramer, J.M. Segura, A. Hunkeler, A. Renn, and B. Hecht, *Rev. Sci. Instrum.* 73 (2002), pp. 2937–2941.
- [354] N. Fukutake, S. Takasaka, and T. Kobayashi, *Chem. Phys. Lett.* 361 (2002), pp. 42–48.
- [355] A. Kaneta, K. Okamoto, Y. Kawakami, S. Fujita, G. Marutsuki, Y. Narukawa, and T. Mukai, *Appl. Phys. Lett.* 81 (2002), pp. 4353–4355.
- [356] U. Zeimer, F. Bugge, S. Gramlich, V. Smirnovski, M. Weyers, G. Trankle, J. Grenzer, U. Pietsch, G. Cassabois, V. Emiliani, and Ch. Lienau, *Appl. Phys. Lett.* 79 (2001), pp. 1611–1613.
- [357] T. Unold, K. Mueller, C. Lienau, T. Elsaesser, and A.D. Wieck, *Phys. Rev. Lett.* 92 (2004), p. 157401.
- [358] K. Taniguchi and Y. Kanemitsu, *Jpn. J. Appl. Phys.* 44 (2005), pp. 575–577.
- [359] A. Kirihaara, S. Kono, A. Tomita, and K. Nakamura, *Opt. Rev.* 13 (2006), pp. 279–282.
- [360] G. Andreev, *Application of Infrared Nanooptics to Ultrathin Materials*, University of California, San Diego, 2011.
- [361] I.C. Moldovan-Doyen, G. Xu, L. Greusard, G. Sevin, E. Strupiechonski, G. Beaudoin, I. Sagnes, S.P. Khanna, E.H. Linfield, A.G. Davies, R. Colombelli, and Y. De Wilde, *Appl. Phys. Lett.* 98 (2011), p. 231112.
- [362] H. Yang, E. Hebestreit, and M. Raschke, *A cryogenic scattering-type scanning near-field optical microscope*, in review (2012).
- [363] N. Jiang, E.T. Foley, J.M. Klingsporn, M.D. Sonntag, N.A. Valley, J.A. Dieringer, T. Seideman, G.C. Schatz, M.C. Hersam, and R.P. Van Duyne, *Nano Lett.* 12 (2012), pp. 5061–5067.
- [364] F.J. Morin, *Phys. Rev. Lett.* 3 (1959), pp. 34–36.
- [365] N.F. Mott, *Rev. Mod. Phys.* 40 (1968), p. 677.
- [366] M. Marezio, D.B. McWhan, J.P. Remeika, and P.D. Dernier, *Phys. Rev. B* 5 (1972), pp. 2541–2551.
- [367] D. Kucharczyk and T. Niklewski, *J. Appl. Crystallogr.* 12 (1979), pp. 370–373.
- [368] A. Zylbersztein and N.F. Mott, *Phys. Rev. B* 11 (1975), pp. 4383–4395.
- [369] J.B. Goodenough, *J. Solid State Chem.* 3 (1971), pp. 490–500.
- [370] D. Paquet and P. Leroux-Hugon, *Phys. Rev. B* 22 (1980), pp. 5284–5301.
- [371] A. Cavalleri, T. Dekorsy, H.H.W. Chong, J.C. Kieffer, and R.W. Schoenlein, *Phys. Rev. B* 70 (2004), p. 161102.
- [372] R.M. Wentzcovitch, W.W. Schulz, and P.B. Allen, *Phys. Rev. Lett.* 72 (1994), pp. 3389–3392.

- [373] M.M. Qazilbash, M. Brehm, B.-G. Chae, P.-C. Ho, G.O. Andreev, B.-J. Kim, S.J. Yun, A.V. Balatsky, M.B. Maple, F. Keilmann, H.-T. Kim, and D.N. Basov, *Science* 318 (2007), p. 1750.
- [374] H.T. Kim, Y.W. Lee, B.J. Kim, B.G. Chae, S.J. Yun, K.Y. Kang, K.J. Han, K.J. Yee, and Y.S. Lim, *Phys. Rev. Lett.* 97 (2006), p. 266401.
- [375] C. Kubler, H. Ehrke, R. Huber, R. Lopez, A. Halabica, J. R. F. Haglund, and A. Leitenstorfer, *Phys. Rev. Lett.* 99 (2007), p. 116401.
- [376] D.B. McWhan, M. Marezio, J.P. Remeika, and P.D. Dernier, *Phys. Rev. B* 10 (1974), pp. 490–495.
- [377] J.P. Pouget, H. Launois, J.P. D’Haenens, P. Merenda, and T.M. Rice, *Phys. Rev. Lett.* 35 (1975), pp. 873–875.
- [378] R.M. Wentzcovich, W.W. Schulz, and P.B. Allen, *Phys. Rev. Lett.* 73 (1994), p. 3043.
- [379] T.M. Rice, H. Launois, and J.P. Pouget, *Phys. Rev. Lett.* 73 (1994), p. 3042.
- [380] A.S. Barker, H.W. Verleur, and H.J. Guggenheim, *Phys. Rev. Lett.* 17 (1966), pp. 1286–1289.
- [381] M.M. Qazilbash, M. Brehm, G.O. Andreev, A. Frenzel, P.-C. Ho, B.-G. Chae, B.-J. Kim, S. J. Yun, H.-T. Kim, A.V. Balatsky, O.G. Shpyrko, M.B. Maple, F. Keilmann, and D.N. Basov, *Phys. Rev. B* 79 (2009), p. 075107.
- [382] M.M. Qazilbash, K.S. Burch, D. Whisler, D. Shrekenhamer, B.G. Chae, H.T. Kim, and D.N. Basov, *Phys. Rev. B* 74 (2006), p. 205118.
- [383] M.M. Qazilbash, Z.Q. Li, V. Podzorov, M. Brehm, F. Keilmann, B.G. Chae, H.T. Kim, and D.N. Basov, *Appl. Phys. Lett.* 92 (2008), p. 241906.
- [384] J. Wei, Z. Wang, W. Chen, and D.H. Cobden, *Nat. Nanotech.* 4 (2009), pp. 420–424.
- [385] J. Cao and J. Wu, *Mat. Sci. Eng. R* 71 (2011), pp. 35–52.
- [386] W. Fan, J. Cao, J. Seidel, Y. Gu, J.W. Yim, C. Barrett, K.M. Yu, J. Ji, R. Ramesh, L.Q. Chen, and J. Wu, *Phys. Rev. B* 83 (2011), p. 235102.
- [387] B.S. Mun, K. Chen, J. Yoon, C. Dejoie, N. Tamura, M. Kunz, Z. Liu, M.E. Grass, S.-K. Mo, C. Park, Y.Y. Lee, and H. Ju, *Phys. Rev. B* 84 (2011), Article no. 113109.
- [388] J.M. Longo and P. Kierkega, *Acta. Chem. Scand.* 24 (1970), p. 420.
- [389] M. Ghedira, H. Vincent, M. Marezio, and J. Launay, *J. Solid State Chem.* 22 (1977), pp. 423–438.
- [390] A.C. Jones, S. Berweger, J. Wei, D. Cobden, and M.B. Raschke, *Nano Lett.* 10 (2010), p. 1574.
- [391] J. Cao, W. Fan, K. Chen, N. Tamura, M. Kunz, V. Eyert, and J. Wu, *Phys. Rev. B* 82 (2010), p. 241101.
- [392] Z. Fei, A.S. Rodin, G.O. Andreev, W. Bao, A.S. McLeod, M. Wagner, L.M. Zhang, Z. Zhao, M. Thiemens, G. Dominguez, M.M. Fogler, A.H. Castro Neto, C.N. Lau, F. Keilmann, and D.N. Basov, *Nature* 487 (2012), pp. 82–85.
- [393] J. Chen, M. Badioli, P. Alonso-Gonzalez, S. Thongrattanasiri, F. Huth, J. Osmond, M. Spasenovic, A. Centeno, A. Pesquera, P. Godignon, A. Zurutuza Elorza, N. Camara, F.J.G. de Abajo, R. Hillenbrand, and F.H.L. Koppens, *Nature* 487 (2012), pp. 77–81.
- [394] W. Kundhikanjana, K. Lai, H. Wang, H. Dai, M.A. Kelly, and Z.X. Shen, *Nano Lett.* 9 (2009), pp. 3762–3765.
- [395] A.C. Ferrari, *Solid State Commun.* 143 (2007), pp. 47–57.
- [396] M. Dresselhaus, G. Dresselhaus, R. Saito, and A. Jorio, *Phys. Rep.* 409 (2005), pp. 47–99.
- [397] A. Hartschuh, H. Qian, A.J. Meixner, N. Anderson, and L. Novotny, *Nano Lett.* 5 (2005), p. 2310.
- [398] N. Hayazawa, T. Yano, H. Watanabe, Y. Inouye, and S. Kawata, *Chem. Phys. Lett.* 376 (2003), pp. 174–180.
- [399] K. Goss, N. Peica, C. Thomsen, J. Maultzsch, C.M. Schneider, and C. Meyer, *Phys. Stat. Sol. B* 248 (2011), p. 2577.
- [400] C. Georgi and A. Hartschuh, *Appl. Phys. Lett.* 97 (2010), p. 143117.
- [401] N. Anderson, P. Anger, A. Hartschuh, and L. Novotny, *Nano Lett.* 6 (2006), pp. 744–749.
- [402] L. Malard, M. Pimenta, G. Dresselhaus, and M. Dresselhaus, *Phys. Rep.* 473 (2009), pp. 51–87.
- [403] J. Stadler, T. Schmid, and R. Zenobi, *ACS Nano* 5 (2011), p. 8442.
- [404] Y. Saito, P. Verma, K. Masui, Y. Inouye, and S. Kawata, *J. Raman Spectrosc.* 40 (2009), pp. 1434–1440.
- [405] S.S. Hong, W. Kundhikanjana, J.J. Cha, K. Lai, D. Kong, S. Meister, M.A. Kelly, Z.X. Shen, and Y. Cui, *Nano Lett.* 10 (2010), pp. 3118–3122.
- [406] C.X. Liu, H. Zhang, B. Yan, X.L. Qi, T. Frauenheim, X. Dai, Z. Fang, and S.C. Zhang, *Phys. Rev. B* 81 (2010), pp. 041307–.

- [407] J. Scott, *Ferroelectric Memories*, Springer, Berlin, 2000.
- [408] A. Yavari, M. Ortiz, and K. Bhattacharya, *Phil. Mag.* 87 (2007), p. 3997.
- [409] T. Kimura, T. Goto, H. Shintani, K. Ishizaka, T. Arima, and Y. Tokura, *Nature* 426 (2003), pp. 55–58.
- [410] A.V. Goltsev, R.V. Pisarev, T. Lottermoser, and M. Fiebig, *Phys. Rev. Lett.* 90 (2003), p. 177204.
- [411] Y. Tokunaga, N. Furukawa, H. Sakai, Y. Taguchi, T.H. Armia, and Y. Tokura, *Nat. Mater.* 8 (2009), pp. 558–562.
- [412] L. Landau, *Nature* 138 (1936), pp. 840–841.
- [413] C. Kittel, *Rev. Mod. Phys.* 21 (1949), pp. 541–583.
- [414] E. Soergel, *Appl. Phys. B* 81 (2005), pp. 729–751.
- [415] L.M. Eng and H.J. Güntherodt, *Ferroelectrics* 236 (2000), pp. 35–46.
- [416] A. Gruverman, *Ferroelectric nanodomains*, in *Encyclopedia of Nanoscience and Nanotechnology*, H. Nalwa, ed., American Scientific Publishers, Los Angeles, CA, 2004, pp. 359–375.
- [417] H. Birk, J. Glatz and Reichenbach, L. Jie, E. Schreck, and K. Dransfeld, *J. Vac. Sci. Technol. B* 9 (1991), pp. 1162–1165.
- [418] P. Guthner and K. Dransfeld, *Appl. Phys. Lett.* 61 (1992), pp. 1137–1139.
- [419] A. Gruverman, O. Auciello, and H. Tokumoto, *J. Vac. Sci. Technol. B* 14 (1996), pp. 602–605.
- [420] A.L. Kholkin, S.V. Kalinin, A. Roelofs, and A. Gruverman, *Review of ferroelectric domain imaging by Piezoresponse Force Microscopy*, in *Scanning Probe Microscopy: Electrical and Electromechanical Phenomena at the Nanoscale*, S.V. Kalinin and A. Gruverman, eds., Springer, New York, 2007, pp. 173–214.
- [421] B. Zalar, V.V. Laguta, and R. R. Blinc, *Phys. Rev. Lett.* 90 (2003), p. 037601.
- [422] M.S. Jang, M. Takashige, S. Kojima, and T. Nakamura, *J. Phys. Soc. Jap.* 52 (1983), p. 1025.
- [423] J. Munoz-Saldana, G.A. Schneider, and L. Eng, *Surf. Sci.* 480 (2001), p. L402.
- [424] T. Yang, U. Mohideen, and M. Gupta, *Appl. Phys. Lett.* 71 (1997), pp. 1960–1962.
- [425] T. Yang and U. Mohideen, *Phys. Lett. A* 250 (1998), pp. 205–210.
- [426] T. Yang, V. Gopalan, P. Swart, and U. Mohideen, *Phys. Rev. Lett.* 82 (1999), pp. 4106–4109.
- [427] D.H. Kim, Z. Sun, T. Russell, W. Knoll, and J.S. Gutmann, *Adv. Funct. Mater.* 15 (2005), p. 1160.
- [428] S.C. Kehr, M. Cebula, O. Mieth, T. Häberle Wrtling, J. Seidel, S. Grafström, L.M. Eng, S. Winnerl, D. Stehr, and M. Helm, *Phys. Rev. Lett.* 100 (2008), Article no. 256403.
- [429] X.K. Orlik, M. Labardi, and M. Allegrini, *Appl. Phys. Lett.* 77 (2000), p. 2042.
- [430] J. Levy, C. Hubert, and A. Trivelli, *J. Chem. Phys.* 112 (2000), p. 7848.
- [431] H. Ma and J. Levy, *Nano Lett.* 6 (2006), pp. 341–344.
- [432] I.I. Smolyaninov, H.Y. Liang, C.H. Lee, C.C. Davis, V. Nagarajan, and R. Ramesh, *J. Microsc.* 202 (2001), pp. 250–254.
- [433] L. Mahieu-Williams, S. Gresillon, M. Cuniot-Ponsard, and C. Boccara, *J. Appl. Phys.* 101 (2007).
- [434] E. Betzig and J.K. Trautman, *Science* 257 (1992), pp. 189–195.
- [435] J.K. Trautman, E. Betzig, J.S. Weiner, D.J. DiGiovanni, T.D. Harris, F. Hellman, and E.M. Gyorgy, *J. Appl. Phys.* 71 (1992), pp. 4659–4663.
- [436] T.J. Silva and S. Schultz, *Rev. Sci. Instrum.* 67 (1996), pp. 715–725.
- [437] F. Matthes, H. Bruckl, and G. Reiss, *Ultramicroscopy* 71 (1998), pp. 243–248.
- [438] P. Bertrand, L. Conin, C. Hermann, G. Lampel, J. Peretti, and V. Safarov, *J. Appl. Phys.* 83 (1998), pp. 6834–6836.
- [439] C. Durkan, I.V. Shvets, and J.C. Lodder, *Appl. Phys. Lett.* 70 (1997), p. 1323.
- [440] S. Takahashi, W. Dickson, R. Pollard, and A. Zayats, *Ultramicroscopy* 100 (2004), pp. 443–447.
- [441] P. Fumagalli, A. Rosenberger, G. Eggers, A. Munnemann, N. Held, and G. Güntherodt, *Appl. Phys. Lett.* 72 (1998), pp. 2803–2805.
- [442] S. Gresillon, J. Cory, J.C. Rivoal, and A.C. Boccara, *J. Opt. A: Pure Appl. Opt.* 1 (1999), pp. 178–184.
- [443] J.N. Walford, J.A. Porto, R. Carminati, and J.J. Greffet, *J. Opt. Soc. Am. A* 19 (2002), pp. 572–583.
- [444] P. Fumagalli, 2005, *Scanning near-field magneto-optic microscopy*, in *Modern Techniques For Characterizing Magnetic Materials*, Kluwer Academic Publishers, Dordrecht, the Netherlands, pp. 455–515.
- [445] S. Sugano and N. Kojima, *Magneto-Optics*, Springer, Berlin, 2000.

- [446] W. Dickson, S. Takahashi, R. Pollard, R. Atkinson, and a.V. Zayats, *J. Microsc.* 209 (2003), p. 194.
- [447] A. Bauer, B.L. Petersen, T. Crecelius, G. Meyer, D. Wegner, and G. Kaindl, *J. Microsc.* 194 (1999), pp. 507–511.
- [448] A. Kapitulnik, J.S. Dodge, and M.M. Fejer, *J. Appl. Phys.* 75 (1994), pp. 6872–6877.
- [449] B.L. Petersen, A. Bauer, G. Meyer, T. Crecelius, and G. Kaindl, *Appl. Phys. Lett.* 73 (1998), pp. 538–540.
- [450] O.B. Bergossi, H.W. Ioland, S.H. Udlet, R.D. Eturche, and P.R. Oyer, *Jap. J. Appl. Phys.* 38 (1999), pp. 655–658.
- [451] H. Wioland, O. Bergossi, S. Hudlet, K. Mackay, and P. Royer, *Eur. Phys. J.: Appl. Phys.* 5 (1999), pp. 289–295.
- [452] L. Aigouy, S. Gresillon, A. Lahrech, A. Boccara, J. Rivoal, V. Mathet, C. Chappert, J. Jamet, and J. Ferre, *J. Microsc.* 194 (1999), pp. 295–298.
- [453] J.M. Vigoureux, C. Girard, and F. Depasse, *J. Mod. Opt.* 41 (1994), pp. 49–58.
- [454] X. Zhao and R. Kopelman, *Ultramicroscopy* 61 (1995), pp. 69–80.
- [455] A.V. Zayats and V. Sandoghdar, *Opt. Comm.* 178 (2000), p. 245.
- [456] I.I. Smolyaninov, A.V.V. Zayats, and C.C. Davis, *Opt. Lett.* 22 (1997), p. 1592.
- [457] D. Wegner, U. Conrad, J. Guřfödde, G. Meyer, T. Crecelius, and A. Bauer, *J. Appl. Phys.* 88 (2000), p. 2166.
- [458] W. Dickson, S. Takahashi, C. Boronat, R. Bowman, J. Gregg, and A. Zayats, *Phys. Rev. B* 72 (2005), pp. 1–6.
- [459] L. Landau and E. Lifshitz, *Electrodynamics of Continuous Media*, Pergamon, Oxford, 1960.
- [460] W.F. Brown, R. Hornreich, and S. Shtrikman, *Phys. Rev.* 168 (1968), p. 574.
- [461] W. Eerenstein, N.D. Mathur, and J.F. Scott, *Nature* 442 (2006), pp. 759–65.
- [462] C.a.F. Vaz, J. Hoffman, C.H. Ahn, and R. Ramesh, *Adv. Mater.* 22 (2010), pp. 2900–18.
- [463] N.A. Hill, *J. Phys. Chem. B* 104 (2000), pp. 6694–6709.
- [464] N.A. Spaldin and M. Fiebig, *Science* 309 (2005), p. 5733.
- [465] J. Rondinelli, A. Eidelson, and N. Spaldin, *Phys. Rev. B* 79 (2009), p. 205119.
- [466] N. Fujimura, S. Azuma, N. Aoki, T. Yoshimura, and T. Ito, *J. Appl. Phys.* 80 (1996), pp. 7084–7088.
- [467] B.B. Van Aken, T.T. Palstra, A. Filippetti, and N.A. Spaldin, *Nat. Mater.* 3 (2004), pp. 164–170.
- [468] M. Fiebig, D. Frohlich, K. Kohn, S. Leute, T. Lottermoser, V. Pavlov, and R. Pisarev, *Phys. Rev. Lett.* 84 (2000), pp. 5620–5623.
- [469] G.E. Bacon, *Neutron Diffraction*, Clarendon Press, Oxford, 1975.
- [470] T. Choi, S. Lee, Y.J. Choi, V. Kiryukhin, and S.W. Cheong, *Science* 324 (2009), pp. 63–66.
- [471] S.C. Chae, Y. Horibe, D.Y. Jeong, S. Rodan, N. Lee, and S. Cheong, *Proc. Natl Acad. Sci.* 107 (2010), p. 21366.
- [472] P.G. Gucciardi, G. Bachelier, M. Allegrini, J. Ahn, M. Hong, S. Chang, W. Jhe, S.C. Hong, and S.H. Baek, *J. Appl. Phys.* 101 (2007).
- [473] C.C. Neacsu, *Tip-Enhanced Near-Field Microscopy: from Symmetry Selectivity to Single Molecule Sensitivity*, Humboldt Universität, Berlin, 2008.
- [474] R.D. Averitt, A.I. Lobad, C. Kwon, S.A. Trugman, V.K. Thorsmolle, and A.J. Taylor, *Phys. Rev. Lett.* 87 (2001), p. 017401.
- [475] M. Forst, C. Manzoni, S. Kaiser, Y. Tomioka, Y. Tokura, R. Merlin, and A. Cavalleri, *Nat. Phys.* 7 (2011), pp. 854–856.
- [476] R.I. Tobey, D. Prabhakaran, A.T. Boothroyd, and A. Cavalleri, *Phys. Rev. Lett.* 101 (2008), p. 197404.
- [477] S. Wall, D. Prabhakaran, A.T. Boothroyd, and A. Cavalleri, *Phys. Rev. Lett.* 103 (2009), p. 097402.
- [478] M. Fiebig, K. Miyano, Y. Tomioka, and Y. Tokura, *Appl. Phys. B* 71 (2000), pp. 211–215.
- [479] T. Satoh, B.B. Van Aken, N.P. Duong, T. Lottermoser, and M. Fiebig, *Phys. Rev. B* 75 (2007), p. 6.
- [480] M. Fiebig, N.P. Duong, T. Satoh, B.B. Van Aken, K. Miyano, Y. Tomioka, and Y. Tokura, *J. Phys. D* 41 (2008), p. 11.
- [481] J. Graf, C. Jozwiak, C.L. Smallwood, H. Eisaki, R.A. Kaindl, D.H. Lee, and A. Lanzara, *Nat. Phys.* 7 (2011), pp. 805–809.
- [482] B.J. Siwick, J.R. Dwyer, R.E. Jordan, and R.J.D. Miller, *Chem. Phys.* 299 (2004), pp. 285–305.

- [483] A.H. Zewail, *Ann. Rev. Phys. Chem.* 57 (2006), pp. 65–103.
- [484] P. Baum, D.S. Yang, and A.H. Zewail, *Science* 318 (2007), pp. 788–792.
- [485] J.R. Dwyer, R.E. Jordan, C.T. Hebeisen, M. Harb, R. Ernstorfer, T. Dartigalongue, and R.J. Dwayne Miller, *J. Mod. Opt.* 54 (2007), pp. 905–922.
- [486] H.S. Park, J.S. Baskin, and A.H. Zewail, *Nano Lett.* 10 (2010), pp. 3796–3803.
- [487] A. Kubo, K. Onda, H. Petek, Z. Sun, Y.S. Jung, and H.K. Kim, *Nano Lett.* 5 (2005), p. 1123.
- [488] A. Kubo, N. Pontius, and H. Petek, *Nano Lett.* 7 (2007), pp. 470–475.
- [489] P. Melchior, D. Bayer, C. Schneider, A. Fischer, M. Rohmer, W. Pfeiffer, and M. Aeschlimann, *Phys. Rev. B* 83 (2011), p. 235407.
- [490] T. Rohwer, S. Hellmann, M. Wiesenmayer, C. Sohrt, A. Stange, B. Slomski, A. Carr, Y. Liu, L.M. Avila, M. Kallane, S. Mathias, L. Kipp, K. Rossnagel, and M. Bauer, *Nature* 471 (2011), p. 490.
- [491] A. Oelsner, M. Rohmer, C. Schneider, D. Bayer, G. Schoenhense, and M. Aeschlimann, *J. Elec. Spectrosc. Rel. Phenomena* 178 (2010), pp. 317–330.
- [492] J. Kortright, D. Awschalom, J. Stöhr, S. Bader, Y. Idzerda, S. Parkin, I.K. Schuller, and H.C. Siegmann, *J. Magn. Magn. Mater.* 207 (1999), pp. 7–44.
- [493] J. Miao, T. Ishikawa, B. Johnson, E.H. Anderson, B. Lai, and K.O. Hodgson, *Phys. Rev. Lett.* 89 (2002), Article no. 088303.
- [494] P. Thibault, M. Dierolf, A. Menzel, O. Bunk, C. David, and F. Pfeiffer, *Science* 321 (2008), pp. 379–382.
- [495] A. Ricci, N. Poccia, B. Joseph, L. Barba, G. Arrighetti, G. Ciasca, J.Q. Yan, R.W. McCallum, T.A. Lograsso, N.D. Zhigadlo, J. Karpinski, and A. Bianconi, *Phys. Rev. B* 82 (2010), p. 144507.
- [496] R.L. Sandberg, D.A. Raymondson, C. Laovorakiat, A. Paul, K.S. Raines, J. Miao, M.M. Murnane, H.C. Kapteyn, and W.F. Schlotter, *Opt. Lett.* 34 (2009), pp. 1618–1620.
- [497] M.M. Qazilbash, A. Tripathi, A.A. Schafgans, B.-J. Kim, H.-T. Kim, Z. Cai, M.V. Holt, J.M. Maser, F. Keilmann, O.G. Shpyrko, and D.N. Basov, *Phys. Rev. B* 83 (2011), p. 165108.
- [498] P.G. Evans, E.D. Isaacs, G. Aeppli, Z. Cai, and B. Lai, *Science* 295 (2002), pp. 1042–1045.
- [499] K. Holldack, N. Pontius, E. Schierle, T. Kachel, V. Soltwisch, R. Mitzner, T. Quast, G. Springholz, and E. Weschke, *Appl. Phys. Lett.* 97 (2010), pp. 062502–062503.
- [500] H. Ehrke, R.I. Tobey, S. Wall, S.A. Cavill, M. Forst, V. Khanna, Th. Garl, N. Stojanovic, D. Prabhakaran, A.T. Boothroyd, M. Gensch, A. Mirone, P. Reutler, A. Revcolevschi, S.S. Dhesi, and A. Cavalleri, *Phys. Rev. Lett.* 106 (2011), p. 217401.
- [501] A. Barty, *J. Phys. B Atom. Mol. Opt. Phys.* 43 (2010), p. 194014.
- [502] R.J. Hamers and D.G. Cahill, *J. Vac. Sci. Technol. B* 9 (1991), p. 514.
- [503] S. Weiss, D.F. Ogletree, D. Botkin, M. Salmeron, and D.S. Chemla, *Appl. Phys. Lett.* 63 (1993), pp. 2567–2569.
- [504] M.J. Feldstein, P. Vohringer, W. Wang, and N.F. Scherer, *J. Phys. Chem.* 100 (1996), pp. 4739–4748.
- [505] V. Gerstner, A. Thon, and W. Pfeiffer, *J. Appl. Phys.* 87 (2000), pp. 2574–2580.
- [506] M. Merschedorf, W. Pfeiffer, A. Thon, and G. Gerber, *Appl. Phys. Lett.* 81 (2002), pp. 286–288.
- [507] S.W. Wu and W. Ho, *Phys. Rev. B* 82 (2010), p. 085444.
- [508] Y. Terada, S. Yoshida, O. Takeuchi, and H. Shigekawa, *Nat. Photon.* 4 (2010), p. 869.
- [509] A. Dolocan, D.P. Acharya, P. Zahl, P. Sutter, and N. Camillone III, *J. Phys. Chem. C* 115 (2011), pp. 10033–10043.
- [510] C. Lienau, *Phil. Trans. R. Soc. A* 362 (2004), pp. 861–879.
- [511] M. Achermann, B.A. Nechay, U. Siegner, A. Hartmann, D. Oberli, E. Kapon, and U. Keller, *Appl. Phys. Lett.* 76 (2000), pp. 2695–2697.
- [512] J. Levy, V. Nikitin, J.M. Kikkawa, A. Cohen, N. Samarth, R. Garcia, and D.D. Awschalom, *Phys. Rev. Lett.* 76 (1996), pp. 1948–1951.
- [513] T. Guenther, C. Lienau, T. Elsaesser, M. Glanemann, V.M. Axt, T. Kuhn, S. Eshlaghi, and A.D. Wieck, *Phys. Rev. Lett.* 89 (2002), p. 057401.
- [514] V. Emiliani, T. Guenther, C. Lienau, R. Netzel, and K.H. Ploog, *J. Microsc.* 202 (2001), p. 229.
- [515] H. Okamoto and K. Imura, *Prog. Surf. Sci.* 84 (2009), pp. 199–229.
- [516] S. Berweger, J.M. Atkin, R.L. Olmon, and M.B. Raschke, *J. Phys. Chem. Lett.* (2012) (in press).
- [517] S. Berweger, J.M. Atkin, X.G. Xu, R.L. Olmon, and M.B. Raschke, *Nano Lett.* 11 (2011), p. 4309.

- [518] T. Ichimura, S. Fujii, P. Verma, T. Yano, Y. Inouye, and S. Kawata, *Phys. Rev. Lett.* 102 (2009), p. 186101.
- [519] K.H. Drexhage, *Prog. Opt. Commun.* 12 (1974), p. 163.
- [520] P. Anger, P. Bharadwaj, and L. Novotny, *Phys. Rev. Lett.* 96 (2006), p. 113002.
- [521] B.C. Stipe, M.A. Rezaei, and W. Ho, *Science* 280 (1998), p. 1732.
- [522] N. Ogawa, G. Mikaelian, and W. Ho, *Phys. Rev. Lett.* 98 (2007), p. 166103.
- [523] B.B. Akhremitchev, Y. Sun, L. Stebounova, and G.C. Walker, *Langmuir* 18 (2002), pp. 5325–5328.
- [524] T. Taubner, R. Hillenbrand, and F. Keilmann, *Appl. Phys. Lett.* 85 (2004), p. 5064.
- [525] M.B. Raschke, L. Molina, T. Elsaesser, D.H. Kim, W. Knoll, and K. Hinrichs, *Chem. Phys. Chem.* 6 (2005), p. 2197.
- [526] C. Ropers, C. Neacsu, T. Elsaesser, M. Albrecht, M. Raschke, and C. Lienau, *Nano Lett.* 7 (2007), p. 2784.
- [527] C.C. Neacsu, S. Berweger, R.L. Olmon, L.V. Saraf, C. Ropers, and M.B. Raschke, *Nano Lett.* 10 (2010), pp. 592–596.
- [528] S. Berweger, J.M. Atkin, R.L. Olmon, and M.B. Raschke, *J. Phys. Chem. Lett.* 1 (2010), p. 3427.
- [529] M. Aeschlimann, M. Bauer, D. Bayer, T. Brixner, F.J. Garcia de Abajo, W. Pfeiffer, M. Rohmer, C. Spindler, and F. Steeb, *Nature* 446 (2007), p. 301.
- [530] M. Aeschlimann, M. Bauer, D. Bayer, T. Brixner, S. Cunovic, F. Dimler, A. Fischer, W. Pfeiffer, M. Rohmer, C. Schneider, F. Steeb, C. Strüber, and D.V. Voronine, *Proc. Natl Acad. Sci.* 107 (2010), p. 5329.
- [531] M. Durach, A. Rusina, M.I. Stockman, and K. Nelson, *Nano Lett.* 7 (2007), p. 3145.
- [532] J. Alda, J.M. Rico-García, J.M. López-Alonso, and G. Boreman, *Nanotechnology* 16 (2005), pp. S230–S234.
- [533] P. Bharadwaj, B. Deutsch, and L. Novotny, *Adv. Opt. Photon.* 1 (2009), p. 438.
- [534] P. Biagioni, J.S. Huang, and B. Hecht, *Rep. Prog. Phys.* 75 (2012), p. 024402.
- [535] N. Berkovitch, P. Ginzburg, and M. Orenstein, *J. Phys. Condens. Matter* 24 (2012), p. 073202.
- [536] R. Olmon and M. Raschke, *Nanotechnology* 23 (2012), Article no. 444001.
- [537] N. Yu, E. Cubukcu, L. Diehl, M.A. Belkin, K.B. Crozier, F. Capasso, D. Bour, S. Corzine, and G. Höfler, *Appl. Phys. Lett.* 91 (2007), p. 173113.
- [538] T.H. Taminiau, R.J. Moerland, F.B. Segerink, L. Kuipers, and N.F. van Hulst, *Nano Lett.* 7 (2007), pp. 28–33.
- [539] E. Verhagen, M. Spasenovic, A. Polman, and L. (Kobus) Kuipers, *Phys. Rev. Lett.* 102 (2009), p. 203904.
- [540] M. Schnell, P. Alonso-Gonzalez, L. Arzubriaga, F. Casanova, L.E. Hueso, A. Chuvilin, and R. Hillenbrand, *Nat. Photon.* 5 (2011), p. 28.
- [541] M.A. Seo, A.J.L. Adam, J.H. Kang, J.W. Lee, S.C. Jeoung, Q.H. Park, P.C.M. Planken, and D.S. Kim, *Opt. Exp.* 15 (2007), pp. 11781–11789.
- [542] T. Grosjean, I.A. Ibrahim, M.A. Suarez, G.W. Burr, M. Mivelle, and D. Charraut, *Opt. Exp.* 18 (2010), p. 5809.
- [543] E. Devaux, A. Dereux, E. Bourillot, J.c. Weeber, Y. Lacroute, J.p. Goudonnet, and C. Girard, *Phys. Rev. B* 62 (2000), pp. 10504–10514.
- [544] M. Lutwyche, C. Andreoli, G. Binnig, J. Brugger, U. Drechsler, W. Häberle, H. Rohrer, H. Rothuizen, P. Vettiger, G. Yaralioglu, and C. Quate, *Sensor Actuat. A-Phys.* 73 (1999), pp. 89–94.
- [545] P. Vettiger, J. Brugger, M. Despont, U. Drechsler, U. Dürig, W. HŠberle, M. Lutwyche, H. Rothuizen, R. Stutz, R. Widmer, and G. Binnig, *Microelectron. Eng.* 46 (1999), pp. 11–17.
- [546] N.C. Lindquist, P. Nagpal, K.M. McPeak, D.J. Norris, and S.H. Oh, *Rep. Prog. Phys.* 75 (2012), p. 036501.
- [547] T. Schmid, B.S. Yeo, G. Leong, J. Stadler, and R. Zenobi, *J. Raman Spectrosc.* 40 (2009), p. 1392.
- [548] J. Wu, Q. Gu, B.S. Guiton, N.P. deLeon, L. Ouyang, and H. Park, *Nano Lett.* (6) (2006), pp. 2313–2317.